Integrated Optical Phased Arrays for Lidar Applications

by

Ami Yaacobi

Submitted to the Department of Material Science and Engineering
in partial fulfillment of the requirements for the degree of
Doctor of Philosophy in Material Science
at the
MASSACHUSETTS INSTITUTE OF TECHNOLOGY
June 2015

Author Signature redacted
Department of Material Science and Engineering
May 5th , 2015

Certified by Signature redacted
Michael R. Watts
Associate Professor of Electrical Engineering
Thesis Supervisor and committee chairman

Thesis Reader Signature redacted
Yoel Fink
Professor of Material Science and Engineering

Accepted by Signature redacted
Donald R. Sadoway
Chair, Departmental Committee on Graduate Students

Integrated optical phased arrays for lidar applications

by
Ami Yaacobi

Submitted to the Department of Material Science and Engineering
On May 5th, 2015, in partial fulfillment of the requirements for the degree of
Doctor of Philosophy in Material Science

Abstract

It is no wonder that research in Si photonics (optical components embedded on a silicon platform) has bloomed so rapidly the last few years. Combining low loss, strong refractive index contrast (and, thus, light confinement), with electro-optical and thermo-optical effects, allows for the fabrication of dense and complex electro-optical Si photonics systems. Moreover, because it is based on the well-established platforms of the CMOS industry, Si photonics is expected to rapidly shift from a research field to the production of high volume, low cost, complex, integrated electro-optical systems. One class of systems receiving increasing interest are Nanophotonic Phased Arrays (NPAs), which offer free space emission of a manipulated beam that can be steered, focused, have controlled angular momentum and even create holograms.

Still, some substantial challenges remain in applying these NPAs to real systems. Large cell size and spacing between adjacent antennas produce multiple beams and reduce effective steering angle. In addition, small beam angle requirements and large aperture in NPAs receivers demand large phased array size. In order to allow for both steering angle and large aperture, a large array with small cell size is required resulting large number of unit cells in one array.

In this work, we first propose two metallic nanoantennas to couple between a waveguide mode to free space radiation. Then, by combining existing Si photonic components like directional couplers and modulators with optical antennas and phase shifters that were designed for this goal we demonstrate, in this work, several NPAs for various applications. Using unique architecture, we then, specifically focus on a, NPA based, lidar. These lidar systems are essential components in any autonomous system maneuvering in an undefined environment. An on chip lidar like this one can serve, for example, in the automotive industry for safety enhancement and to allow autonomous driving functionality at an affordable price.

Thesis Supervisor: Michael R. Watts
Title: Associate Professor of Electrical Engineering

Acknowledgements

As I stand at the finish line, I owe my gratitude to all the people who have made this dissertation possible and because of whom my graduate experience has been one that will remain with me forever.

A great many people have contributed to this dissertation. First and foremost, I owe gratitude to my advisor, Professor Michael (Mike) Watts. I have been fortunate to have an advisor, who gave me the freedom to explore, and at the same time, the guidance to recover when my experiments did not go as I expected.

I would also like to thank Professors Yoel Fink and Eugene Fitzgerald for serving on my thesis committee. Their helpful thoughts , comments and inquiries helped to enrich and convey my ideas. I want to extend my thanks to Professor Fink who was there with sage advice whenever I needed it.

I am sincerely appreciative of having my colleagues beside me; Cheri Agaskar, Chris Poulton, Michele Moresco, Ehsan Shah Hoseini, Johnathan Bradley, Dave Cole, Katia Shteyrkova, Jie Sun, Erman Timurdogan, Manan Raval, Purnawirman, Zhan Su, Nanxi Li, Gurpreet Singh and Jerry Zhou. During hard and good times, I enjoyed their collaboration, support and wisdom. I am especially thankful to Cheri Agaskar and Chris Poulton for encouraging the use of correct grammar and consistent notation in my writings and for carefully reading and commenting this manuscript and earlier ones.

I want to acknowledge and give thanks to Ellisa Haverty and Angelita Mireles, the academic staff at DMSE, and Stacy McGrath, our group's assistant, for accompanying and supporting me throughout the unknown bureaucracy of MIT. I would also like to thank Stacy, for walking through my dissertation and correcting my grammar. I would like to add my deep appreciation to the system staff, Sukru Cinar, Bill Adams and Al McGurl who maintained the computers, lab equipment and office environment. Their dedication and efficiency enabled me to avoid much frustration and delays.

I would also like to express special thanks to Toyota Motor Corporation for funding the research and enabling this to become a reality. Specifically, I would like to thank Toyota's team on the project: Jae Lee and Paul Schmalenberg, from Toyota Motor Engineering & Manufacturing North America (TEMA), and especially to Tsuyoshi Nomura, from Toyota Central R&D Labs (TCRDL), for his extended involvement in the research.

Last , but not least, I would like to give thanks and my deepest appreciation to my wife, Esti, my three amazing children, parents, siblings extended family and friends. I could not have done this without them. They were there with me in good and hard times celebrating my successes and supporting me during my challenges.

Table of Contents

Table of Figures

Appendix Figures

Table of Tables

1 Introduction

1.1 Silicon Photonics

The last century was significant for its technology breakouts (1). Breakthroughs in two specific fields origin at the middle of that century had probably have the largest impact on our world as we see it today – The field of optics and the field of solid state electronics. The optics field, with the two separate developments of laser and fiber optics, enabled today's optical communication and opened a new for human kind. Broadband laser communication, with low carrier loss over long distance optical fibers, wired our planet, first allowing for affordable intercontinental communication, then empowering the growth of the internet. Today's data traffic reaches the enormous levels of ~30 TB/sec IP traffic around the world (2) and probably much more in data centers. Roughly at the same time, the solid state electronics field was developed by the invention of the Silicon (Si) transistor and the creation of the Si industry, particularly the complementary metal-oxide semiconductor (CMOS) technology patented in 63 (3). This technology showed the fastest evolution rate by doubling transistor count every 2 years, reducing its minimum feature size from a quarter of an inch (4) in 1954 to a less then 100nm now days. Interestingly, these two technologies have some opposite strengths and limitations. While optical communication is broadband and almost lossless (hence carry signals long distance), it generally utilizes, more expensive, large components either because of low light-matter interaction or because of low index contrast that disable sharp waveguide bands. Alternatively, Si based electrical systems relay mostly on electrical communication through Cupper (Cu) lines. These metal lines have high loss in carrying electric and electromagnetic signals over small distances and extremely limited in their bandwidth. Nonetheless, CMOS technology features low cost micron scale systems; it allows for easy, well establish, micro- and nano-scale components and therefore cheap miniature systems in mass production. Fig. 1.1 (5) shows the difference in loss between coax cable and optical fibers over 100m as a function of frequency.

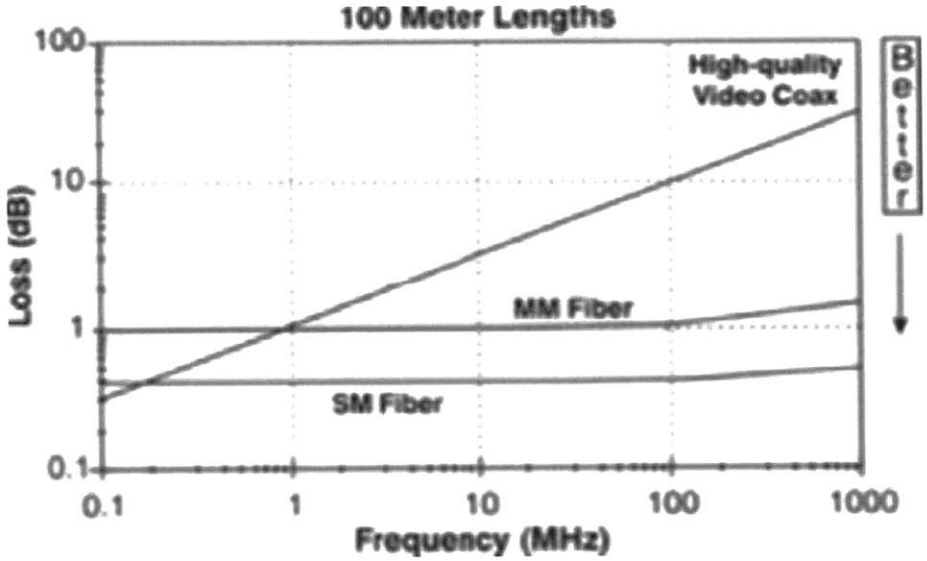

Fig. 1.1 Curtesy of (5) - comparison of signal transmission loss for 100-meter long single mode (SM) fiber, multimode (MM) fiber and high-quality video coaxial cable

Combining these two technologies into a rather new field called *Si Photonics* enables on-chip electro optical systems that harness the good of each technology without carrying any of the weaknesses mentioned above. Amazingly, the two technologies seem to merge perfectly well. Not only the two materials, Si as core material and Silicon-dioxide (SiO_2) as cladding are transparent in most of the IR spectrum, the large index contrast between the two enables very strong mode confinement in Si waveguides. This, in turn, allows for sharp bends and micron scale components. Fig. 1.2 shows a, dense, Si photonic system demonstrating about 4000 unit cells packed in to an area of just above $0.3mm^2$; each unit cell containing several components and waveguide bending of 2μm in radius (6). In addition, Si have two, electrical controlled, optical effects allowing for optical manipulation and opto-electric integrated systems – the thermo-optical effect which is strong and permit short components, and the electro-optical effect which is fast and allows for high speed systems. These advantages, together with the well-established Si industry, opens a vast number of opportunities for new, compact, low cost and low power consuming, systems that were out of reach 10 years ago.

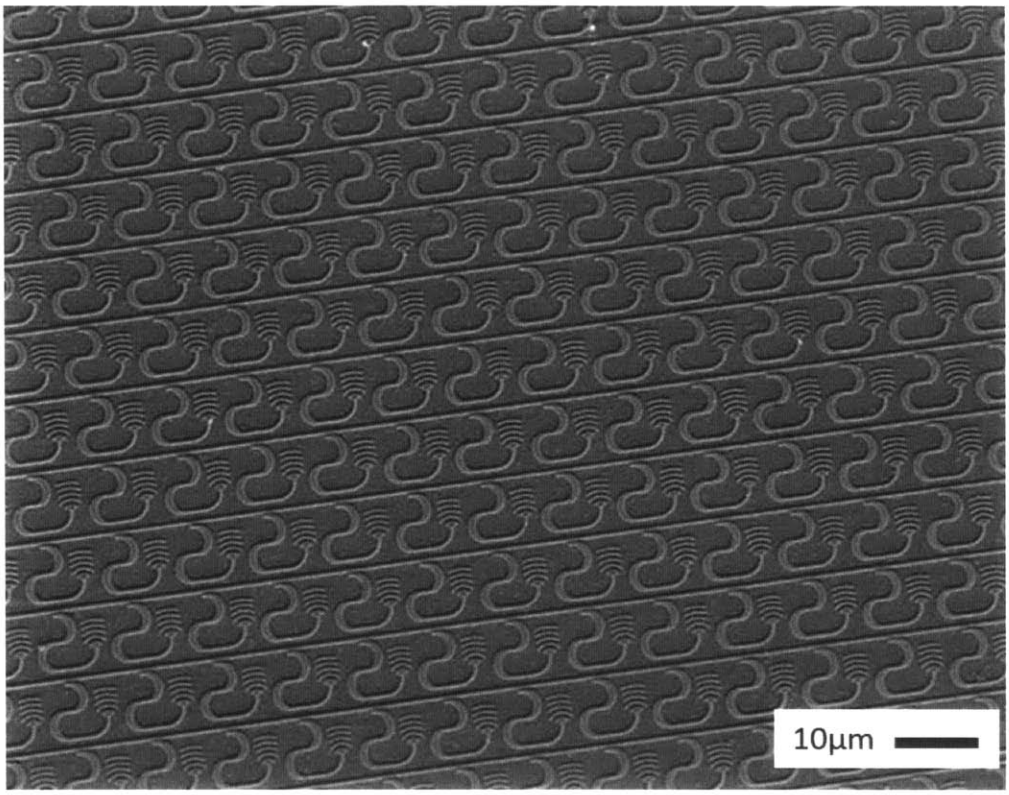

Fig. 1.2 a Scanning Electron Microscope (SEM) image of a dense fabricated Si photonics system showing several components packed into a unit cell area of only 9x9μm

Looking at the benefits of Si photonics and the technologies it grew from, it is easy to see why researchers were aiming the silicon photonics field mainly for on-chip data communication and as a link to fiber optic, longer range, communication (7), (8). The broadband low loss link, with high proximity to where the bits produced or sent to, creates the perfect communication channel for high speed data processing. Components like micro-rings tunable filters (9), Mach-Zhender modulators (10), Wave Division Multiplexers (WDMs) (11), on-chip photodetectors (12), (13) and more were quickly formed to address the optical link goals. Still, other types of systems are gaining more and more momentum from the same technology sometime using the similar components originally developed for communication requirements. One of which is the main focus of this work – Si based nanophotonic phased arrays (NPAs), the way they are constructed and possible applications are thoroughly presented here.

1.2 Optical Phased Arrays

1.2.1 Basic Theory

Phased arrays are arrays of antennas sharing a mutual feed with some phase control mechanism to regulate the phase of the electromagnetic wave emitted by each antenna. Constructed this way, Phased arrays produce a wave front pattern that agrees with a desired beam shape. For example, one collimated

beam emission in some azimuthal direction can be achieved by setting the phase of the different emitters to vary linearly along the array, with respect to azimuthal direction on the array plane, and create a flat phase front tilted to the desired beam direction. The tilt of the beam from the zenith direction directly depend on the variation rate of the phase along the array. Fig. 1.3 presents a side view of such a case where θ is the tilt from zenith angle, and the linearly grows of the phase along the array from, left to right, can be seen in the single antenna phase circles' radiuses.

However, controlling the phase and amplitude of each emitter can also generate a three dimensional image. By mimic the wavefront phase (and possibly but not necessarily amplitude) of a given background, one can create a hologram of this background. Moreover, it is also possible to take the wavefront of a specific object and by calculating its time reversal propagation, mimicking it's phase and amplitude on the array to create a three dimensional image in front of the array (between the array and the viewer). For example, in order to create a hologram of a point source in space in front of the phased array, one only needs to tune the array phases to create a spherical converging phase front. A spherical diverging phase front will appear as a hologram of a point source behind the array.

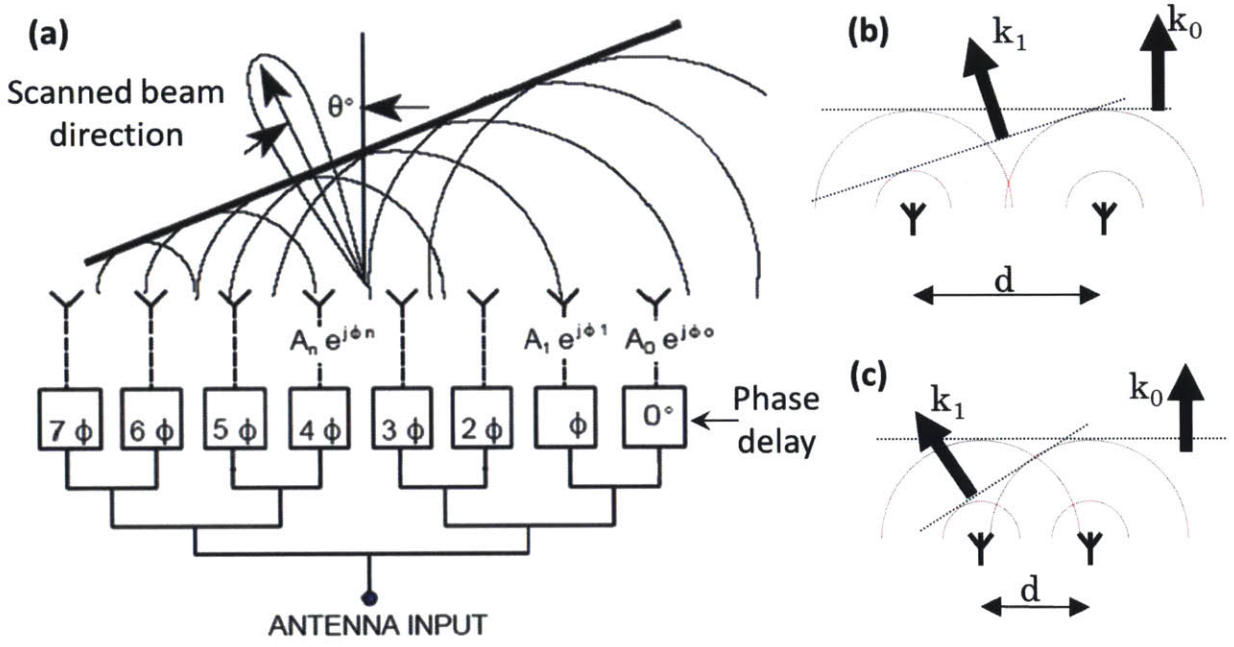

Fig. 1.3 Phased array basics: (a) Schematic illustration of a beam steering with a phased array. The phase delay increases linearly from left to right, supporting a flat phase front tilted to the left and a collimated beam in that direction. (b) and (c) illustration of higher orders emit from a phased array and their dependent over antenna pitch where (b) shows large spacing and close orders and (c) shows small antenna spacing and higher separation angle between beams.

When designing a phased array, the first fundamental limit one should consider is the higher orders constructively interfered. These will create higher order images/beams in unwanted direction. Using Fourier theorem for far field paraxial radiation and looking at the phased array radiation Fig. 1.3(b), one

can easily see that the radiation pattern emitted from a series of discrete emitters translates by Fourier transform to periodic radiation pattern in the far field. The period angle in far field is, then, proportional to the wavelength and inverse proportional to the emitter spacing (i.e array unit cell size). Removing the paraxial approximation, Fourier optics does not hold any more but the constructive characteristic of different modes is still in effect as can be seen in the difference between Fig. 1.3(b) and (c) (see Appendix A for more information) and the relations to wavelength and unit cell size still hold. Walking through the exact formulation it turns out that in order to eliminate side beams when main beam points forward, the unit cell size should be less than one wavelength and half wavelength to eliminate additional beams when main beam points parallel to the surface of the array. This may be trivial to deal with at low frequency or RF, but at the optical spectrum requires the unit cell to be on the micron scale size.

1.2.2 From RF to the Optical Spectrum

Phased arrays are common in the RF regime and are being used mainly for radar and communication applications where they are operated up to the Extreme High Frequencies (EHF). They inhabit fast communication links (14), the Ballistic Missile Early Warning System (BMWES) and PAVE Phased Array Warning System (PAVE PAWS) (15), fighter plane nose radars (16), naval radars (17) and more. For these systems phased arrays are mainly used to steer transmitted beams or identify the direction where a received energy came from.

Still, the physics behind these devices is not limited to the RF spectrum. Using same components built differently than for RF, phased arrays can also be built in the optical regime (wavelength < 10um). Transit the phased array technology to the optical regime opens a large number of applications to aim for. Light radars (lidars) are the straight forward analogy to radars in the RF regime and free space optical communication systems are the transformation from phased array base RF links, but optical phased arrays can also be used for other systems. 3D video displays (18) structured light for 3D imaging (19) and angular momentum control for multimode fibers communication (20) are only few example of how optical phased arrays can impact our lives in the future.

Reducing the wavelength to the optical spectrum inherently requires scaling of the unit cell (a cell in the array) by the approximately same ratio. This, while allows for miniaturized systems, also brings challenge; new components of a micron scale size should be designed. Several methods to address this challenge like the use of Micro Electro Mechanical Systems (MEMS) mirrors (21) and liquid crystal based transparent media (22) were applied. Still, the benefits of Si photonics, as described above, suggest a good platform to address this challenge in even more compact way. Indeed, Si based Nanophotonic Phased arrays (NPAs) are being researched since the end of the last decade and some progress has been demonstrated (23), (24). Yet, the 2 dimensional characteristic of Si based fabrication oblige the need for

new architectures to split the energy, control its phase and feed each cell in the array in a way that allow for electrical steering in two directions, wide angle steering, wide angles between different orders and fast steering.

This work deals with the challenge of creating an efficient and scalable NPA on a Si photonic platform. Chapter 1 walks through the basic optical components of a NPA and how to design them to be effective and in the small footprint necessary for the small unit cell size. Chapter 1 brings two futuristic designs of metallic nanoantennas that are more efficient in rapidly extracting the light out of a waveguide. Chapter 1 describes the first design known to us of a 2D electrical steerable Si based NPA of its kind, its architecture, fabrication and experimental results. This work, then, shifts to focus on possible applications with the first part of chapter 1 describing a NPA for lidar applications, its architecture, fabrication and experimental results, the second part of chapter 1 describing how we construct a lidar system using this NPA. Additional work on different possible applications – holographic displays and control of photon angular momentum are, then, shortly mentioned in the summary chapter.

2 Architecture and Elements of Nanophotonic Phased Arrays

Nanophotonic phased arrays (NPA), like any phased arrays, include a series of emitters (antennas) fed from a common coherent source, where each emitter's optical phase is controlled to form a desired wave front at the near field. As such, three main components are clearly needed in any NPA: couplers or splitters to divide the input energy between the set of emitters, phase shifters to control the relative phase of each antenna and optical antennas to emit (or couple) the energy to free space. This chapter describes, in Section 2.1, the different available architectures of realizing a NPA and the specific advantages of each of the architectures. Sections 2.2, 2.3 and 2.4 refer to the different components (power splitters, phase shifters and antennas respectively) and how they are designed. Sections 2.2 and 2.3, which deal with power splitting and phase shifting designs, are partly based on work done with Dr. Jie Sun et al (25). Section 2.1 is general for its architectural nature and Section 2.4 is a general overview of antenna design. The design and usage of each of the different antennas is described in more detail in the following chapters.

2.1 Architectures

As stated above, NPAs include three main components: a way to split the coherent energy to different antennas, phase shifters to control the relative phase of each antenna and the antennas themselves. It is important to note here that in the case of a phased array that acts as a receiver, it is more accurate to describe the splitters as combiners, combining the energy collected by the antennas to the output waveguide, but the actual components do not change. The three building blocks can be arranged in different ways. Fig. 2.1 shows the basic technique to combine different architectures of these building blocks sequentially to form possible NPAs. First, the input waveguide is split into N channels. This can be done, for example, using cascade coupling to each channel, tree shape coupling or utilizing a star coupler. Next, a phase shifter is applied on each channel, either one per channel, which is simple but requires a Look Up Table (LUT) to steer the beam in each direction, or different phase shifting length/strength per channel to allow steering with one signal. Lastly, optical antennas are applied at the end of each channel to couple the light in the waveguide with the free space beam. Antennas can be grating based or metallic structures. The basic design of NPAs consists of combining the three components in three different levels where each level works independently.

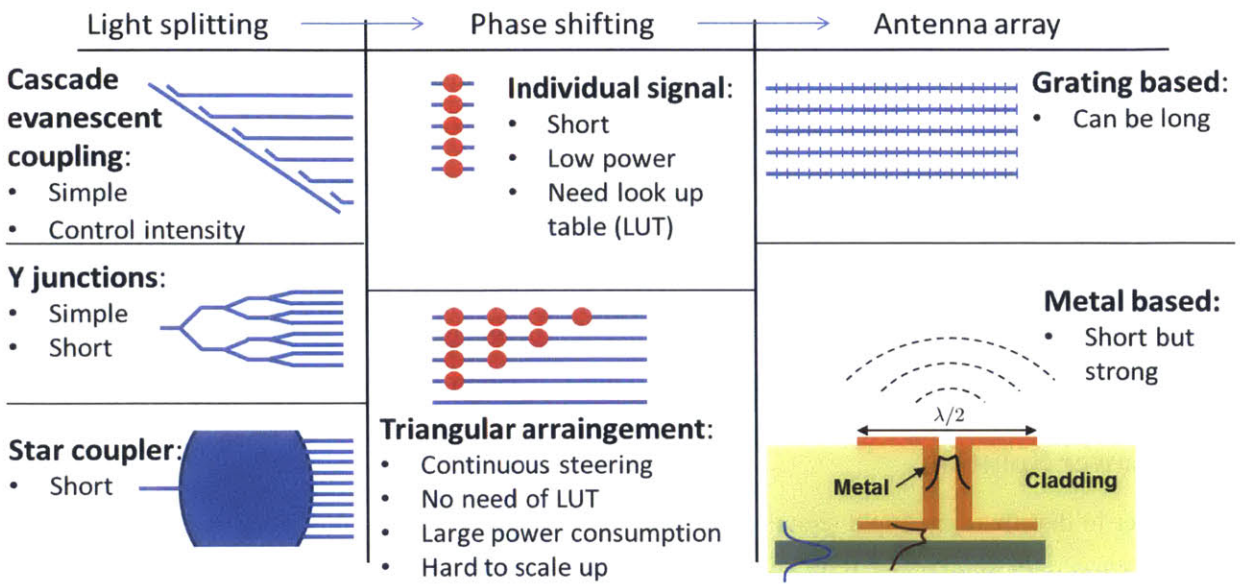

Fig. 2.1 NPA components: Different methods of separately realizing each of the three building blocks and combining them to create a NPA. Starting from distributing the power between the array's unit cells, then controlling the phase of each unit cell's wave and ending with coupling the power and emitting it to free space. The figure elaborates on the advantages and disadvantages of each method and the red spots represent phase shifters.

For light splitting, a star coupler or Multimode Interferometer (MMI) splitter (26) enables the shortest way to split the light. In splitting to a small number of waveguides (typically less than 8), it is possible to design one coupler to distribute the light between all channels. Nevertheless, the design of such couplers becomes more challenging and sensitive to fabrication errors as the number of outputs increase. Alternatively, a tree of cascaded 1x2 couplers (MMI based or other type) is simple to design and robust without limitation on the number of channels. The length of this type of splitting grows as log(N), which is not an issue with short couplers, but still limits the use when a design of large number of channels are attempted to be done with long adiabatic couplers (27). In this work, we generally use the cascade splitting with directional couplers for its simplicity in up scaling and ease of power control between the different channels. The short length of these couplers allows them to be part of the unit cell, hence, supporting easy up scaling, as described in (6), where 64x64 antennas passive NPA is demonstrated. Chapter 1 and Section 6.1.1 use this method in two levels in order to create a 2D grid of antennas. In Chapter 1 and Section 6.1.2, we combine the cascade splitting with the phase shifting to create a cascaded phase shifter which allows for beam steering using one signal.

Phase shifting, when done separately from splitting, can be done either by having one phase shifter for each channel (unit cell) or by having linearly increasing amount of phase shifting length for each channel to allow for one signal steering (28). The latter, although simple to control, does not scale up easily and requires area and power consumption which are scaling on the order of N^2. In Chapter 1 , we use the method of one phase shifter per channel. While this method requires a LUT to determine the

phase arrangement for each direction, it allows the phase shifter to be embedded in the unit cell, and therefore easily scalable. Moreover, it suits for arbitrary phase patterns, which are needed for holograms and focusing. In Section 6.1.1, we use the same principle but place the phase shifters after the optical antennas so the phase shifting is done in free space rather than in the waveguide.

As for optical antennas, there are two main approaches which one can use in order to couple a bound mode into free space (or vice versa). Chapter 1 describes the design of two metallic resonators as vertical couplers, and Chapters 1, 1 and 1 make use of a variety of grating based couplers, each one optimized for the specific type of NPA. Next, we describe in detail our realization for each component.

2.2 Power Splitting

In order to distribute the input signal between the different antennas, in this work, we use the cascade splitting design with evanescent field couplers, also known as directional couplers, where the lengths of the couplers control the portion of light dropped into each antenna unit.

Using Si or Si_3N_4 waveguides, the directional coupler evanescently couples light from the main bus waveguide to the waveguide leading to each unit cell. When two waveguides are placed within proximity of each other, each waveguide imposes a perturbation on the other waveguide. The effect of this perturbation can be theoretically understood using a method known as Coupled Mode Theory (CMT). This method is described in more depth and in the time domain in Appendix A . Here we will briefly explain CMT for propagation in a single direction when the two propagating modes are defined in the two remaining dimensions. Starting from Section 7.6 in (29), and assuming a coupling coefficient between the two waveguides to be κ_{12} *or* κ_{21}, we can linearly approximate the coupling between the two waveguides as

$$\frac{da_1}{dz} = -j\beta_1 a_1 + \kappa_{12} a_2 \qquad \text{Eq. 2.1}$$

$$\frac{da_2}{dz} = -j\beta_2 a_2 + \kappa_{21} a_1 \qquad \text{Eq. 2.2}$$

where a_i is the mode field intensity and β_i is the propagation constant of the i^{th} waveguide without a perturbation. Assuming a z dependence of the combined field in the waveguides of $e^{-j\beta z}$ and solving Eq. 2.1 and Eq. 2.2 we find the eigenvalues β to be

$$\beta_{a,b} = \hat{\beta} \pm \sqrt{\delta\beta^2 - \kappa_{12}\kappa_{21}} \qquad \text{Eq. 2.3}$$

where $\hat{\beta} = (\beta_1 + \beta_2)/2$ and $\delta\beta = (\beta_1 - \beta_2)/2$. For two waves propagating in the same direction $\kappa_{12} = \kappa_{21} = -|\kappa|^2$, the two eigenvectors are

$$a_{a,b} = \left(-\frac{\delta\beta}{\kappa} \pm \sqrt{\left(\frac{\delta\beta}{\kappa}\right)^2 + 1} \right)^{1} \quad \text{Eq. 2.4}$$

representing the symmetric and antisymmetric modes. For all the cases given in this work, the two waveguides are similar and $\delta\beta = 0$ so the normalized eigenvectors and eigenvalues are simply

$$a_a = \frac{1}{\sqrt{2}}\begin{pmatrix}1\\1\end{pmatrix},\ a_b = \frac{1}{\sqrt{2}}\begin{pmatrix}1\\-1\end{pmatrix} \text{ and } \beta_{a,b} = \hat{\beta} \pm \kappa. \quad \text{Eq. 2.5}$$

In the case of a directional coupler, light is entered into the coupling region with energy in waveguide number 1 alone, therefore, the field distribution at z=0 is $a_{(z=0)} = (1,0) = (a_a + a_b)/\sqrt{2}$. One propagates this field in z by evolving each eigenvector with its eigenvalue, substituting the eigenvectors and eigenvalues from Eq. 2.5 gives us

$$a_{(z)} = \frac{1}{\sqrt{2}}\left(a_a e^{-j\beta_a z} + a_b e^{-j\beta_b z}\right) = \frac{1}{2}\begin{pmatrix}e^{-j\beta_a z} + e^{-j\beta_b z}\\ e^{-j\beta_a z} - e^{-j\beta_b z}\end{pmatrix} = \begin{pmatrix}\cos(\kappa z)\\ -j\sin(\kappa z)\end{pmatrix} e^{-j\hat{\beta}z}. \quad \text{Eq. 2.6}$$

Therefore, the energy splitting between the two waveguides as a function of z will follow

$$|a_1|^2 = \cos^2(\kappa z) \text{ and } |a_2|^2 = \sin^2(\kappa z) \quad \text{Eq. 2.7}$$

in the input waveguide (number 1) and the drop waveguide (number 2) respectively. Eq. A.12 in Appendix A describes, in more depth, what affect the magnitude of the coupling coefficient. Nevertheless, it can be easily understood that as much as we place the two waveguides closer to each other, their modal fields interact more with the perturbation the other waveguide impose and κ increases.

Therefore we see that the power coupling coefficient of the directional coupler can be adjusted by two parameters (see inset in Fig. 2.2):

- The coupling length (L), which represent the z point in Eq. 2.7 where the two waveguides are being separated, and,
- The coupling gap (g) between the drop and the bus waveguides which controls κ.

Since a short coupling length is preferred in order to reduce footprint, the preferred coupling gap is the minimal etch line width allowed by the fabrication process; a 100nm in our case. A typical directional coupler and its L and g values are shown in the insert of Fig. 2.2. In addition, small scattering losses at the beginning of the coupler and at the waveguide bending point imply that the coupler's design needs to be based on the energy extracted from the bus rather than coupling to the drop port. This is important for the cascaded splitting architecture, which is sensitive to errors in the power remaining in the bus. As light propagates along the bus, small inaccuracies in extraction will accumulate and cause large variations in the power remaining to be dropped to the last emitter unit cells. This, in turn, will cause unwanted power fluctuations between each emitter of the NPA.

Using a 3D Finite-Difference Time-Domain (FDTD) simulation (described in more depth in Appendix A), the power extracted from the waveguide at different coupling length for 400x220nm (WxH) cross section Si waveguides and 1550nm wavelength was calculated and fitted to the $1-\cos^2(\kappa z)=\sin^2(\kappa z)$ theoretical curve driven from Eq. 2.7 with three additional degree of freedom. Fig. 2.2 shows the extraction in dB as a function of coupler length. The power extraction changes from 4% to 50% when the coupling length varies between 0μm to 2.5μm and coupling gap is a constant 100nm. The fitting curve for this power extraction was chosen to be

$$Ext = A * \sin^2(\kappa L + B) + C \qquad \text{Eq. 2.8}$$

where $A = 0.99$, $\kappa = 0.229 Rad/\mu m$, $B = 0.18 Rad$, $C = 0.01$. The parameter B has been inserted to the fit to accommodate a small coupling resulted at the waveguide bending, C has been inserted in order to accommodate bending loss in the bus waveguide and was simulated to be 1%, and A is set not to exceed $1-C$ for power conservation.

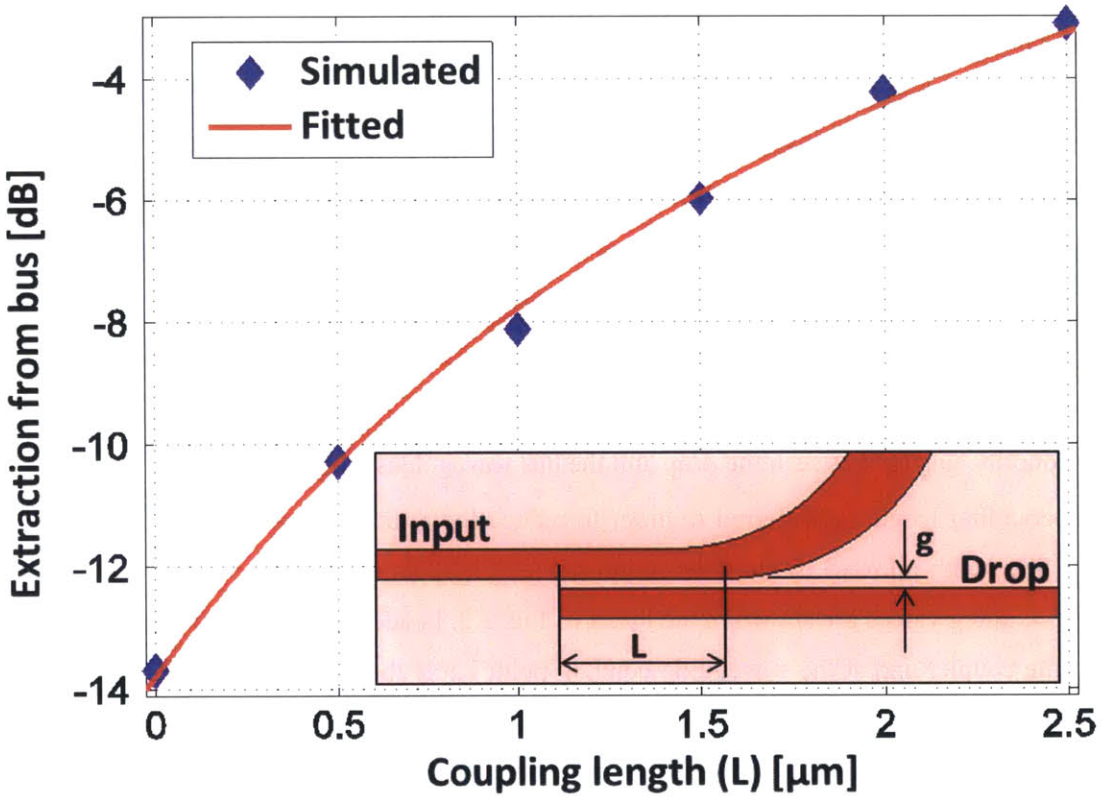

Fig. 2.2 Design of the directional coupler: The power extracted from the bus as a function of the coupling length. Insert shows the coupler architecture as simulated. Adiabatic bending and widening in the waveguide seen here is related to the phase shifter and explained in the next part of this chapter.

When coupling from one bus to N channels in a NPA with designed near-field intensity distribution $|w_n|^2$, the power-extraction coefficient of the n^{th} coupler to the n^{th} antenna unit is given by

$$Ext_n = \frac{|w_n|^2}{|w_{end}|^2 + \sum_{j=n}^{N}|w_j|^2} \quad \text{Eq. 2.9}$$

where $|w_{end}|^2$ is the residual power discarded at the end of the buss. w_{end} is usually determined by the maximal coupling enabled by the directional coupler given a maximum coupling length available in the unit cell. The denominator in Eq. 2.9 is simply the power available in the waveguide before the n^{th} coupler so the value of the extraction is simply the part of the available power which needs to be dropped. Using Eq. 2.9, combined with the FDTD simulation in Fig. 2.2, any near-field emission profile $|w_n|^2$ can be achieved in the NPA utilizing the proposed optical power delivery network based on the cascaded directional couplers. Most NPAs require uniform near-field emission, that is, $|w_n|$ constant across the whole array. Then, the extraction coefficients in Eq. 2.9 becomes

$$Ext_n = \frac{1}{|w_{end}/w_n|^2+N-n}. \quad \text{Eq. 2.10}$$

In order to address aberrations in the NPA output emission, we look at the phase response of the couplers. Although Eq. 2.6 predicts no phase change on the bus waveguide and constant 90° phase shift on the drop port, in reality, different coupling lengths and gaps cause small phase variation through the bus and in the drop port. While the phase on the drop port effects only a single emitter, the phase in the bus waveguide is accumulated over the set of cascaded couplers. Nevertheless, a linear phase change as a function of unit cell number only presents extra steering in the emission angle; it is the deviation from linear curve that allow the phase to cause aberrations in the emitted beam. This deviation from linearity of the drop port phase and accumulated bus phase is shown in Fig. 2.3 as a function of the unit cell number. It can be seen that in this case of, 23 antennas, the phase error does not exceed 1 Rad (~15% of a wavelength) and this value can be halved when omitting one or two antennas at the end of the phase array. In some parts of this work (Chapters 1 and 1), these phase changes were ignored for their negligibility. In Chapter 1, on the other hand, these phase differences were corrected by applying extra waveguide path inside the phase shifter section. Since in large arrays most of the couplers require splitting only a small amount of power off the bus waveguide, these couplers also share a similar structure (short length) and naturally have the same phase response. Hence, in large arrays, where the majority of couplers look alike, the need to account for the phase different is reduced. In all results of this work, the far field spot size is found to be close to the diffraction limit showing minimal aberrations.

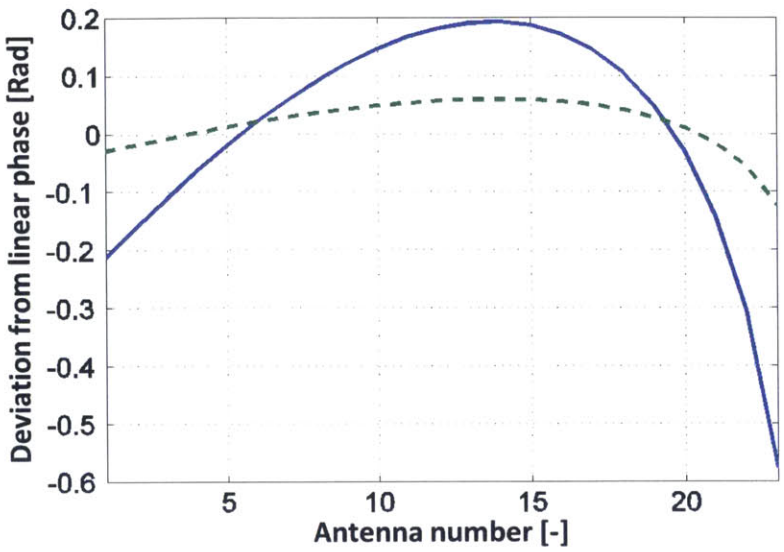

Fig. 2.3 Phase change caused by directional coupler: Deviation from linearity on (dashed green line) drop port phase and (blue solid line) accumulated bus phase.

When designing a directional coupler, coupling strength as well as phase changes, available length and other fabrication and practical considerations should be taken into account, but the flexibility and small footprint of these couplers enable sturdy design under tight constraints. When designed correctly, a cascaded splitting allows distribution of power to a large number of antennas with a short footprint per antenna.

2.3 Phase Shifting

The purpose of the phase shifter in a NPA is to provide an accurate relative phase φ to each optical antenna. Although in passive phased arrays this phase shift can be introduced statically by an optical delay line, in this work we focus on dynamically controlling this phase through electrical signals.

It is desirable to have a tunable phase shifter, where the optical phase can be actively adjusted to achieve 2π tuning range within each phase shifter. Moreover, for compatibility with integrated electronics, it is critical for the phase shifter to be power-efficient. The strong thermo-optical effect has been widely used in silicon photonics' tunable phase shifters (30), (31), (32) to obtain a large phase shift in short footprint. Most of these phase shifters utilize the over-cladded metal heater that is separated from the waveguide by a layer of dielectric to prevent excessive optical loss from the metal. However, this dielectric layer, sandwiched between the metal heater and waveguide, represents a large heat resistor and makes the thermo-optic tuning time constant $\tau \sim RC$ longer. The over-cladded metal heater is also less power-efficient since it loses more heat directly to the cladding without contributing to the phase shift. Moreover, metal heaters will always have a higher temperature than the Si waveguide limiting the Si temperature to under the metal melting point. To overcome these challenges, thermo-optic heaters can be

directly formed within the silicon waveguide (33), (34), (35), (36), (37), enabling much more efficient and fast heating in a highly compact phase shifter that can fit within, an adequate size, unit cell.

As shown in Fig. 2.4(a), the integrated heater is formed by doping the silicon waveguide to create a resistive heater within the waveguide. The heater is electrically connected to contact metals through two silicon leads that are directly attached to the waveguide. The silicon waveguide is lightly doped to provide a considerable resistance and to avoid significant optical loss from the dopants. The silicon leads are heavily doped to reduce the contact resistance so that most of the heating power is produced at the waveguide. In addition, a zigzagged structure of the silicon leads was implemented in some cases to increase leads length and provide better thermal isolation between the waveguide and the metal contacts. This isolation is important to prevent the metal contact from melting at high waveguide temperatures. In fact, these leads allow the Si waveguide to reach temperatures higher than the via and metal melting points. This, in turn, continues to shorten the required length of the phase shifter and releases the requirement of using high melting point metals.

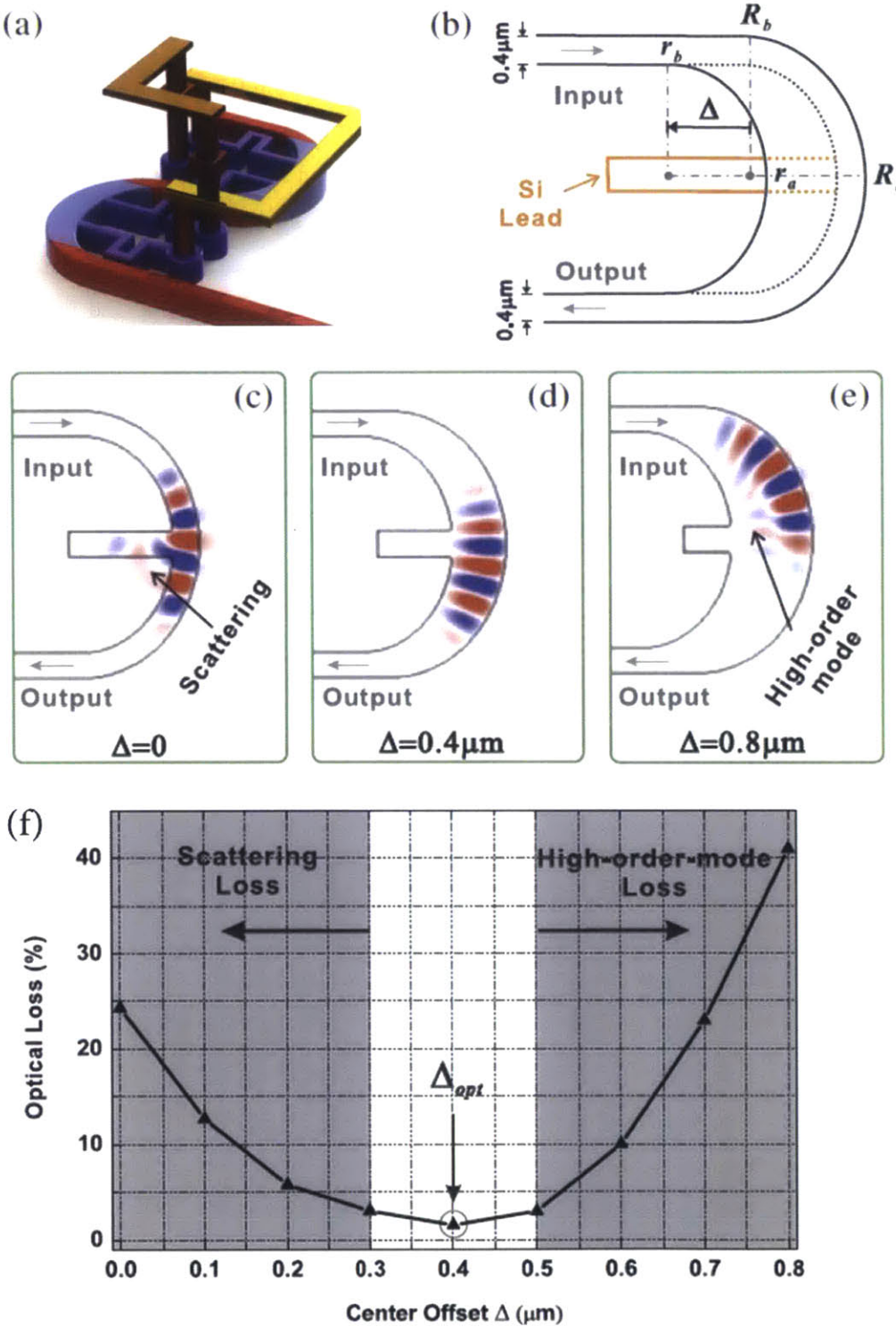

Fig. 2.4 Tunable phase shifter with adiabatic bend: (a) A 3D schematic figure of the phase shifter design showing the intrinsic waveguide (red), the lightly doped section (blue), the highly doped Si leads (purple) and the vias and metal lines fidding the heater (brown and gold). (b) A schematic drawing of the adiabatic bend in the tunable phase shifter and its parameters. The 3D-FDTD simulation of light passing through a waveguide bend with a silicon lead, where the center of the inner ellipse is offset by different distances Δ to form an adiabatic bend: (c) Δ = 0, (d) Δ = 0.4μm, and (e) Δ = 0.8μm. (f) The 3D-FDTD simulation of the optical loss from the adiabatic bend with an attached silicon lead. The optimal offset is Δ_{opt} = 0.4μm. Figure modified from (25)

The directly integrated silicon heater gives the most power efficient thermo-optic phase tuning because the waveguide itself has the highest temperature; however, the intimate contact of the silicon lead with the optical waveguide could cause severe optical losses due to light scattering. As shown by the FDTD simulation in Fig. 2.4(c), substantial scattering loss is observed when light is passing through a waveguide bend with a directly connected silicon lead. Fortunately, this contact issue was solved by our group's recently developed adiabatic bend structure (38), which enables low-loss contact with integrated heaters (33), (34), (35), (36) as well as *p-n* junctions (39) in various silicon photonic devices. Fig. 2.4(b) illustrates the adiabatic bend used in this study. The outer edge of the waveguide bend follows an elliptical curve with R_a = 1.7μm and R_b = 2.0μm. The inner edge is also an ellipse with r_a = 1.3μm and r_b = 1.7μm. The centers of the two, inner and outer, ellipses are offset by distance Δ. This offset gradually, or adiabatically, widens the central part of the bend. This widening together with the waveguide bending pushes the optical mode to the outer side of the waveguide so the silicon leads can be introduced to the inner part where there is little optical field. In this way, the scattering from the silicon leads is greatly reduced, as shown in Fig. 2.4(d). However, when the offset is too large, higher-order modes will be excited because the waveguide widening is too abrupt to be considered as an adiabatic transition, causing excessive radiation loss when transitioning back to a single-mode waveguide, as simulated in Fig. 2.4(e). As a result, there exists an optimal offset distance Δ_{opt} that causes the lowest loss. Fig. 2.4(f) simulates the optical loss of the adiabatic bend at different offset distances, where it shows the optimal offset is Δ_{opt} = 0.4 μm, corresponding to a width of 0.8μm in the center of the adiabatic bend. The scattering loss dominates when the offset is smaller than 0.4μm, while the excitation of high-order modes is responsible for the loss when the offset is larger than 0.4μm. The total optical loss is 1.5% per curve at the optimal point. The material loss caused by the lightly doped waveguide is about 3dB/mm at a typical *n*-type doping level of 1×10^{18} cm^{-3} (40), corresponding to a negligible propagation loss of less than 0.5% in the sub-10μm doping region. In more recent work, we increased the outer radius to $R_a = R_b$ = 3.0μm, the inner ellipse size to r_a = 2.5μm and r_b = 2.6μm and the ellipses offset to Δ_{opt} = 0.9μm and achieved 0.5% loss per curve which allows for cascaded phase shifting as described in Section 5.3.3.

Fig. 2.5 shows a COMSOL™ simulation of the heat distribution in a similar phase shifter. Two important points can be seen in this figure: First, the metal contacts temperature stay low and hardly affected by the high temperature of the waveguide. Second, the heat flow quickly through the waveguide, warming longer section of it and allowing even more efficient phase shift. A high-efficiency, low-loss thermo-optically tunable phase shifter is made possible using the directly integrated silicon heater and the adiabatic bend.

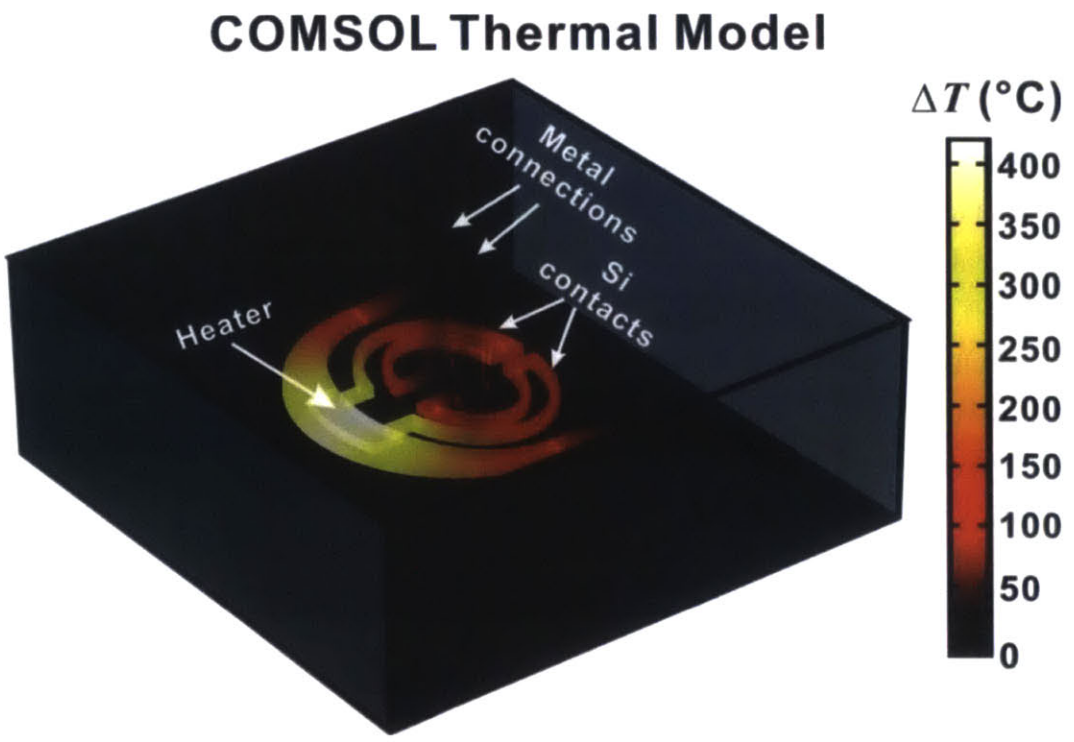

Fig. 2.5 Thermal Simulation: COMSOL™ thermal simulation of a phase shifter, showing the low temperature of the contacts and the heat propagation along the waveguide. Figure edited from (36)

This phase shifter was fabricated in a Mach-Zhender interferometer architecture and the switching time constant was measured (36). Fig. 2.6 shows the time response and the rising and falling time constant to be τ_{heat} = 2.2μs and τ_{cool} = 2.4μs. The author of this dissertation associates the 0.2μs delay in cooling time to the slower electric power turn-off so that the real phase shifter time constant is simply τ = 2.2μs. Moreover, it can be seen from Fig. 2.6 that a π phase shift can be achieved with 13mW electric power only. The use of the strong thermo-optical effect for phase shifting allows for small footprint phase shifters, and the above described method for directly heating the waveguide enables fast temperature changes and phase control together with low power consumption. Waveguide conducted thermo-optical phase shifters are the best alternative for phase shifting in NPA and are used widely in this work.

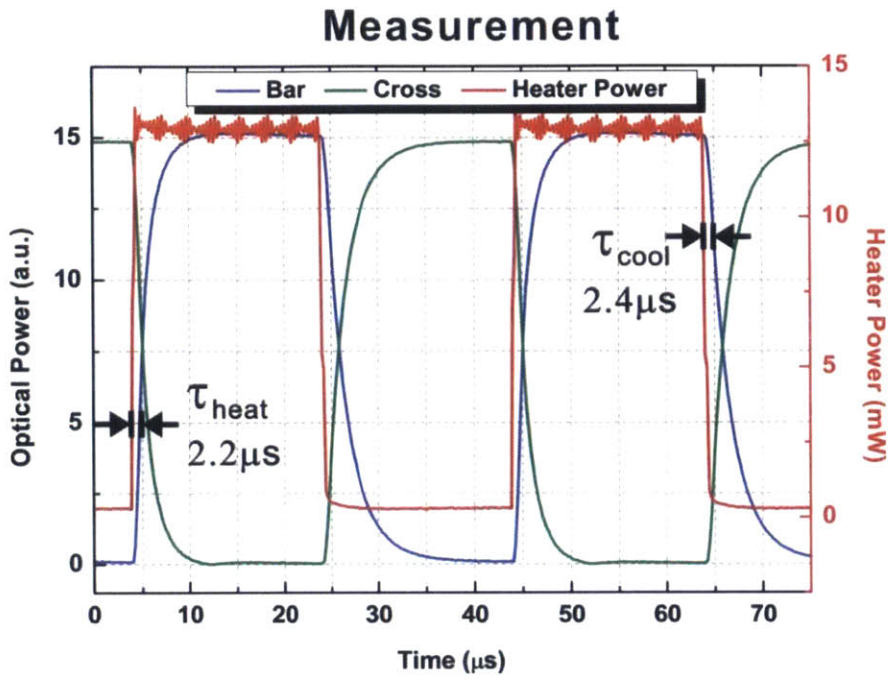

Fig. 2.6 Phase shifter response: time response of waveguide conducted thermos-optical phase shifters as elements in a Mach-Zhender interferometer showing the time constant of these phase shifters to be 2.2μs. Courtesy of (36).

2.4 Optical Antennas

Optical antennas as vertical couplers, devices that take a pulse of light traveling in a waveguide and couple it vertically out of the chip or (vice versa), have been widely researched mainly for coupling between a waveguide and a fiber. There are two main approaches in the literature addressing this coupling: metallic based antennas (41), (42), (43), (44) and, the more common, grating based antennas (45), (46), (47). Although some metallic based antennas were tested at early stages of this work (see Chapter 1), most results were demonstrated with a fabrication process that did not include a metal layer with optical proximity to the waveguide. For the majority of this work, grating based couplers were used in order to couple the light from the waveguide bound modes to free space. Two different grating based antenna concepts were used: a short antenna for point source-like emitters, described in Chapter 1 and 1, and a long antenna for 1D steering arrays fed from one side and requiring a large aperture, described in Chapter 1. This section describes the fundamentals of grating based antennas and how to design them to fit certain requirements. The specific design of each antenna (grating or metallic based) is described in the corresponding chapter. It is important to note here that whenever coupling or emitting out from the chip is discussed, it is clear from reciprocity that both directions are possible and considered. For simplicity only, this work is written for antenna emission, but all theories, methods and results hold for receiver antennas in just the same way.

In order to gain some intuition on grating couplers, we use the coupling mode theory described in details in Appendix A . Starting with Eq. A.12 for two resonators, the coupling coefficient from the first resonator to the second resonator is

$$\kappa_{21} = -\frac{1}{4}\omega \int (\delta\epsilon_2 e_2^* \cdot e_1) dV. \qquad \text{Eq. 2.11}$$

e_i is the modes of the input field (i=1) and the output field (i=2) and $\delta\epsilon$ is the refractive index perturbation on the input mode's field (waveguide mode in our case) nonzero only in specific points of space. Looking at Eq. 2.11 we can see that in order to achieve a strong coupling coefficient κ_{21} between two different waves, $\delta\epsilon$ should generally be nonzero only in specific volumes in space. This is important in order to avoid integration of opposite signs. If we try to integrate a large, real, positive value, for example, $\delta\epsilon$ should be positive only in points in space where $(e_1^* \cdot e_2)$ real part is positive. For a specific case of coupling from a waveguide to a vertically propagating free space wave, looking along the waveguide, e_2 have a constant phase, and the periodic sign of $(e_1^* \cdot e_2)$ is one waveguide wavelength. Therefore, $\delta\epsilon$ should be nonzero for half of this period only and placed repeatedly at every one waveguide wavelength. In order to create a strong (short) vertical coupler, one needs to create a strong perturbation $\delta\epsilon$ only at space points where $(e_1^* \cdot e_2)$ constructively integrate.

Still, designing a grating based antenna requires more attention than just maximize coupling coefficient between the two waves. A strong grating with one wavelength period may also generate back reflection. Additionally, it may support coupling the waveguide mode to the down propagating free space wave. The way we address these two issues is by symmetry braking. It is easy to see that, in an up/down symmetric structure, the up emission will, by definition, be equal to the down emission and will never exceed 50% of the input power. Hence, in order to enable a strong upward emission without extensive loss to downward emission, the up/down symmetry must be broken. Fig. 2.7(a) shows an FDTD simulation image from Chapter 1, where a metal ground plane is used in order to break symmetry for our metallic antennas. This shows up to 60% up emission with most of the non-coupled light staying bound to the waveguide. Fig. 2.7(b) shows a FDTD simulation side view of our, short grating antenna design from Chapter 1. This design has one ridge etch grating, which brakes the up down symmetry enough to split the energy ~60%/40% between the up and down emission. A more complex method of breaking both up/down symmetry together with the forward/backward symmetry includes two layers of dielectric staggered in order to match the phases upward while destructively interfering them in the down direction. This method was used in Section 6.1.1 and illustrated in a FDTD side view image in Fig. 2.7(c). One can also understand this method as creating a set of tilted perturbation mirrors (dashed lines in the figure) to maximize up coupling while minimizing down coupling.

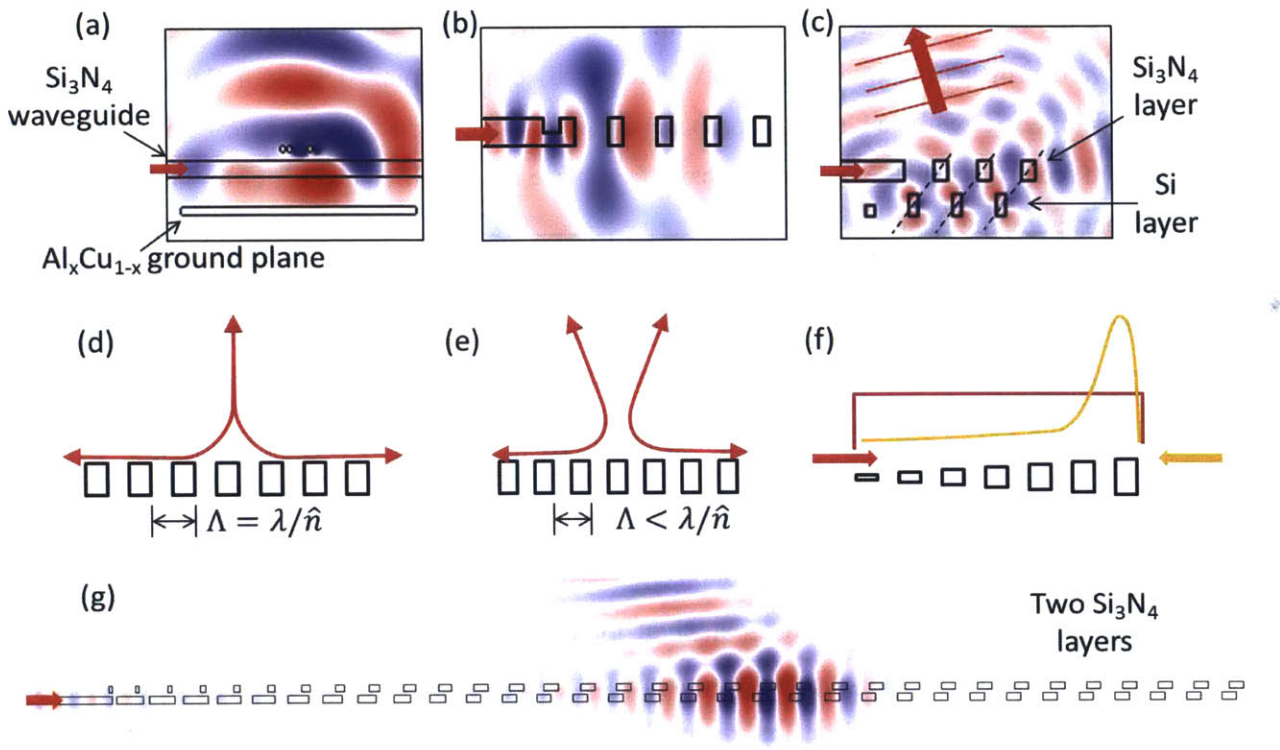

Fig. 2.7 Symmetry breaking in optical antennas: (a)-(c) 3D FDTD simulation images of three antennas showing the use of (a) metallic ground plane, (b) ridge etch and (c) staggered double layer for vertical symmetry breaking. (d)-(f) schematics of symmetry breaking on the propagation direction showing (d) a non-symmetry-broken grating, symmetry breaking by (e) emitting slightly backward and (f) strength variation. (g) a FDTD simulation of a Si_3N_4 waveguide to fiber coupler designed combining all these methods.

The need for breaking the forward/backward symmetry is less intuitive. Looking at Fig. 2.7(d) we can see that light traveling in both directions in the coupler emit to the same free space mode. Therefore, considering reciprocity, light propagating down from a free space radiation will, by definition, couple equally to both forward and backward propagating modes with no more than 50% efficiency to each mode. This limits the coupling between the waveguide mode and the free space mode to no more than 50% efficiency. In order to break this forward/backward symmetry, two methods can be applied. The first one does not break the symmetry of the structure itself, but the symmetry of its free space emission. By changing the period of the grating from $\Lambda = \lambda/\hat{n}$, where $\hat{n}$ is the average effective index, to a slightly longer or shorter period, as can be seen in Fig. 2.7(e), the emission direction of the antenna shifts forward or backward respectively. This in turn separates the two free space fields coupled to the forward and backward waveguide propagating modes, eliminating the reciprocity issue described above and allowing for each one of the fields to couple with more than 50% efficiency.

Another method of breaking the forward/backward symmetry is by varying the coupling strength along the antenna length. When using long grating, varying the perturbation strength from a weak

perturbation at the beginning to a strong one at the end of the antenna can be helpful. Fig. 2.7(f) shows how the forward propagating mode of a waveguide (red) can be coupled in to a flat top near field emission mode intensity while a backward propagating wave is coupled to a very narrow near field mode. It is clear from reciprocity that a uniform intensity free space mode will couple better to the left port than to the right port allowing the coupling efficiency to exceed 50%. One can also see this as a way to better hold the energy in the coupler grating. While a wave approaching from the right will be largely reflected from the first strong grating periods, a wave approaching the antenna from the left will be less perturbed by the week gratings and penetrate more into the antenna before being reflected. At that point, the wave is already deep in the antenna and the reflected energy will still see many gratings to couple with to free space. Finally, Fig. 2.7(g) shows an FDTD simulation image of a Si_3N_4 waveguide-to-fiber coupler designed, that is out of the scope of this work, using most of the methods mentioned above. It is clear in this image how most of the power is being coupled upward and only a small fraction emits downward.

Section 3.2 describes in detail another method for breaking the forward/backward symmetry with metallic-based antennas. We apply several resonators with different resonance frequencies, and therefore phase response, along the waveguide, in a way that the different phase responses compensate on the different location, so they all constructively interfere up wards.

As mentioned earlier, optical antennas for vertical coupling have been extensively researched mainly for the purpose of fiber coupling. Still, vertical couplers can also be used for NPAs. There are slight differences between the requirements for antennas for the two applications. While for fiber coupling a near field intensity pattern that matches the fiber mode and a flat phase is required, for phased arrays, the far field pattern is naturally more important. In fact, for 2D NPAs, the antenna is regularly considered a point source. Moreover, for this phased arrays, the main requirement of the optical antenna is its small size to fit within a small space in the unit cell. This is in order to have the higher lobe orders be far away from the main beam. This spacing not only needs to be populated with waveguide and emitter, but also with a phase control unit which is generally much larger than a wavelength.

We described here possible architectures and components to enable the construction of a NPA, ending with a theoretical analysis of a grating based antenna. In the next chapter, we describe two metallic antennas which are very small in size and can be good candidates for use in NPAs. In the rest of this document, we discuss only grating based antennas implemented into our arrays, some of which are small and designed to couple as much power as possible in a short length, and some are long for 1D NPAs and designed to allow a large aperture in the non-steerable direction.

3 Futuristic Optical Nanoantennas

While traditional vertical couplers are built using dielectric gratings on the wave guide, coupled mode theory, given in more details in Appendix A , show that the coupling coefficient of such emitters is proportional to the permittivity difference introduced by this dielectric grating. This permittivity difference is relatively low in dielectric grating based couplers and, thus, requires long structure to generate high coupling efficiency. As discussed above, it is important for 2D NPA antennas not to excide a certain length. Therefore, the introduction of another coupling method is important.

In order to do so, we introduce a small structure, low Q, metallic resonator which will provide a link between the waveguide and the emitted light. Metallic optical nanoantennas (48) have been proved to couple electromagnetic plane wave with a mode very small in space (49). Furthermore, being metallic, these structures introduce extremely high permittivity difference on the waveguide structure, providing strong perturbation to the waveguide and enhancing the coupling coefficient. Using the high permittivity difference of metallic perturbation on a dielectric resonator and the highly concentrated electric field of the metallic antenna mode, enable rapid coupling from the waveguide to the nanoantenna. The nanoantenna, in turn, radiates the energy to free space.

Nanoantennas and micro metallic structures have been studied for many photonic applications, some, with relation to vertical coupling applications (41), (42), (43), (44). Most of these previous arts show mainly copy and rescaling of RF antennas like dipoles (41), (50), bowties (51),Yagi-Udas (52), (53) and more. This structures being studied so deeply are good candidates for our task, but the way RF antennas are powered (using transmission line wire much smaller than a wavelength) is somewhat different than the way photonic nanoantennas are often driven. These antennas are often driven by a waveguide mode that is not much smaller than a wavelength. This mode tends to flow on the whole antenna structure rather than feeding a single point on it (as the case in RF). In this chapter we show two designs of new structures more suitable for Si photonics and for coupling light directly between a waveguide and a free space wave mode.

3.1 First Proposed Structure Rectangular Aperture Antenna

In this section we propose, theoretically investigate, and numerically demonstrate a compact design for a vertical emitter at a wavelength of 1550nm based on nanophotonic aperture antennas coupled to a dielectric waveguide. The structure utilizes a plasmonic antenna placed above a Si_3N_4 waveguide with a ground plane for breaking the up/down symmetry and increasing the emission efficiency. Three-dimensional finite-difference time-domain (FDTD) simulations (described more in Appendix A) reveal that up to 60% vertical emission efficiency is possible in a structure only four wavelengths long with a 3dB bandwidth of over 300nm and experimental results are shown to validate our simulation method. This section follows the theoretical work published as (54) and the experimental results published in (55).

3.1.1 Intruduction

Vertical input/output coupling in the telecom C-band (i.e. 1535nm $< \lambda <$ 1565nm) has been extensively investigated for the purpose of coupling to or from an optical fiber (56), (57), (58), (59). As a result, most vertical couplers to date have emission patterns matched to fiber modal diameters (~10μm). However, vertical coupling can also be used in Nanophotonic Phased Arrays (NPAs) (23), (24) to steer a beam or generate holograms. In such arrays, the desired emitter characteristics include strong waveguide-to-free-space output coupling and a compact structure (i.e. a few wavelengths long, or less). A short emitter length is critical to fitting many emitters in a small area and enabling wide rotation angles with a single lobe. However, demonstrations of efficient output coupling using short structures are uncommon, with minimum structure lengths of several wavelengths (57), (59). Most vertical couplers (with the exception of the metallic rods in (41), (60)) rely on gratings in semiconductors or insulators alone to perturb the electromagnetic field and efficiently emit. However, the extraction rate is limited by index contrasts available in dielectric structures. To overcome this limitation, we consider the use of metals to perturb the electromagnetic field and achieve efficient vertical coupling in a compact structure. We show that the inherent large permittivities and conductivities of metals enable large coupling coefficients and efficient output in a structure only a few wavelengths long. The specific structure designed here is a nanophotonic aperture antenna. However, the results here are general; designed properly, nanoantennas enable rapid emission from dielectric waveguides.

3.1.2 Theory

To gain intuition about the coupling between the nanoantenna and the waveguide, we treat the nanoantenna as a resonator using coupled-mode theory in the time domain given in more detailes in Appendix A and (29), (61). While coupled-mode theory assumes shape invariance of the modes and drops second order terms making it more quantitatively accurate with weakly coupled modes, coupled

mode theory provides useful insight even when modes are strongly coupled. However, for quantitatively accurate results, in this letter, we rely on three-dimensional full field simulations and show its agreements with real structures at the end of this section.

The differential equation governing the response of a resonator with energy amplitude a and coupling coefficient μ to a perturbing mechanism (e.g. a waveguide) with wave amplitude s (normalized to power) is, to first order,

$$\frac{da}{at} = \left(j\omega - \frac{1}{\tau}\right) a + \mu s \,, \qquad \text{Eq. 3.1}$$

where ω_0 is the resonant frequency, and τ is its decay rate. Since the resonator's amplitude define its energy, a is normalized to energy, the waveguide's amplitude, though, define its power and, therefore s is normalized to power. In a nanophotonic antenna, the loss mechanisms can be broken down into radiation, ohmic, and coupling losses, with decay rates τ_r, τ_o, and τ_e, respectively. From energy balance considerations, we have

$$\frac{1}{\tau} = \frac{1}{\tau_e} + \frac{1}{\tau_r} + \frac{1}{\tau_o} . \qquad \text{Eq. 3.2}$$

τ_e is taken only once here assuming the standing wave is not symmetric and couple only to the forward propagating waveguide mode. In case of a standing wave resonator which couple equally to both directions of the waveguide $2/\tau_e$ should be taken instead. The steady state solution to Eq. 3.1 with ω frequency input s is then

$$a = \frac{\mu s}{j(\omega - \omega_0) + 1/\tau} . \qquad \text{Eq. 3.3}$$

In order to find μ we look at the ring down case of the resonator assuming no loss or radiation, only coupling to the waveguide. From reciprocity we can write

$$s_t = s + \mu a \qquad \text{Eq. 3.4}$$

where s_t is the power on the output waveguide and $s = 0$ for the ring case. From energy conservation we can write

$$|s_t|^2 = -\frac{d|a|^2}{dt} = \frac{2}{\tau_e}|a|^2 = |\mu a|^2 . \qquad \text{Eq. 3.5}$$

Thus

$$|\mu|^2 = \frac{2}{\tau_e} . \qquad \text{Eq. 3.6}$$

Given that our goal is to maximize the ratio of the radiated power (Eq. (7) in (61))

$$|s_r|^2 = \frac{2}{\tau_r}|a|^2 \qquad \text{Eq. 3.7}$$

to incident power $|s|^2$, and assuming that τ_r remains constant, we substitute τ from Eq. 3.2 into Eq. 3.3, use $|\mu|^2$ from Eq. 3.6 with $\omega = \omega_0$ to maximize

$$\left|\frac{a}{s}\right|^2 = \frac{|\mu|^2}{1/\tau^2} = \frac{2/\tau_e}{\frac{1}{\tau_e^2} + \frac{1}{\tau_r^2} + \frac{1}{\tau_e \tau_r}} \qquad \text{Eq. 3.8}$$

and find the desired value of τ_e to be $\tau_e = \tau_r$ when ohmic losses are neglected. Going over the same math process with longitudinal symmetric resonator wave, which couple evenly to both directions in the waveguide ($1/\tau_e \Rightarrow 2/\tau_e$), would yield a maximum coupling when $\tau_e = 2\tau_r$. Substituting this value in Eq. 3.8 and then $|a|^2$ in Eq. 3.7 show the coupling to radiation cannot exceed more than half of the power traveling in the waveguide. This supports our note in Section 2.4 explaining that the longitudinal symmetry should be broken in order to allow more than 50% coupling.

The effect of changes to our structure on τ_e or μ can be estimated using coupled-mode theory. This section follows the formalism developed in (62) for time dependent coupling using volume integration and is therefore consistent with three-dimensional modes. Following Eqs. 2.13 to 2.16 in (62), we look at the power fed by the waveguide to the resonator mode

$$-\frac{1}{2} Re \int \mathbf{E}^* \cdot \mathbf{J} dV = -\frac{1}{4} \int (a\mathbf{e}_r)^* \cdot (j\omega \Delta\epsilon s \mathbf{e}_{wg}) dV + c.c., \qquad \text{Eq. 3.9}$$

where $\mathbf{e}_r$ and $\mathbf{e}_{wg}$ are the normalized modes of the resonator and waveguide respectively. $\mathbf{J} = j\omega\mathbf{P} = j\omega\Delta\epsilon s\mathbf{e}_{wg}$ is the polarization current due to the perturbation from the resonator and $\Delta\epsilon$ is the complex permittivity difference caused by the resonator. Looking at the energy change in the resonator

$$\frac{d|a|^2}{dt} = -\frac{2}{\tau} aa^* + \mu a^* s + \mu^* a s^*, \qquad \text{Eq. 3.10}$$

the power from Eq. 3.9 corresponds to the last two terms only ($\mu a^* s + \mu^* a s^*$). Comparing these two terms with Eq. 3.9, μ is given by

$$\mu = -\frac{j}{4}\omega \int \Delta\epsilon \mathbf{e}_r^* \cdot \mathbf{e}_{wg} dV. \qquad \text{Eq. 3.11}$$

In the formulation above, we define the waveguide three dimensional mode as $\mathbf{e}_{wg} = \tilde{\mathbf{e}}_{wg}(x, y)\exp(-j\beta z)$ where $\tilde{\mathbf{e}}_{wg}$ is the two dimensional waveguide mode. Eq. 3.11 shows that the high absolute value of $\Delta\epsilon$ for a metallic perturbation increases the polarization current and hence gives rise to higher coupling compared to a dielectric perturbation.

3.1.3 Design and Simulation

Vertical coupler designs in this paper are based on rectangular apertures in an antenna plane placed above a Si_3N_4 waveguide, with an additional metallic ground-plane under that waveguide to facilitate

vertical coupling (Fig. 3.1). As an example realistic structure, we chose the following: (1) an 80nm Al ground-plane, (2) a 60nm Al antenna layer, (3) a Si_3N_4 waveguide with a width of 700nm and a 220nm height, (4) a ground plane to antenna separation of 680nm, and (5) a waveguide to antenna separation of 100nm (Fig. 3.1(a)). The permittivities of Si_3N_4 and SiO_2, are 4, and 2.1 respectively at 1550nm (63), and the Al Drude parameters are $\gamma_d = 2.4\times10^{14}$ rad/sec and $\omega_p = 2.2\times10^{16}$ rad/sec as measured in our collaborator fab in Sandia national labs.

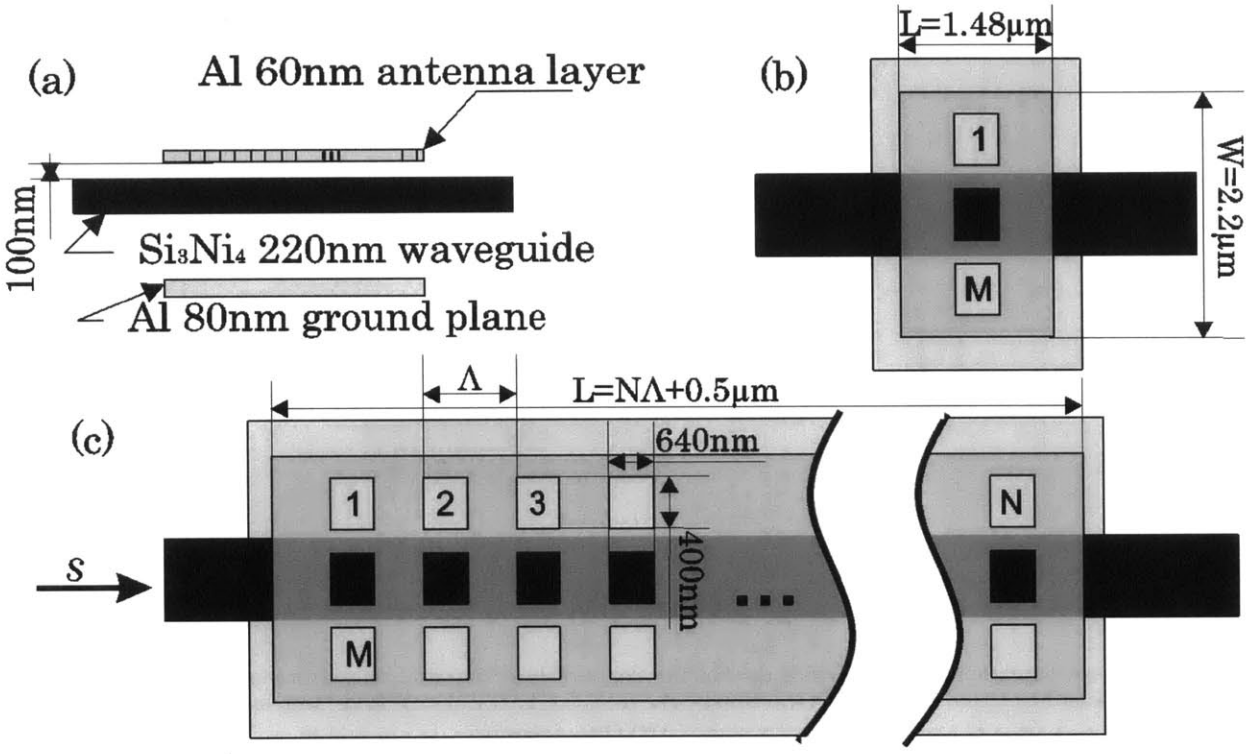

Fig. 3.1 Antenna designs: (a) side view, (b) top view of laterally repeating apertures and (c) longitudinally repeating with period $\Lambda = 0.9\mu m < \lambda/n$. The underlayer of Al represents a ground plane positioned at $d = 3\lambda/4n$ (680nm) from the emitter metal.

In order to calculate τ_e and τ_r, we look at the ring-down properties of the resonator. When no input excitation is applied ($s = 0$) the solution for Eq. 3.1 is the exponential ring-down in this case

$$a(t) = a(0)\exp\left(j\omega_0 t - \frac{t}{\tau}\right). \qquad \text{Eq. 3.12}$$

3D finite-difference time-domain (FDTD) ring-down simulations, of just the antenna in Fig. 3.1 (without the Si_3N_4 waveguide), give us the radiation rate τ_r of the antenna. Fig. 3.2 shows the ring-down of a single rectangular aperture resonator, tuned to a resonance near 1550nm, when it is isolated and also when coupled to a waveguide. The resulting τ_r (neglecting ohmic losses) is found to be ~7fs when no waveguide is present. The combined time constant for radiation plus waveguide coupling, τ, is found to be about 5.8fs. Using (2), the external coupling coefficient is found to be $\tau_e \approx$ 34fs, five times larger than the radiation coupling τ_r. Although the result above is approximate, as τ_r can vary with the introduction

of the waveguide, the fact that τ_e is much greater than τ_r indicates that the resonator is clearly under-coupled.

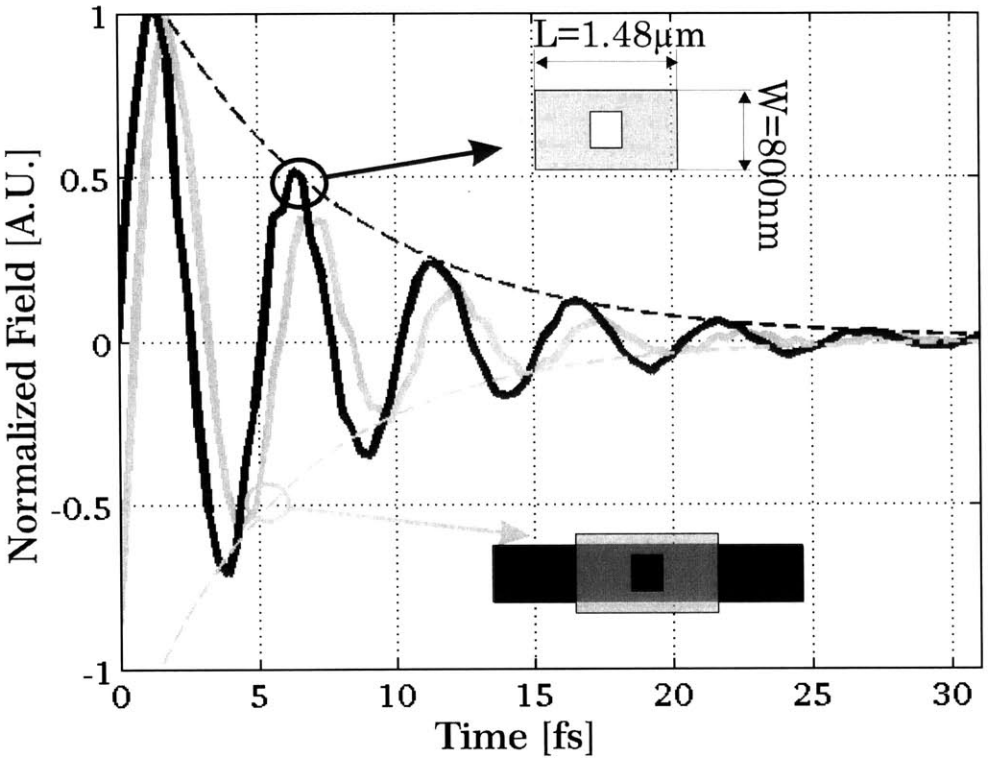

Fig. 3.2 Ring-down simulations: 3D FDTD ring-down of the electric field (and its exponential envelope) for a single aperture resonator without (black) and with (gray) a waveguide. The fields (i.e. lateral electric fields) were taken from the aperture center.

To increase the coupling to the resonator, one can, for example, lower the metal level to bring the antenna closer to the feeding waveguide or reshape the antenna's input side (e.g., using a metal-insulator-metal feeder to the aperture). Our approach was to coherently repeat the antenna aperture and, by doing so, increase the waveguide to resonator coupling coefficient μ as shown in Fig. 3.1(b).

From Eq. 3.11, it becomes clear that repeating the antenna structure laterally will increase the integral by the adding volume with non-zero $\Delta\epsilon$. Taking into account the normalization of the new $\mathbf{e}_r$ mode, that takes more volume now, reduces the effect by a factor of the square root of the volume ratio. This leaves us with a residual increasing of μ that is approximately the square root of the repetition number M, reduced slightly by the weaker field at the waveguide edge. Conversely, the radiation efficiency of the bound surface plasmon does not appreciably change, a result of the scattering rate remaining constant when the number of apertures is increased without altering the density of apertures. Therefore, by repeating the structure laterally M times in a region where the waveguide modal field remains strong, we can increase τ_r / τ_e by a factor of approximately $\sqrt{M}$. As a result, by placing apertures laterally, the

antenna inches closer to critical coupling (i.e. $\tau_e = \tau_r$). A comparison of 3D FDTD simulations for one and three apertures is depicted in Fig. 3.3(a). The emission of the three-aperture emitter is shown to exceed the one aperture emitter by ~1.6 which is close to the $\sqrt{3}$ ratio predicted by coupled mode theory. Still, as mentioned in Section 3.1.2, since we excite the resonator from only one direction in the waveguide, and considering that μ and τ_e are given for coupling to both directions, the maximum possible emission is 50% in a longitudinal symmetric case. Higher efficiencies require non symmetric excitations or non-symmetric emitters, a result that is explained both in Section 2.4 and at the end of Sections 3.1.2.

In order to obtain the results in Fig. 3.3(a), we monitored the spectral content of the fields over the surface of a box enclosing the structure. From this, we calculated the amount of energy leaving each facet (Fig. 3.3(b)). All other losses, including emission out of the sides, bottom and rear of the structure had significantly lower values (ohmic losses are ~10% for the 3x6 (WxL) antenna over most of the band and less for the smaller structures). In all cases depicted in Fig. 3.3(a), the structure includes a ground plane at a distance of $d \approx 3\lambda/4n$ for constructive vertical coupling. This was done to, constructively, interfere the reflection of the bottom emission with the top emission and, thus, maximize the vertical coupling.

To further enhance the emission, the structure is repeated longitudinally in order to help couple the remaining field in the waveguide (see Fig. 3.1(c) and 3rd to 5th curves in Fig. 3.3(a)). In this case, we can achieve greater than 50% coupling by breaking the symmetry of the problem and directing the emission to an angle from the surface normal which is half the way from the main lobe maximum to the first zero. This can be done by tuning the structure longitudinal period Λ to be slightly less than the bound resonant wavelength (0.9μm instead of 1μm). Curves 3 and 4 in Fig. 3.3(a) show the different between direct up emission and slightly backward emission in the 3x2 apertures case. The 5th curve shows 65% coupling using 3x6 apertures structure. Finally, looking at the far field pattern of the top facet emission (e.g. Fig. 3.3(c) for the 3x6 apertures case) shows that the main lobes in all structures has a 15° to 25° FWHM. The main lobe was centered at the zenith for the first 3 structures and at 10° and 5° back from the surface normal for the fourth and fifth structures respectively.

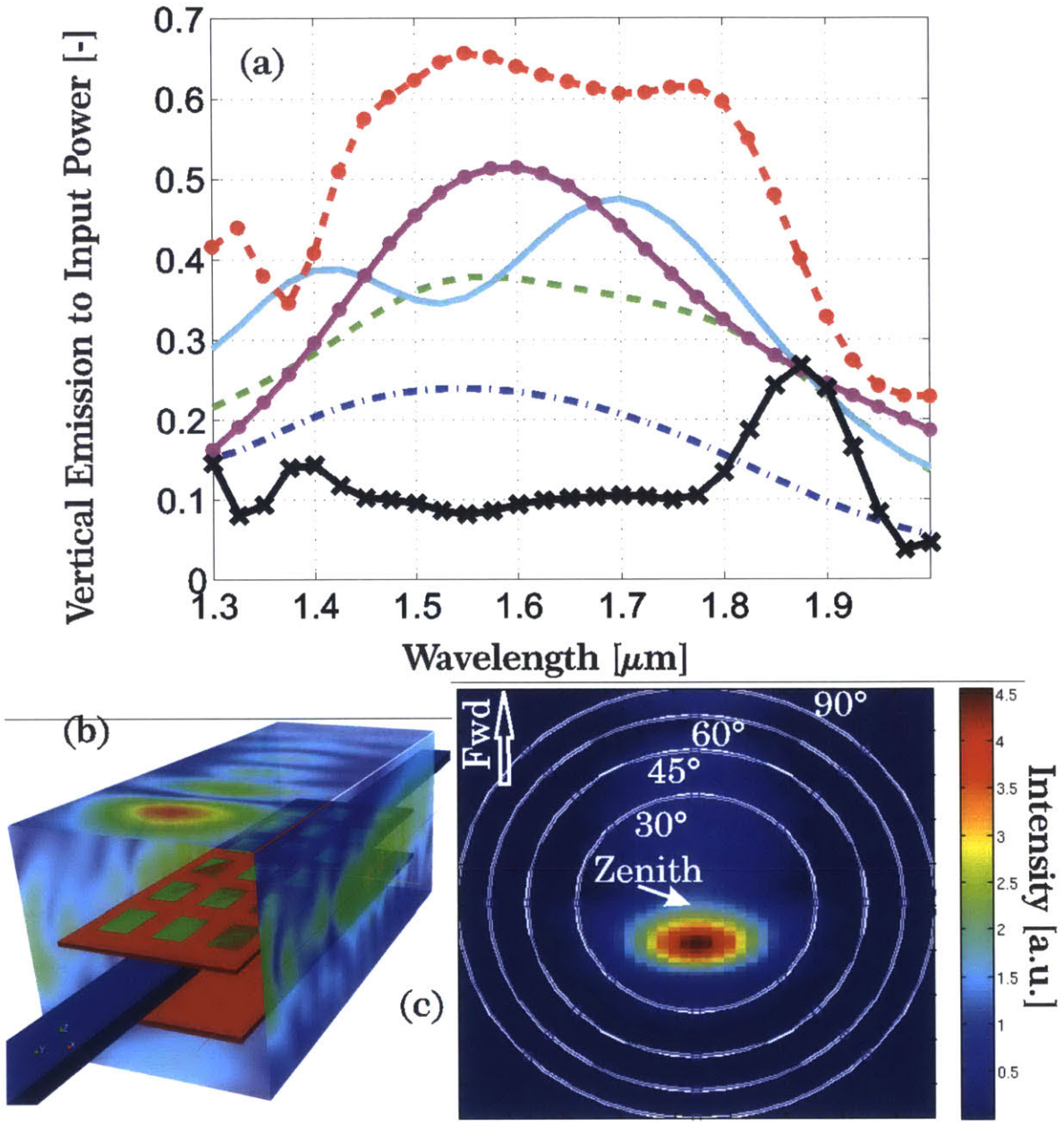

Fig. 3.3 Emission simulations: (a) Simulated vertical emission for different structures with ground-plane: blue dash-doted single aperture, dashed green 3 apertures arranged laterally to the waveguide direction, solid cyan 3x2 array design to emit exactly to zenith, magenta solid with dots 3x2 array design for 10° backward emission, dashed red line with dots 3x6 array design for 5° backward emission and black line with Xs ohmic losses of 3x6 array, (b) the simulated 3x6 structure with the time integrated field box around it. (c) Far field pattern of the same structure at λ=1550nm.

3.1.4 Fabrication

Three nanoemitters of the proposed scheme (1x1, 1x3 and 3x3 apertures) have been fabricated at Sandia National Laboratories. 75nm AlCu was deposited above 3μm of oxide and ground planes were defined using photolithography. Another layer of oxide was grown and Chemical Mechanical Polished (CMP) to 400nm above top of ground plane. 250nm of Si_3N_4 was, then, PCVD grown on top of the oxide

and the waveguides were defined using photolithography. Last layer of SiO_2 was deposited and CMP was done to 200nm above top of waveguide. Finally, the antenna layer of 50nm AlCu was placed; antennas' perimeters were defined using photolithography, and apertures were defined using e-beam lithography.

Due to fabrication constrains, some thicknesses were fabricated not according to best simulated values:

- The waveguide thickness was fabricated to be 250nm instead of 220nm as simulated, a difference that bounds the mode stronger in to the waveguide and reduce coupling,
- antenna-to-waveguide separation was fabricated to be 200nm instead of 100nm, which also reduced coupling and,
- antenna-to-ground plane spacing was fabricated 850nm instead of 780nm, which broke the $3/4\lambda$ condition mentioned above.

Moreover, since fabrication process started before ending simulation optimization, in plane dimensions of both ground plane and antenna plane were randomly define. Table 3.1 shows the in plane fabricated dimensions for each structure with the single emitter optimized dimensions as described in Section 3.1.2 and simulated in Fig. 3.3 above. Fig. 3.4(a), (b) and (c) shows Scanning Electron Microscope (SEM) images of the 1x1, 1x3 and 3x3 apertures antennas respectively. Lastly, the chips were fabricated with no trench etch at end of waveguides, and dicing roughness made fiber-to-chip coupling loss vary between different ports. This, in turn, made estimation of power-in-waveguide less precise.

dimensions		1x1 aperture antenna		1x3 apertures antenna	3x3 apertures antenna
		Optimal	Fabricated	Fabricated	Fabricated
Ground-plane	L	1.42μm	4μm	5μm	6μm
	W	2.88μm	4μm	4μm	4μm
Antenna external	L	1.42μm	2μm	3μm	4μm
	W	0.8μm	2μm	2μm	2μm
Antenna Aperture	L	380nm	400nm	380nm	400nm
	W	400nm	320nm	400nm	320nm

Table 3.1 Main antenna fabrication dimensions and optimal single aperture dimension as simulated above in Section 3.1.3 and Fig. 3.3.

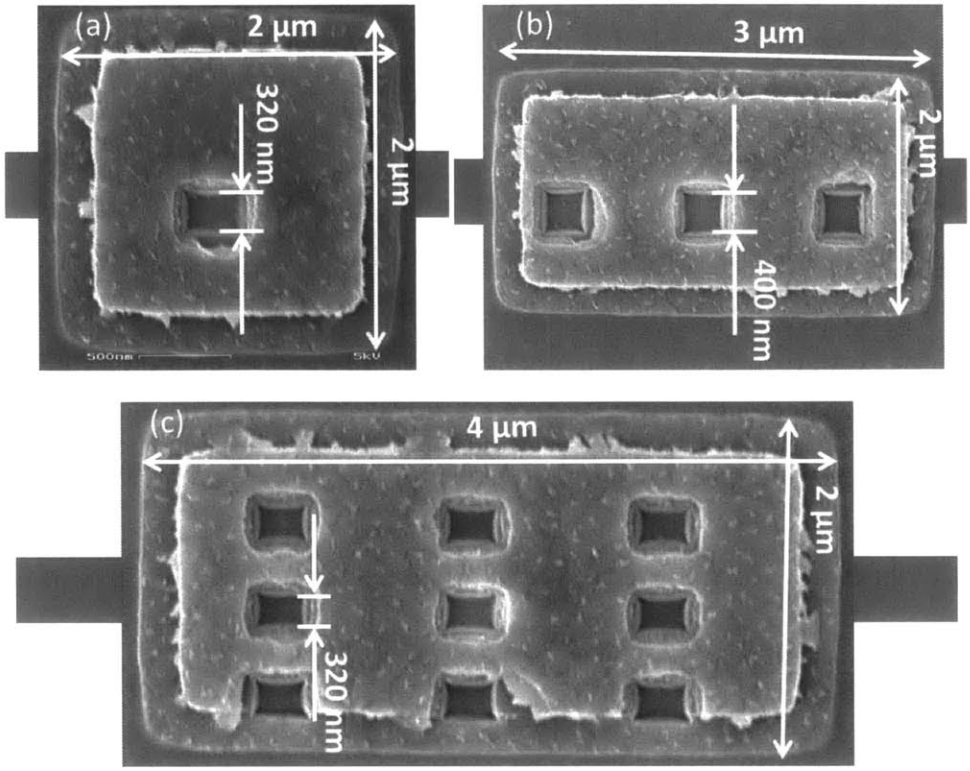

Fig. 3.4 Antenna SEM: Images of a (a) 1x1, (b) 1x3 and (c) 3x3 apertures antennas. Selected dimensions and illustration of waveguide orientation under the antenna are given. Residual photoresist can be seen on all structures. This resist may have played a role in changing the antenna properties a little bit.

Although this fabrication did not use the optimal structural dimensions and hence high efficient antenna result were not expected, we can still treat it as validation step for our theoretical results. This validation is done by testing both antenna efficiencies and far field patterns, and comparing antennas' characteristics to simulated results of structures with similar dimensions.

3.1.5 Experimental Results

The three fabricated devices were tested for their upward emission efficiency where efficiency is defined here as power collected by the test system's objective divided by the in waveguide calculated power. A tunable laser source was coupled to the chip using lensed fibers; coupling losses were measured on a straight, no antenna, waveguide and subtracted from the fiber input power. A free-space detector, together with a 0.68 numerical aperture (NA) lens was used to collect the light emitted upwards where IR and visible cameras were used to monitor the fiber position. Then, after a good coupling achieved, the IR camera was used to focus and position the free space power emitter to collect antenna output radiation. Fig. 3.5 shows this experimental set and Fig. 3.6(a) shows measured emitter efficiency vs wavelength.

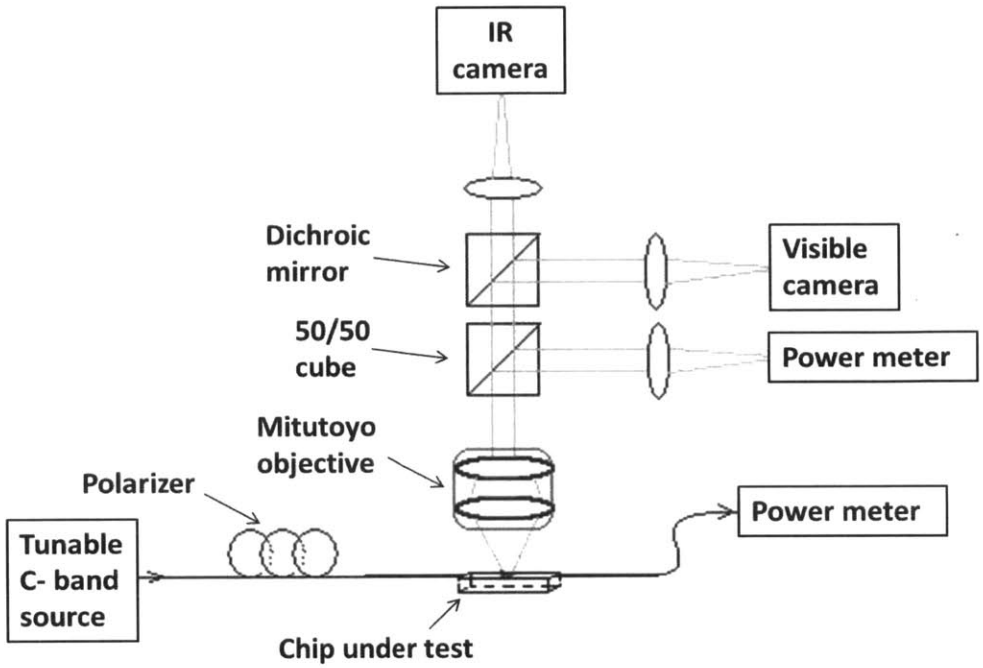

Fig. 3.5 Experimental system: The system used for power and efficiency measurements. A tunable fiber coupled laser with a polarization controller fed the chip, optical system with a 0.68 NA objective assembled was used to align fibers and measure free space output power and another fiber coupled power meter measured the residual power in the waveguide.

All structures have been simulated as fabricated. Non optimal antenna dimensions described above resulted in each device having several radiation lobes, sometimes exceeding the experimental system's NA. Capturing such emission requires a significantly higher NA lens than the 0.68 (±43°) used for these measurements. Simulated results suggest that the fraction of the light captured by the imaging lens is 20%, 14%, and 60% for 1x1, 1x3 and 3x3 structures respectively. The limited numerical aperture of the collective optics, therefore, was taken in to account in the calculated efficiencies. The final efficiencies of as-fabricated devices are shown in Fig. 3.6(b). It can be seen from these graphs that the main different between fabricated and simulated efficiencies are merely a constant number for each antenna structure. We attribute this difference to the fiber-to-waveguide coupling. As mentioned above, due to the lack of fiber trenches and chip edge roughness, uniform coupling between different waveguide ports was poor. Overall measured efficiencies at 1550nm for vertical nano-emitters presented in this paper are 4.93%, 7.11% and 13.04% for 1x1, 1x3 and 3x3 apertures emitter structures respectively. These numbers are not high but support our simulation results; with the right, optimal, dimensions, coupling can reach between 24% for single aperture and 65% for 3x6 apertures antennas.

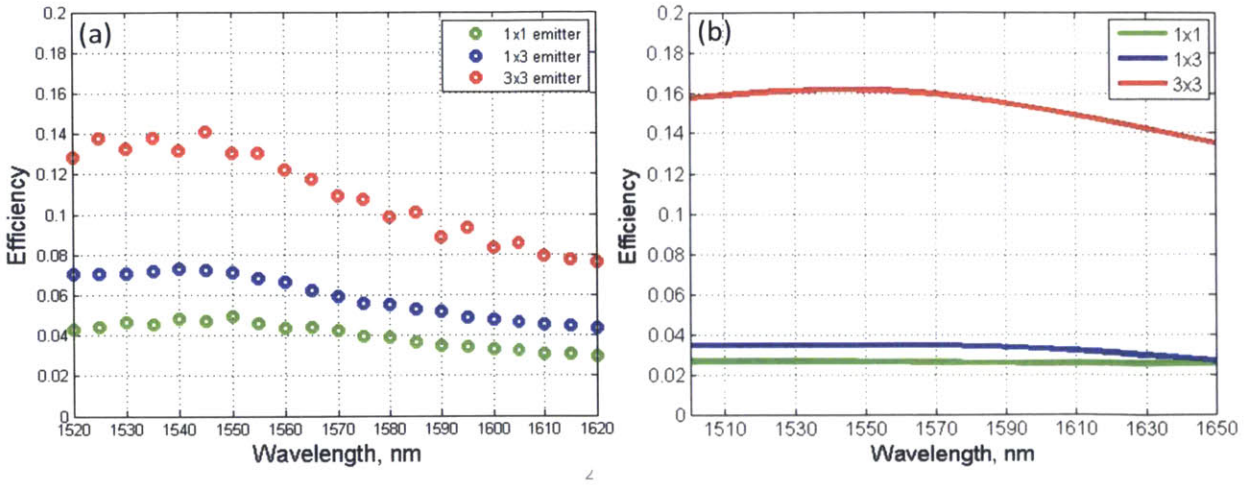

Fig. 3.6 Emission powers: (a) Experimental efficiencies and (b) re-simulated efficiencies for as-fabricated antenna dimensions for 1x1, 1x3 and 3x3 apertures antennas.

In order to further verify our simulations to fit fabricated antenna's behavior, we looked at the far field images of each antenna and compared it with the simulated far field images of the corresponding structure. The same imaging system describe above and shown in Fig. 3.5 with the same 0.68NA objective and small changes in lens positioning was used to image the far field of each antenna. In order to verify that the received image is a far field image, changes in the appearance were searched for while slightly moving the imaging system in all three axes. When no changes observed, the image was the far field one. Fig. 3.7 shows experimental (a-c) and simulated (d-f) far field images of all 3 structures (1x1, 1x3 and 3x3 respectively). It can be seen that the simulated and experimental far field images agree to a good extent which again help validates our FDTD simulation rigorousness and confirm our 65% efficiency result for the 3x6 antenna above.

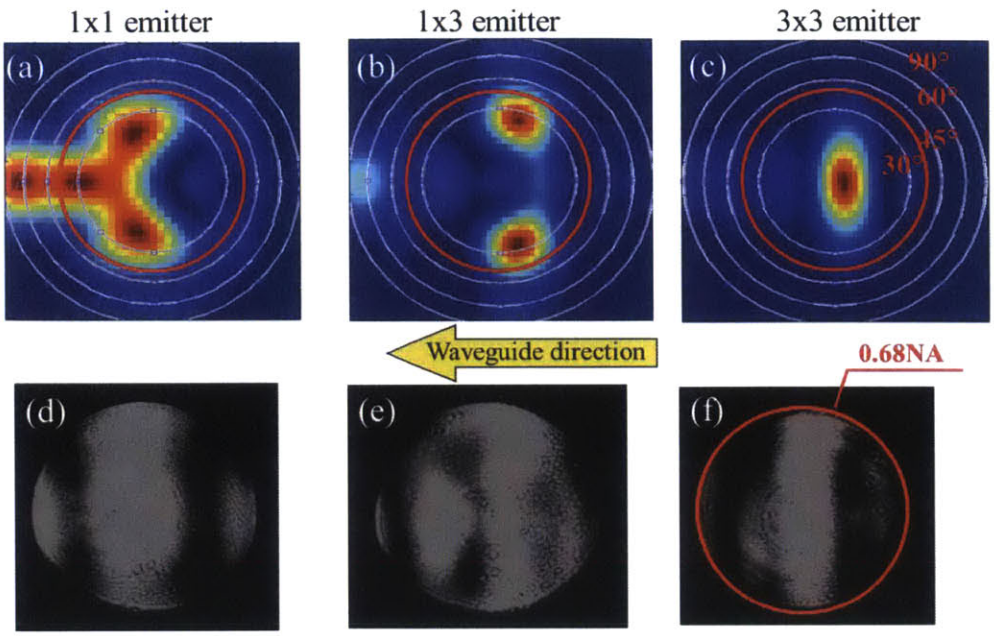

Fig. 3.7 Fer field patterns: (a-c) Re-simulated far field emissions of the 1x1, 1x3 and 3x3 apertures antennas respectively, (d-f) IR images of the far field emission pattern of these antennas showing good agreement with re-simulated images. Red circle represents the collection objective's NA.

3.1.6 Conclusion

Using three-dimensional FDTD simulations, we show that metallic nano-antenna structures can easily vertically couple 65% of an input bound wave with a structure of only four free-space wavelengths long. Comparison between fabricated antennas' emission and simulated results verify our FDTD simulation method to match experimental results, and therefore support the high coupling efficiency simulated with the proposed structure. This structure is short, realistic and uses commonly available materials. While compact, all-dielectric silicon emitters have been demonstrated (59), to our knowledge this is the first proposed and numerically verified compact emitter design in a Si_3N_4 waveguide, which is a relatively low index contrast system. By repeating the structure laterally and then longitudinally with a period Λ, which is slightly shorter than the effective wavelength, highly efficient and extremely broadband emission is produced. While the initial measured efficiencies were not yet as high as grating-based emitters, the potential for extremely compact and wide-band operation offered by nano-antenna-based emitters is compelling. We expect that in a silicon waveguide coupled to a nano-photonic antenna even greater efficiency would be possible due to the increased polarization current enabled by the high index contrast of a silicon waveguide.

3.2 Resonance-Chirped Sub-Wavelength Nanoantennas

Herein we propose, theoretically investigate, and numerically demonstrate the first use of frequency chirping to achieve broadband, efficient sub-wavelength vertical emission from a dielectric waveguide. We demonstrate this unique and effective approach in the telecom C-band in a nanophotonic frequency chirped dipole antenna. The structure utilizes a plasmonic antenna placed above a Si_3N_4 waveguide, and a ground plane, to enhance emission efficiency. Three-dimensional Finite-Difference Time-Domain (FDTD) simulations reveal up to 55% vertical emission efficiency and a bandwidth of 500nm is possible in a structure less than half a wavelength long. The design methodology and theoretical underpinnings of frequency chirped nanophotonic antennas coupled to dielectric waveguides are presented. This chapter follows our publication described in (64).

3.2.1 Introduction

Vertical coupling can be used in Silicon On Insulator (SOI) based Nanophotonic Phased Arrays (NPA) for the purpose of emitting light traveling in a waveguide to a free space mode (23), (24), (65). Vertical input/output coupling has previously been extensively investigated for the purpose of coupling to or from an optical fiber (56), (57), (58), (59), (66), but, as a result, most vertical couplers to date have emission patterns matched to fiber modal diameters (~10μm) and size of the same order or larger. In a NPA, however, the desired emitter characteristics include strong waveguide-to-free-space output coupling in a compact structure – ideally less than one wavelength long. A short emitter length is critical to fitting many emitters in a small area and to enabling wide divergence angles within a single lobe. However, demonstrations of efficient output coupling using short structures are uncommon; minimum structure lengths found to be several wavelengths long (54), (57), (59). Short emitters, for coupling between two modes in general and vertical coupling in particular, have also been demonstrated using nanoantennas designs translated from the radio frequency (RF) to optical bands (41), (52), (53), (59). Howerver, traditional RF antennas differ from photonic nanoantennas in at least one important way: RF antennas are fed from thin (much narrower than one wavelength) transmission lines, enabling the excitation of the antenna to occur from a single location or by a single component, usually called the radiator. In a photonic nanoantenna, the open dielectric waveguide precludes separation of the guided wave from the antenna structure and the guided wave interacts with the entire antenna. Thus, passive elements like the directors or reflector in a Yagi-Uda antenna can no longer count as passive. This fundamental difference suggests that a different tact should be taken to enable compact and efficient emission from antennas coupled to dielectric nanophotonic waveguides. In (53), the authors by-pass this problem by polarization separation and tilting the feeding element. However, this method introduces a 50% coupling penalty into

the antenna. This paper uses a different approach which considers both the input and output waves in order to design a new antenna structure that couples more efficiently between them.

We propose and numerically demonstrate the use of deep sub-wavelength frequency chirped elements to enable sub-wavelength emission from a nanophotonic dielectric waveguide. Finite-Difference Time-Domain (FDTD) simulations of a one-layer antenna plus a ground plane show 55% up emission with a structure only one third of a free space wavelength long. The antenna is a cluster of metallic nano-rods designed to work in the C-band, however, the results here are general and can be applied to any chirped structure and any band of the electromagnetic spectrum to achieve efficient, sub-wavelength coupling between two propagating modes.

3.2.2 Theory

To gain intuition about the coupling between the nanoantenna and the waveguide, we treat the nanoantenna as a resonator and use coupled-mode theory in the time domain (29), (61), (62). Coupled-mode theory assumes shape invariance of the modes and drops second order terms, enabling quantitatively accurate results only with weakly coupled modes; however it provides useful qualitative insight even when modes are strongly coupled. To ensure accuracy in design, we rely on three-dimensional full field simulations for all quantitative results in this letter.

The differential equation governing the reaction of a resonator with energy amplitude a and coupling coefficient μ to a perturbing mechanism (e.g. a waveguide) with field amplitude s is, to first order (61)

$$\frac{da}{dt} = \left(j\omega_0 - \frac{1}{\tau}\right)a - j\mu s \qquad \text{Eq. 3.13}$$

where ω_0 is the resonance frequency, and τ is its field decay rate. In a nanophotonic antenna, the loss mechanisms can be broken down into radiation, ohmic, and coupling losses, with decay rates τ_r, τ_o, and τ_e respectively. This equation is similar to Eq. 3.1, just with re defining μ as $j\mu$ from the last section. The steady state solution to Eq. 3.13 with input s at frequency ω is:

$$a = -\frac{j\mu s}{j(\omega - \omega_0) + \frac{1}{\tau}} \equiv sRe^{j\Delta\varphi}, \qquad \text{Eq. 3.14}$$

where we define the resonator response to have amplitude R and phase $\Delta\varphi$. It is easy to see that, for $\omega \gg 1/\tau$, one can change the phase response of the resonator, $\Delta\varphi$, through a total range of π radians by changing the resonance frequency. When μ is real and positive, for example, $\Delta\varphi$ will vary in the range $(-\pi,0)$, depending on the value of ω_0. If the resonator mode is leaky (radiating), the phase of the emitted field will be the same as that of the resonator.

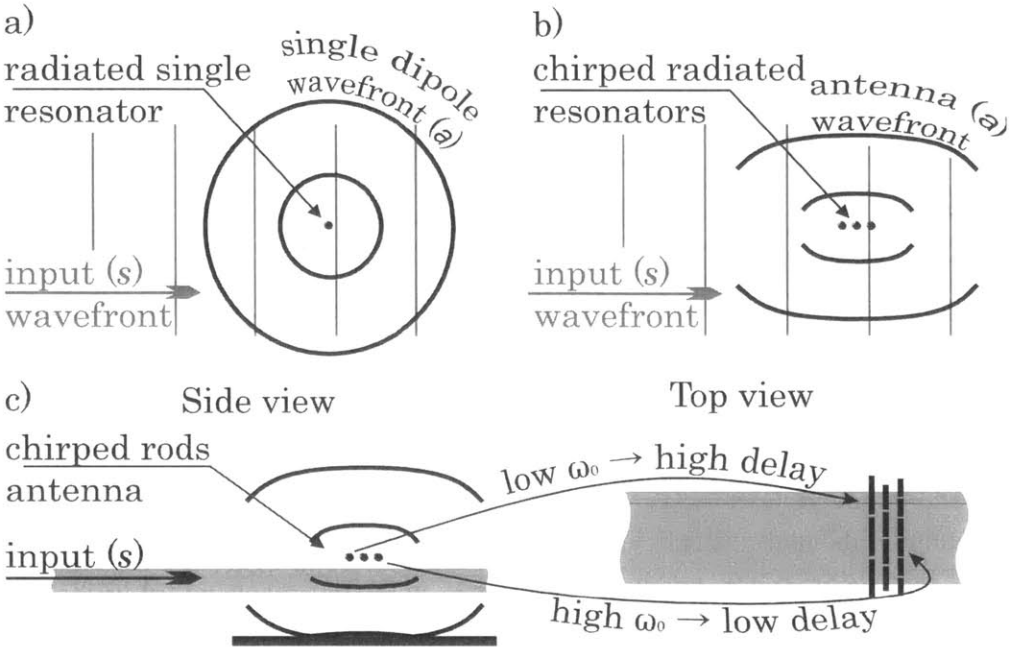

Fig. 3.8 Antenna design principle: (a) side view of a single resonator (here a dipole) driven by a plane wavefront, (b) a set of chirped resonance resonators design for right-angle wave coupling driven with the same source as (a), (c) Side and top view of a set of resonators designed for vertical coupling from a waveguide to free space. Total structure length is smaller than $\lambda/2n_{eff}$.

Using this principle, and the space dependence of the input wave, $\exp(-j\vec{k}z)$, we can place several resonators with different resonances along the waveguide in such a way that, although placed in different z positions, they all resonate with the same phase. Thus, the resonators will constructively interfere to form a vertically emitted wave. As Fig. 3.8(a) shows, a single dipole driven by a plane wave emits in all directions. However, a set of frequency chirped dipoles can be combined to interfere and form a flatter wavefront and larger antenna gain as shown in Fig. 3.8(b), enabling efficient vertical coupling. By additionally repeating the dipoles laterally we further enhance the coupling at each longitudinal position. The resulting antenna structure is illustrated in Fig. 3.8(c).

Considering cross-talk between the different components of the antenna, we can rewrite Eq. 3.13 for a group of resonators a_i

$$\frac{da_i}{dt} = \left(j\omega_i - \frac{1}{\tau_i}\right) a_i - j \sum_k \mu_{ik} a_k \,, \qquad \text{Eq. 3.15}$$

where ω_i and τ_i are the i^{th} resonator natural resonance and decay rate respectively, and μ_{ik} is the coupling coefficient from the k^{th} to the i^{th} resonator. It can be seen from Eq. 3.15, that, when all the resonators have same phase, no amplitude fluctuations are produced; there is only a red shift in the resonant frequency. This Red shift can easily corrected by readjusting and blue shifting the individual resonance of each element, ω_0.

3.2.3 Design and Simulation

In this paper, we use dipole rod resonators, with a dimension along the input $\vec{k}$ vector much shorter than a wavelength. We arrange several of these dipoles in a half wavelength section (π phase region) to create a sub-wavelength coupler through constructive interference of the output from each rod. Fig. 3.8(c) illustrates the principle behind the structure of the vertical coupler. The specific vertical coupler designs presented here are based on phase chirped rod resonators placed in a plane above a Si_3N_4 waveguide. An additional metallic ground-plane is placed under that waveguide to facilitate vertical coupling (see Fig. 3.8(c)). For an example structure, we chose the following: (1) an 80nm Al ground-plane, (2) a 60nm Al antenna layer, (3) a Si_3N_4 waveguide with a width of 700nm and a 220nm height, (4) a ground plane to antenna separation of 680nm, and (5) a waveguide to antenna separation of 100nm. The permittivities of Si_3N_4 and SiO_2, are 4, and 2.1 respectively at 1550nm (63). The Drude parameters used for Aluminum were $\gamma_d = 2.4 \times 10^{14}$ rad/sec and $\omega_p = 2.2 \times 10^{16}$ rad/sec.

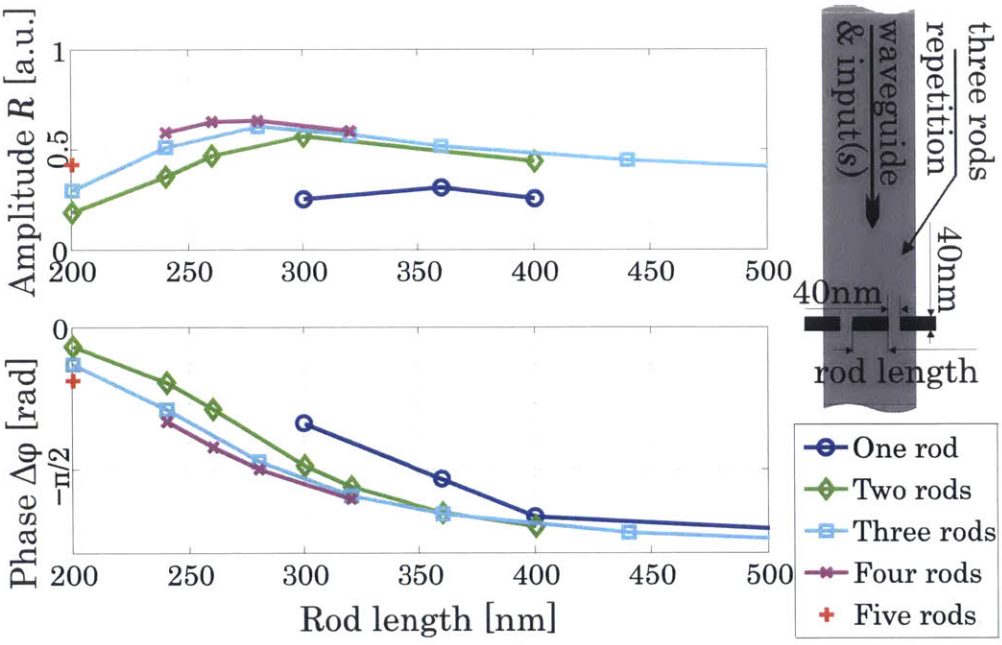

Fig. 3.9 Design method: Amplitude R (top) and phase Δφ (bottom) of the resonator response vs. rod length for lateral repetition of specified number of rods and wavelength of 1550nm (a three rod lateral repetition example is shown on the right).

To design the antenna, first, the phase responses of dipole antennas of different lengths are examined. The responses are calculated via 3D FDTD simulations using a waveguide with no ground plane as the feeding mechanism. The one rod curve (blue) in Fig. 3.9 shows the resulting amplitude and phase responses at a wavelength of 1550nm as a function of rod length. Using Eq. 3.14 and the asymptotic value of the phase response for the lowest resonance (about -2.5radians), we calculate τ to be ~1fs. With such a short decay intrinsic to a nano-rod, each nano-rod is inherently undercoupled. Thus, following

Sections 3.1.2 and 3.1.3, lateral repetition of the nano-rods is needed to enhance overall coupling. Various sets of laterally repeated rods (same length in each set) were examined to determine their phase responses. Fig. 3.9 shows the resulting responses (amplitude and phase) as a function of rod length and repetition number. It can be seen that the maximum amplitude response always corresponds to the $-\pi/2$ phase response, as expected from Eq. 3.14.

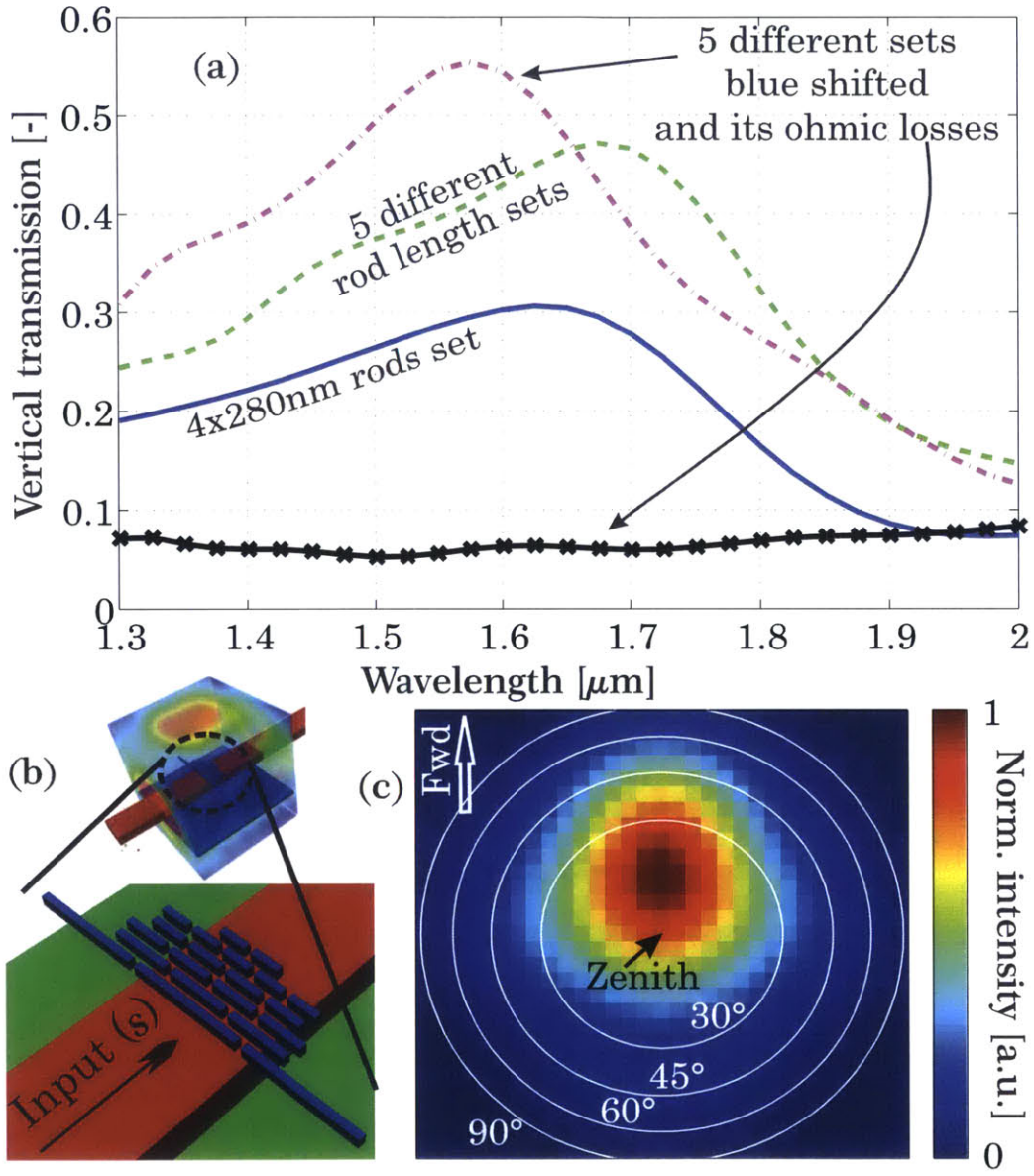

Fig. 3.10 Simulated results: (a) Simulated vertical emission for different structures, each with a ground-plane: solid blue four times lateral repetition of 280nm rods, dashed green five different sets of rods arranged to create the phase chirped antenna, dash-doted magenta same structure blue shifted and black line with x's ohmic losses of the later, (b) final structure with the time integrated field box around it. (c) Free space far field pattern of the same structure at λ=1550nm.

Next, we choose resonators with different phase responses and place them along the waveguide axis such that the sum of the input wave phase $\vec{k}z$ and the specific phase response is same for all resonators.

This results in constructive interference in the designed output direction. Lastly, a correction to the rod length is made in order to correct for the red shift caused by the proximity of different resonators with the same phase.

Fig. 3.10(a) compares the up emission of one 4 rod set on resonance (blue solid line) with the uncorrected (green dashed line) and redshift corrected (magenta dash dotted line) phase chirped antennas described above. The rods in the uncorrected structure are arranged in sets 3x680nm, 3x360nm, 4x280nm, 4x240nm and 5x200nm where AxBnm stands for (repetition number)x(rod length in nm) and the order of writing is the order along the z axis. The corrected (blue shifted) antenna has rods arranged in sets 3x630nm, 3x320nm, 4x240nm, 4x200nm, 5x160nm and an extra 2x160nm set. The solid black line, show the ohmic losses to be under 10%. In order to obtain the results in Fig. 3.10(a), we monitored the spectral content of the fields over the surface of a box enclosing the structure. From this, we calculated the amount of energy leaving each facet (Fig. 3.10(b)). All other losses, including emission out through the sides, bottom and rear of the box had significantly lower values (<10% each at 1550nm). All cases depicted in Fig. 3.10 include a ground plane at a distance of $d \sim 3\lambda/4n$ for constructive vertical coupling. This was done so as to combine the bottom and top emission and maximize the vertical coupling. In total, we found 55% vertical emission, revealing efficient emission from a sub-wavelength structure. Additionally, as shown in Fig. 3.10(c), the main lobe from the full structure has less than a 30 degree FWHM and therefore the output can be directed. Lastly, the resulting bandwidth of a short (rapidly coupled) emitter goes up to ~500nm.

3.2.4 Conclusion

In conclusion, by using 3D FDTD simulations, we show that metallic nanoantenna structures can vertically emit at least 55% of an input wave over a 3dB bandwidth of 500nm in a structure only one third of a free-space wavelength long. Furthermore, the proposed structure uses realistic dimensions and commonly available materials. By repeating the structure longitudinally, even more efficient emission could be produced. While efficient all dielectric emitters have been demonstrated (23), (24), (56), (57), (59), to our knowledge this is the first proposed and numerically verified compact (less than a wavelength long) emitter design and the first proposed structure of its kind.

4 2D Electrical Steering Phased Array

Optical phased arrays have several large advantages over their RF equivalents. The much shorter optical wavelength holds promise for large-scale integration (67). The short wavelength allow for much smaller apertures flowing with much smaller systems and the computability of guiding the light in materials from the electric industry, opens the way for low cost mass production of Nanophotonic Phased Array (NPA). Still, the intense requirements of optical phased arrays also impose severe challenges. Consequently, optical phased arrays, using various platforms (68), (69), (70), (71), (72) and recently with chip scale nanophotonics (23), (24), (28), (73), have so far been restricted to one-dimensional electrical steering. Here we report the demonstration of a two-dimensional steerable NPA, in which 8x8 (total 64) optical nanoantennas are densely integrated on a silicon chip with a pitch of 9μm in each dimension. We show that active phase tunability can be realized demonstrating dynamic beam steering and shaping. This work demonstrates a 2D NPAs implemented on compact and inexpensive nanophotonic chips built with complementary metal-oxide–semiconductor (CMOS) technology. This, in turn, enables arbitrary radiation pattern generation using NPAs and, therefore, extends the functionalities of phased arrays beyond conventional beam steering. In fact, it opens up new possibilities and wide use in applications such as communication, ranging, three-dimensional holography and biomedical sciences. This chapter describes a work done in collaboration with Jie Sun et al and published in (6)

4.1 Introduction

A NPA, consists of several, typically identical, optical antennas. Each antenna emits light of a specific amplitude and phase to form a desired far-field radiation pattern through interference of these emissions. The short wavelength of light offers potential for NPAs to greatly exceed the number of elements found in their radiofrequency counterparts in a compact, low-cost chip. By incorporating a large number of antennas, high-resolution far-field patterns can be achieved and arbitrary radiation patterns can be generated by the NPA (6), extending the functionalities of phased arrays well beyond the conventional beam focusing and steering. However, the short optical wavelength also presents challenges in realizing coherent outputs from such large-scale NPAs. Specifically, even nanometer scale fluctuations in fabrication processes may affect the antennas' optical emission that need to be balanced in power and aligned in phase to form a specific far-field radiation pattern. As a consequence, all chip-based two-dimensional NPAs demonstrated so far are limited to small-scale implementations with no more than 16 antennas, and their functionalities are thereby constrained to conventional single beam steering. Here we propose a compact, scalable architecture, NPA system that is compatible with a CMOS process and

demonstrate that active phase tunability can be successfully up scaled in antenna number and generate dynamic far-field patterns.

4.2 Theory and Design

In order to support a 2D electrical steering in a scalable system, we use the architecture shown in Fig. 4.1. First, we locate all essential components of the NPA in a 2 dimensional small unit cell including the coupler to the unit cell, the phase shifter and the antenna itself. Then, we distribute the energy between the different unit cells in a scalable manner. A laser input is coupled into the main silicon bus; this bus waveguide distributes energy by evanescently coupling to row-buses and each row-bus distributes the energy, using a different evanescent field coupler design, between the different unit cells of the specific row. The coupling to the row waveguides and to each unit cell is controlled in such a way that each obtains the wanted amount of power (flat power distribution in our case). By doing so, we gain two main advantages. First, the distribution of power in two stages releases the need to couple a very small fraction of the light to the early antennas on the bus. Coupling such a small fraction is theoretically possible, but much more sensitive to fabrication imprecisions. Distribution in two stages (rows/columns) releases these tight tolerances a bit. Second, and more importantly, this two-dimensional architecture allows the phase array to be easily up scaled in both dimensions while maintaining 2D electrical phase control and by adjusting only the coupling strength of the unit cell or bus coupler. Each of the optical antenna unit cells (as seen in the green rectangle in Fig. 4.1) consists of three major functional parts: a coupler to distribute the light from the row bus to the antenna, a phase shifter and a nanoantenna to efficiently deliver optical power to free space. The coupler and phase shifter components in the unit cell are described in detail in Chapter 1. Here we will briefly describe the phase shifter and expand more on the specific antenna design and differences in the couplers' design.

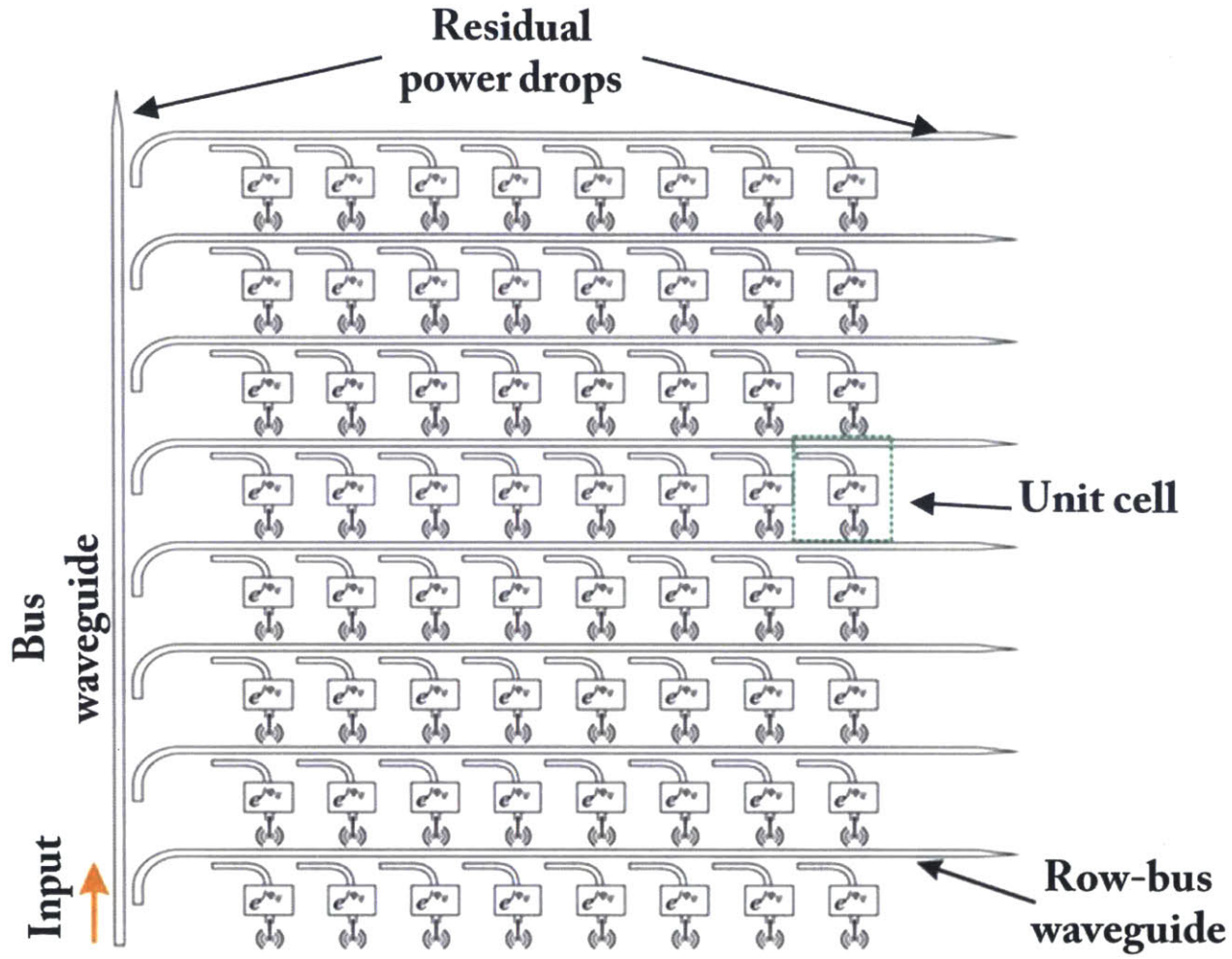

Fig. 4.1 Architecture of a scalable 2D electrical steering NPA: The main bus waveguide, row-bus waveguide and array's unit cell in the green rectangle are shown. At the end of each bus waveguide there is a taper to dispose unused optical power.

Couplers Design: Directional, evanescent field, couplers in this work were based on the same architecture as described in Section 2.2. Nevertheless, the small design differences from the coupler described in Section 2.2 and the need to take into account the phase effect of the coupler are explained here. The blue line in Fig. 4.2(a) shows the coupling required per unit cell number counting backward from the last unit cell (or row) on the row bus (or main bus). The red and green lines show the coupling length required for a 120nm gap coupler to couple the right amount of light to the specific row and unit cell respectively. Note that the maximum coupling achieved in this figure is only 50%. The rest of the optical power in the silicon bus is discarded after the last row and after the last unit cell in each row through a gradual waveguide taper (as illustrated in Fig. 4.1). This is done in order to avoid the necessity to achieve 100% coupling efficiency in the last row/unit cell using an over-sized coupler. Doing so causes an acceptable power loss of ~12% in total which reduces even more, with up scaling, as a factor of $\sim 1/N + 1/M$, where N and M are the number of rows and columns in the array. It can be seen that for

our 16×16 NPA, the bus-to-row coupler length varies from 4.3μm (coupling efficiency = 5.9%) in the first coupler to 8.05μm (coupling efficiency = 50%) in the last coupler, as shown by the red line. The optical power is coupled in the same way from each row bus waveguide to the unit cells along it. The green line in Fig. 4.2 shows the row-to-unit coupler length varying from 3.3μm (coupling efficiency = 5.9%) to 8.12μm (coupling efficiency = 50%). The difference between the two types of couplers results from the different bend radius at the end of each coupler and the adiabatic characteristic of the unit cell bend which does not exist in the bus-to-row coupler.

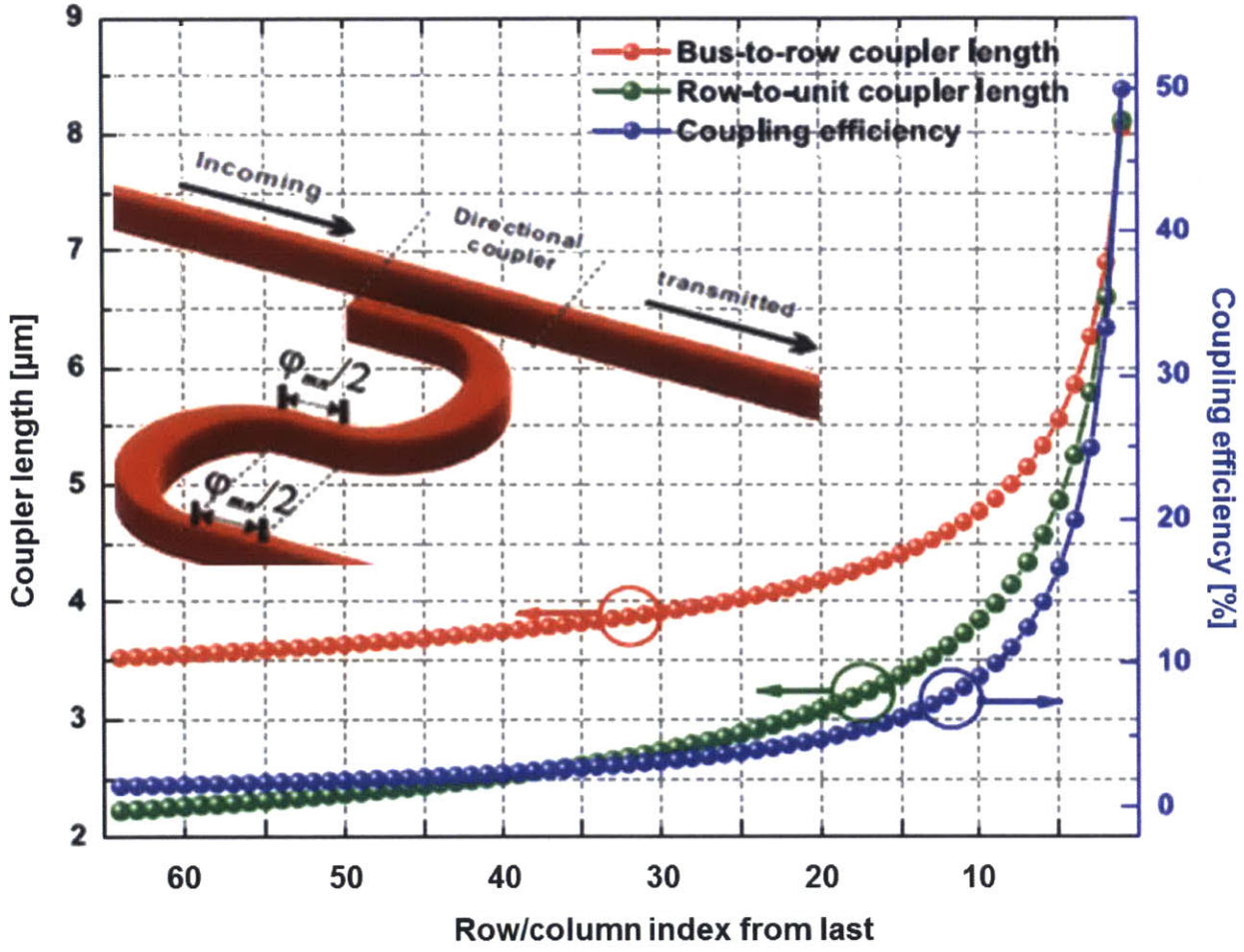

Fig. 4.2 Power and phase management: Coupling efficiency (Blue), and coupler length for the bus-to-row couplers (Red) and the row-to-unit cell couplers (Green) in the 2D NPA. The length of row-to-unit couplers is a little different from the bus-to-row couplers because different bend radii are used in the two cases. The coupler lengths are obtained through a 3D-FDTD simulation. Partial drawing of the unit cell is placed on the graph to illustrate the optical phase management in the unit cell. By tuning the length of the two sections market with $\varphi_{mn}/2$ we correct the phase non-uniformity of the different couplers φ_{mn}.

Moreover, phase management is another important aspect that needs to be carefully designed in the NPA to ensure all unit cells are tuned to response to the phase signal as desired without additional phase nonuniformity. Due to the small number of rows/columns, phase differences between different coupler

lengths on the cascade splitting architecture (as explained in Section 2.2) were calculated and taken into account. In other words, the zero-signal phase of all unit cells were corrected to be equal. This is achieved by two identical optical delay lines where each provides a propagation phase of $\varphi_{mn}/2$, where φ_{mn} is the correction phase for the unit cell (m,n). The coupler, as part of the unit cell, is illustrated on the graph of Fig. 4.2 with its two $\varphi_{mn}/2$ phase correction sections.

Nanoantenna Design: Ideally, the unit cell size should be less than half of the free-space wavelength λ_0 of the optical emission in both the x and y directions for the radiation to have a unique interference pattern in the far field without high-order radiation lobes (54), (74). It is therefore crucial to make the unit cell as small as possible in order to decrease the number of high order interference patterns in the far field. A compact and efficient optical nanoantenna is thus demanding for the NPA system. Optical nanoantennas down to subwavelength size have previously been demonstrated (64), (75), (76), (77), (78) with metal; however, to make the material systems compatible with the CMOS process, silicon-based dielectric nanoantennas are used (Fig. 4.3). The compact grating-based optical nanoantenna, measures 3.0μm in length, 2.8μm in width and 220nm in thickness, consisting of only five grating teeth. A partial etch 110nm in depth is applied to the first grating groove, to break the up–down symmetry of the nanoantenna for more upward emission (79). A SEM of the antenna is given in Fig. 4.3(a) showing the Si and half etched gratings. Fig. 4.3(b) shows the simulated emissions and reflection calculated using a three dimensional finite-difference time-domain simulation, in which 51% of the optical power emits upwards while only 30% emits downwards at λ_0=1.55μm. More efficient up-emission can be realized if a more optimized partial etch depth is used (the partial etch depth was fixed to 110nm in our process for the consideration of other devices on the same mask), or a reflective ground plane is implemented underneath the grating to reflect the downward emission. The graph in Fig. 4.3(b), shows the calculated far-field pattern of the optical nanoantenna, using the near-to-far-field transformation (80). The emission is not vertical because the grating period is slightly detuned from that of a second-order grating that would emit vertically, to suppress the resonant back-reflections; otherwise, significant reflection would interfere with the light propagation in the NPA (see Section 2.4 for theoretical elaboration). The emission from the nanoantenna is also broadband, with a bandwidth extending across hundreds of nanometers in wavelength, an inherent characteristic of the short length of the grating. This coupler could find potential applications such as broadband vertical couplers.

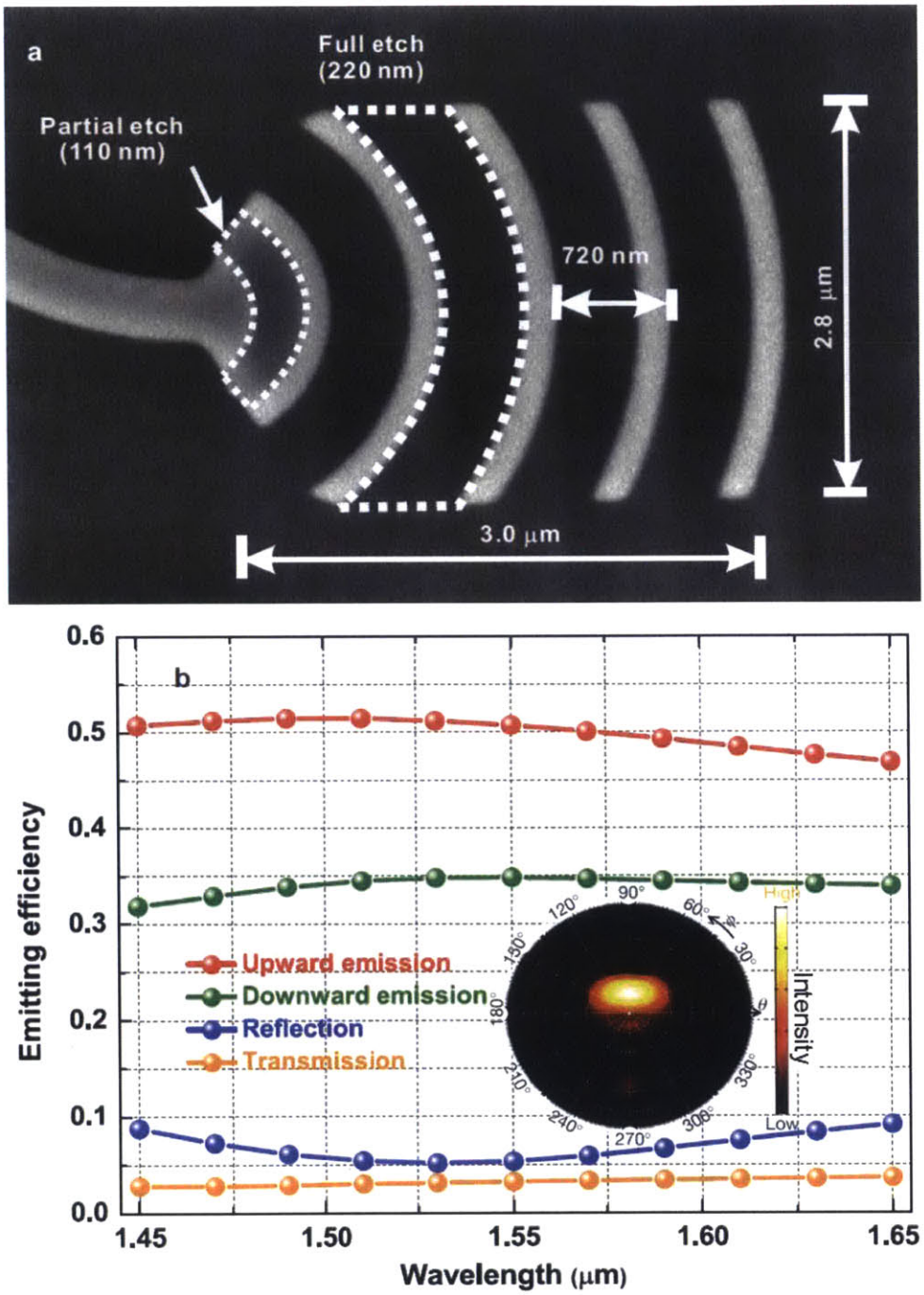

Fig. 4.3 Nanoantenna design: (a) A scanning electron micrograph (SEM) of the fabricated nanoantenna. The bright color represents silicon with a height 220nm while the dark color is the buried oxide (BOX), and the color in-between is the partially etched silicon with a height of 110nm. (b) The simulated grating emission efficiency. The up emission far-field radiation pattern of the optical nanoantenna is shown on the graph. This far field pattern was calculated from the near-field emission using the near-to-far-field transformation. The radiation fields in b are viewed from the zenith of the far-field hemisphere, as a projection of the far-field hemisphere to the equatorial plane in the polar coordinate system (θ, ϕ). θ and ϕ are the far field azimuth angle and polar angle, respectively.

Phase Shifter Design: For phase shifting we use the design described in Section 2.3. A section in the waveguide is low n-type doped to form a short resistor. This section can be electrically heated to create a

tunable thermal phase shifter. Two narrow silicon leads with heavy n^+-doping, providing electrical connections to and thermal isolation from the heater, are connected to the heater on the inner side of the adiabatic bends to minimize the loss caused by light scattering (35), (36). Fig. 4.4 illustrates the whole NPA design with the unit cell design in the inset showing the tunable phase shifter. The electrical controls are connected in rows and in columns to simplify the electrical circuitry.

The unit cell pitch is larger than a free-space wavelength. The beam shape is therefore replicated in the far field because the same interference conditions occur periodically in the far field to produce higher-order patterns. Eq. C.2 and Eq. C.5 in Appendix A indicates that the final far-field radiation pattern of the NPA is repeated in multiple orders (shown in Fig. 4.5 in the next section) according to the array factor. The emission pattern orders are only visible in the vicinity of the zenith, owing to the envelope dictated by the directional emission of the optical nanoantenna.

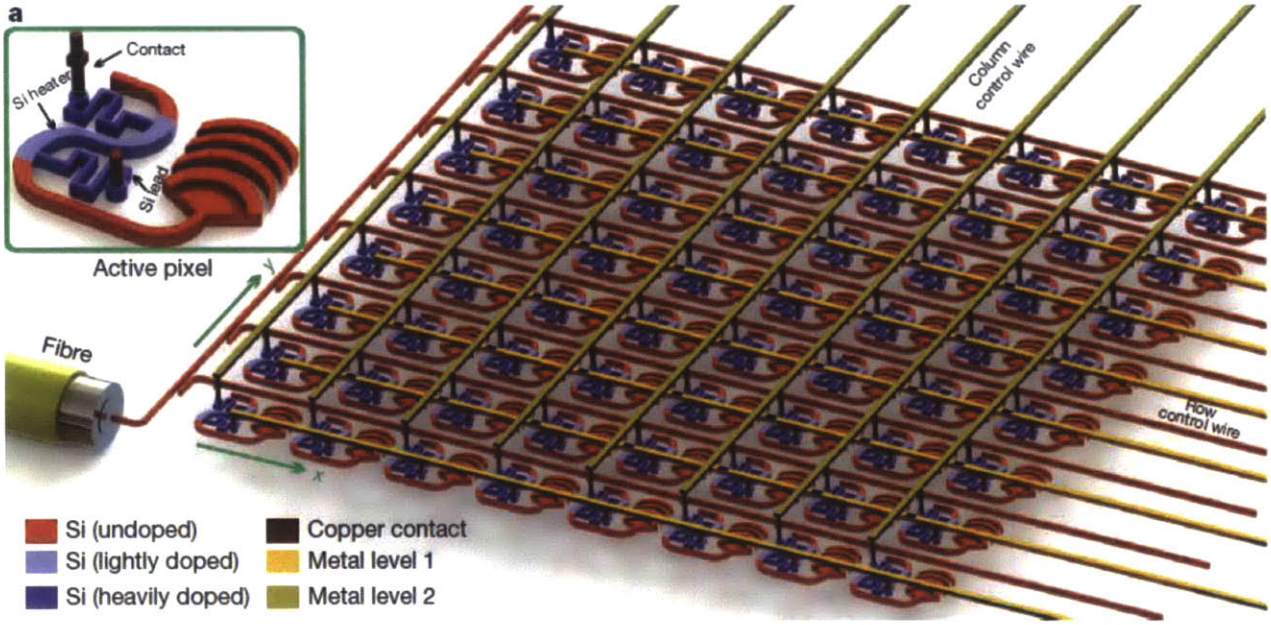

Fig. 4.4 Schematic illustration of the complete design of the 8x8 active NPA: Inset, diagram of an active antenna unit cell (size 9μm x 9μm). The optical phase of each unit cell is continuously tuned by the thermo-optic effect through an integrated heater formed by doped silicon.

4.3 Fabrication and Experimental Results

The designed 8x8 unit cells NPAs were fabricated in a 300mm CMOS foundry with 193nm optical immersion lithography (a 65-nm technology node) on silicon-on-insulator (SOI) wafers with a 220nm top silicon layer and 2μm buried oxide. A timed partial silicon etch (110nm) was first performed to make the partly etched grating groove. A full silicon etch was then applied to form the waveguides and grating nanoantennas. Subsequent n and n^+ dopings were implanted, followed by standard silicidation to make copper–silicon contacts. The contacts were connected to on-chip probing pads by two metal and a via layers for thermo-optic tuning. SiO_2 with a total thickness of 3.6μm was used to cover the devices, with a

final polishing step to make the surface planar to avoid additional phase errors due to surface corrugation. A 1.55-μm laser was coupled into the transverse electric mode of the main bus waveguide. The far field images were then captured with a near infrared (NIR) camera, using a setup similar to that in (81). The far-field image is clamped by the finite numerical aperture (NA = 0.4) of our objective lens.

The measured resistance is 2.5kV per heater including the two copper–silicon contacts, and a high thermal efficiency of about 8.5mW per π-phase shift is achieved, benefiting from the direct heating of the silicon waveguide. By applying different voltages on each unit cell, different phase combinations can be achieved in the NPA to generate different radiation patterns dynamically in the far field. As shown in Fig. 4.5, five different radiation patterns are demonstrated using the same NPA: a standard single-beam pattern with no voltage on the array; beam-steering for about 6° in both the vertical direction and the horizontal direction; generation of two beams in vertical direction; and generation of four beams in the horizontal direction. Good agreement between simulation and experiment is observed, which confirms the robustness of the proposed design as well as the accuracy of the fabrication and active thermo-optic phase tuning. Following the passive section of (6), the proposed active NPA structure can be immediately extended to a larger phased array (for example 64x64) with independent electrical control of each unit cell with the aid of fully CMOS-controlled circuitry to access all of the unit cells electrically and to project dynamic patterns in the far field with applications including communications, true three-dimensional holograms, light radars (lidars) biomedical imaging and interferometry.

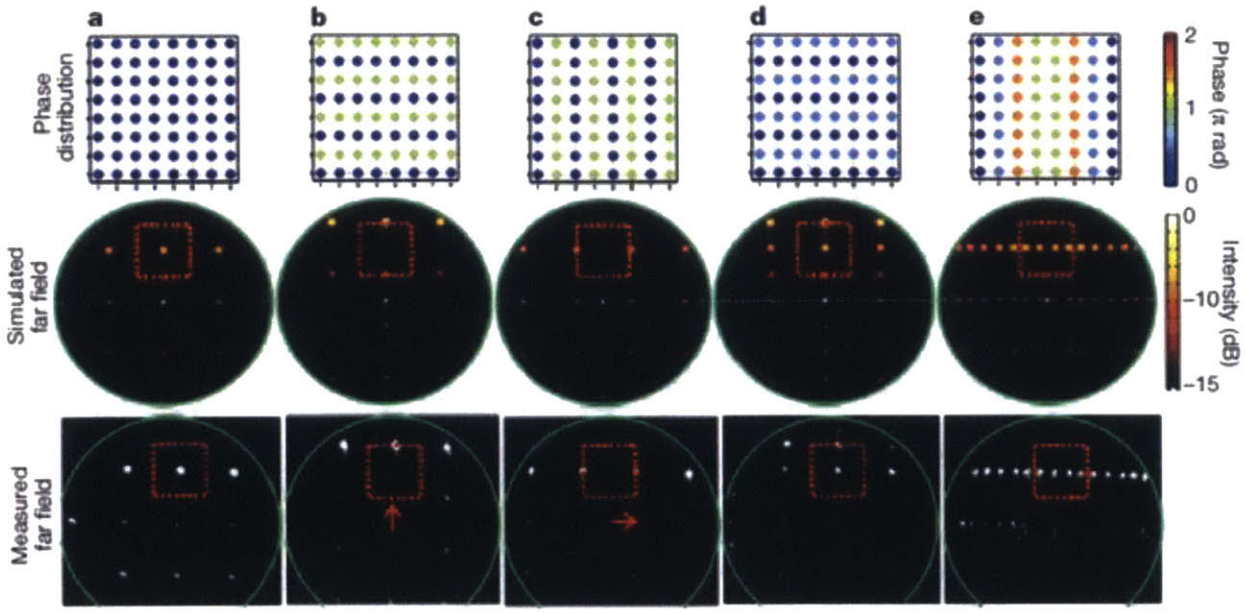

Fig. 4.5 Beam steering and forming: Examples of the dynamic far-field patterns generated by the 8x8 active NPA by applying different voltage combinations to the unit cells, showing simulations and measurements. (a) The original single-beam pattern with no voltage on. (b) (c) Steering the beam, by 6°, to the edge of each interference order in the vertical (b) and in the horizontal (c) dimensions. (d) The single beam is split into two beams in the vertical direction. (e) The single beam is split into four beams in the horizontal direction. The green circle indicates the edge of the lens NA (0.4), and the red box specifies the area of one interference order (see also the Supplementary Movie of (6) for the dynamic pattern generation).

4.4 Summary

We have demonstrated the large number of phased tunable nanoantennas which enables NPAs to generate arbitrary far-field radiation patterns dynamically and, in turn, to affect new fields such as communication, lidar, three dimensional holography and biomedical sciences. Our unit cell design is easily up scalable and was already demonstrated to create a 4096 antennas 2D NPA in (6). The ability to take advantage of a state-of-the-art CMOS integration process also promises a bright future for low-cost and compact NPAs that will be important in many fields with their newly explored functionalities.

5 Chip Scale Lidar System

5.1 Objectives

Light radar (lidar) systems today are used in variety of systems and are well known for their ability to produce a three dimensional map of their field of view. They are used in variety of fields from topography mapping (82), through ecosystem study (83), to 3D city modeling in urban control and taxation (84). Nevertheless, lidar systems to date are expensive and therefore cannot penetrate other markets that could largely benefit from their ability; one of which is the car industry.

Google with their autonomous car was already demonstrating self-driving ability using a lidar sensor on top of their car (see Fig. 5.1(a)) (85). Still, this sensor, shown in Fig. 5.1(b), apart from being extremely expensive (86) is bulky, includes complex optical assembly and is probably not as sturdy as desired for a commercial car component. Autonomous vehicles were also demonstrated using radar sensors and visible cameras. Cameras in the visible range enable the use of an extremely cheap sensor in mass production. Nevertheless, the image processing required to analyze the raw data coming from these cameras is expensive and sometimes incorrect. Furthermore, visible spectrum cameras reduce their performance drastically at night and require extremely high dynamic range to deal with light sources in the field of view at the same time they need to resolve objects in the darkness. Radar based sensors have good visibility in fog or smoke conditions but their resolution is extremely limited because of their long wavelength. In fact, at a range of 100m, their resolution is about 10m or more. Moreover, the bandwidth used by radar systems is limited to ~1GHz. This bandwidth together with the bandwidth requirements for a 1m range resolution enables less than 10 separate system bands and largely reduces the number of systems that can work together without interference. Lidar systems on the other hand enable sensors with high resolution and extremely large spectrum band (over 10,000 times larger than the available spectrum of radar systems) with night compatibility and direct range output that does not required much processing. Therefore, drastically reducing lidar price, and size as well as eliminating its fragility can be of high importance for autonomous vehicles as well as other applications.

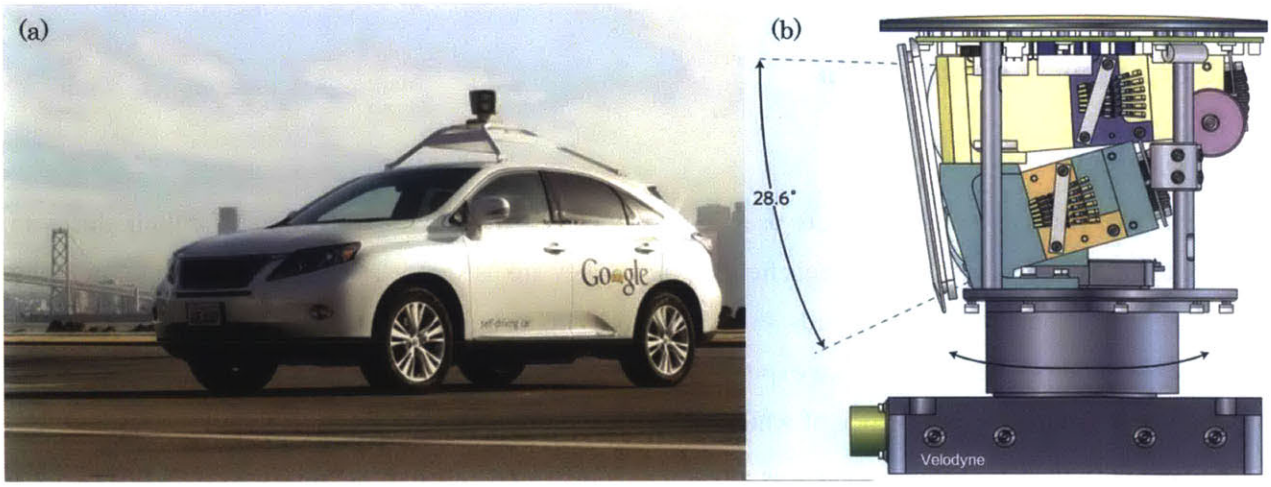

Fig. 5.1 Lidar for autonomous vehicles: (a) The Google car as presented in (85) and (b) a drawing of the lidar system which provides the car's main environment sensor (curtesy of Velodyne™)

Nanophotonic Phased Arrays (NPAs) together with other Si photonic components can solve all of these issues at once. Chip scale systems with on chip optics (no external lens assembly), on chip steering (no moving mechanical components) and other electro-optic manipulations can replace the large and expensive lidar systems in use today with an affordable unit price in mass production. Moreover, the small size and robustness of a chip base system inherently makes it sturdy and immune to mechanical shocks. In this chapter we will describe a coherent ranging method that suits nanophotonic systems, walk through its power budgets and show some ranging results with one of our systems. Then, we will present a NPA architecture that suites lidar applications and provide its beam steering measurements. Lastly, we will end with describing a lidar system design using two long NPAs of this type, operating as transmitter and receiver and bring its early results. While in this work we aim to demonstrate the integration of the main functions steering, frequency sweeping and detecting on a Si photonic platform, more complex and standalone photonic lidar systems can be designed. An on-chip laser source (87), (88) can also be implemented and the photonic chip can be integrated to a CMOS electronic chip (89) for SSB driving, signal processing and frequency analyzing but these are considered out of the scope of this work.

5.2 Nanophotonic Ranging

5.2.1 Background and Method

Light radars (lidars) are used in many applications today. However, at the moment, lidar systems are, at most, large, fragile and extremely costly (86). Precise laser beam steering imposes high end mechano-optics which is expensive and fragile, but the main cost comes from the common method of ranging which is based on a pulse Time of Flight (TOF) (90), (91). The need for precise ranging requires a short pulse in time, and peak power limitations bound the total energy (or number of photons) being sent in a

pulse. Large part of the pulse energy, scattered from the target, is lost when being collected with a reasonable receiver aperture size. The need of detection of this small number of photons collected by the receiver imposes the use of Avalanche Photo Diodes (APDs) that are extremely expensive and hard to produce at eye-safe wavelengths. Moreover, these APDs can be easily saturated by background light. The use of Si photonics technology not only allows for low cost, on-chip, steering, its single mode waveguide characteristic is applicable for coherent detection methods which allow for high dark current detectors, low transmission powers and insensitive to high background light. To be more specific, it allows the use of a different ranging method called Frequency Modulated Continuous Wave (FMCW) (91) that incorporates integrated non-avalanche photodiodes.

FMCW is a coherent method of ranging. Instead of sending a short pulse in time and measuring the time elapsed until some returning photons are collected, in FMCW a continuous wave is used. This allows the transmission of a high total energy optical beam per measurement, even with a pick power limited emitter. This wave is linearly chirped (i.e. frequency shifted linearly in time). The returning beam is then beaten against a local oscillator (LO) (a small portion of the chirped energy taken from before the emitter). The two beams together create an amplified beat node of frequency equal to the difference between the LO and returning signal frequencies. The beat node is said to be amplified here since it is much larger than the returning signal itself. This type of amplification does not amplify noises coming from dark current, background light or other noncoherent sources but only the coherent signal reflected from the target.

Fig. 5.2 describes a basic implementation of the FMCW method. The input CW laser frequency is chirped linearly in time using an on-chip Single Side Band (SSB) modulator (a linearly tunable laser can be used instead to avoid the need of an SSB). A small portion (e.g. 10%) of the optical pre-emitted power is tapped off to act as a LO (red line in Fig. 5.2(b)), and the rest is transmitted upon a target. The return signal (a delayed copy of the transmitted signal shown in green in Fig. 5.2(b)) is then collected by the receiver antenna and beaten against the LO to produce the beat node. This beat node frequency, Δf, is equal to the frequency difference between the two signals and proportional to the target range

$$\Delta f = \frac{df}{dt}\Delta t = \frac{df}{dt}\frac{2R}{c}. \qquad \text{Eq. 5.1}$$

Using a spectrum analyzer (or otherwise) the beat node frequency can be measured and the range to the target calculated.

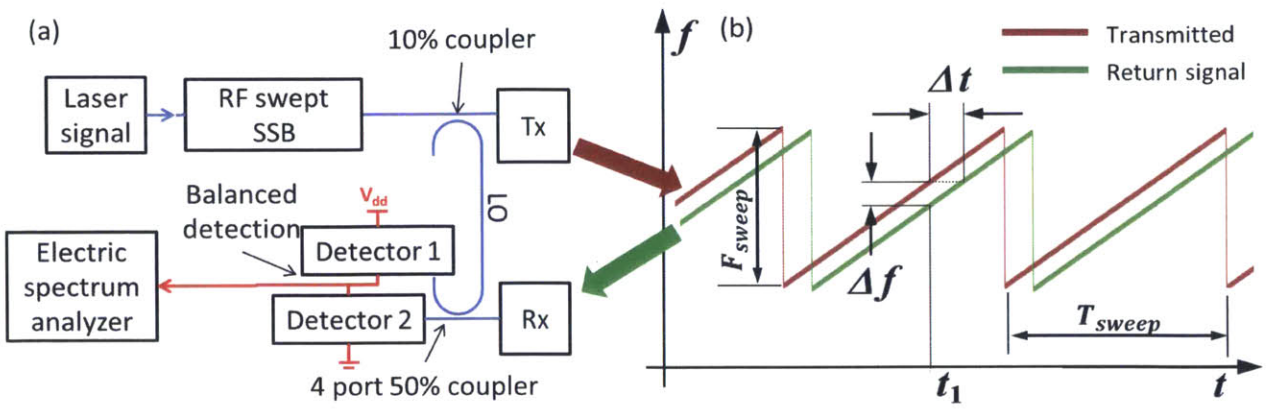

Fig. 5.2 FMCW method and basic implementation: (a) The FMCW system with blue lines representing optical waveguides and red lines representing electrical lines. (b) A figure of frequency vs. time of the LO and emitted light (red)) and return signal (green) to illustrate how the FMCW method works. Tx – Transmitter antenna, Rx – Receiver antenna, SSB – Single side band modulator, LO – Local oscillator.

In order to calculate the range resolution acquired with a specific setup we assume the sweeping time, T_{sweep}, is much greater than the time that it takes the light to travel to the target and back, Δt. There is no gain in sampling the beat node over multiple sweeps since the phase of the beat is not conserved between sweeps. Sampling the beat node over less than a sweep is, practically, like having shorter sweep. Therefore, the electric measurement bandwidth, BW, of the beat node is approximately $1/T_{sweep}$. The range resolution is, then, found by the product of the frequency resolution (electric bandwidth, BW) with the range to frequency derivative. Substitute the bandwidth and Eq. 5.1 gives

$$\Delta R = \frac{dR}{d(\Delta f)} BW = \frac{c}{2T_{sweep}\frac{df}{dt}} = \frac{c}{2F_{sweep}} \qquad \text{Eq. 5.2}$$

where $F_{sweep}$is the total optical frequency sweep of the system. Therefore, we can see that the range resolution is only dependent on the frequency sweeping range. While sweeping speed affects on sample capacity (measurements per unit of time) and, as we will see in the next section, on Signal to Noise Ratio (SNR), it does not affect the range resolution. This result is important since it shows the need for a specific bandwidth used by every system and, hence, expresses one of the benefits of lidar systems over radar systems which, as stated above, are occupying a band more than 10,000 times smaller.

5.2.2 Power Budget

In this section we calculate the SNR for a coherent lidar system. This input is important when designing a nanophotonic lidar to enable the right design parameters for the expected range performance. We start from the radar equation for receiver power (92)

$$P_R = P_T \frac{\sigma_t}{(4\pi)^2} \frac{G_{Tx} A_{Rx} e_{Rx}}{R^4} \qquad \text{Eq. 5.3}$$

where P_T is the emitted power, σ_t target cross section, G_{Tx} transmitter gain, A_{Rx} receiver aperture, e_{Rx} receiver efficiency and R target range. The transmitter gain assuming a collimated beam output is (92)

$$G_{Tx} = \frac{4\pi A_{Tx} e_{Tx}}{\lambda^2} \quad \text{Eq. 5.4}$$

where A_{Tx} is the transmitter aperture area, e_{Tx} transmitter efficiency and λ the emitted wavelength. For the case where the spot size is smaller than the target, the target cross-section for our transmitter-receiver system is simply the smallest spot size of the two on the target

$$\sigma_t = \rho \frac{\lambda^2 R^2}{\mathrm{A}} \quad \text{Eq. 5.5}$$

where A is the transmitter or receiver area and ρ is the target reflectance. The reflectance holds values between 0 for non-reflecting (black) target, 1 for perfectly scattering (white) target or greater for retro reflective target. It is clear from Eq. 5.5 that having the receiver and transmitter diffraction limited with different sizes does not benefit the target cross section and, hense, does not improve SNR. Therefore, we will treat A as A_{Tx} for the moment. It is important to note here that due to the single mode characteristic of our system (waveguide etc.), that is needed for coherent detection, making the spot size larger by distorting the beam does not help as well – the transmitter and receiver need to have the same far field pattern in order to maximize power collection. At the end of this chapter we will discuss a different way to increase the receiver effective aperture without changing its far field pattern and still gain in SNR. Substituting Eq. 5.4 and Eq. 5.5 with $A = A_{Tx}$ into Eq. 5.3 gives us

$$P_R = P_T \frac{\rho A_{Rx} e_{Rx} e_{Tx}}{4\pi R^2}. \quad \text{Eq. 5.6}$$

The power received to the receiver aperture is, for small aperture systems like NPA based lidars, extremely small given the large ratio between the receiver area, A_{Rx}, and the square of the range, R^2. Nevertheless, as we'll see in the next paragraph, the FMCW method enables measuring an extremely weak signal by beating it with a strong local oscillator (LO).

Next, we walk through the detection of the signal and calculate the SNR of the system from the received power. It is well known that by beating two signals with a frequency difference, a beat node that is equal in amplitude to twice the square root of the product of the powers is produced. The way we beat these two signals is by using a four port coupler to beat 50% of the P_R with 50% of the P_{LO} in each of its two output ports. The output ports are both connected to a respective photodetector. The two detected electrical signals are then subtracted by placing the photodetectors in series and measuring the excess current between them. This, while not improving the theoretical SNR, helps reduce LO fluctuations. Changes in the LO power will change the current of both detectors equally which will be subtracted out in the balance detection. The beat signal on the other hand is in a 180° phase difference between the two

output ports which will add in the balanced detection method. The beat node strength, given the receiver power, P_R, and LO power, P_{LO}, with a photodiode responsivity $\Re$ is then given by

$$I_{sig} = 2 \times 2\Re\sqrt{0.5P_{LO}0.5P_R} = 2\Re\sqrt{P_{LO}P_R} \Rightarrow I_{sig}^{RMS} = \Re\sqrt{2P_{LO}P_R} \quad \text{Eq. 5.7}$$

where the $2\times$ is to denote the addition of the two signals in the balanced detection the 0.5's are for the 50% splitting in the four port coupler and the Root Mean Square (RMS) signal $I_{sig}^{RMS} = I_{sig}/\sqrt{2}$. Calculating the noise, we look at the DC level of each of the photodiode currents, I_{DC}, which, assuming that $P_{LO} \gg P_R$ and that the local oscillator current is larger than the dark current, is simply

$$I_{DC} = \Re 0.5P_{LO}. \quad \text{Eq. 5.8}$$

Assuming well designed read out electronics, the detection is shot noise limited by the receiver DC current. The resulted shot noise of a single detector is then (93)

$$I_{shot}^{\text{single}} = \sqrt{2qI_{DC}BW} = \sqrt{q\Re P_{LO}BW} \quad \text{Eq. 5.9}$$

where q is the electron charge and BW is the measurement bandwidth, and when adding the uncorrelated noise from the two detectors

$$I_{shot}^{total} = \sqrt{I_{shot}^{\text{single}^2} + I_{shot}^{\text{single}^2}} = \sqrt{2q\Re P_{LO}BW}. \quad \text{Eq. 5.10}$$

Lastly, we calculate the SNR by dividing the signal current from Eq. 5.7 by the shot noise current from Eq. 5.10 to get

$$SNR = \frac{I_{sig}^{RMS}}{I_{shot}^{total}} = \sqrt{\frac{\Re P_R}{qBW}} = \sqrt{N_{pe}}. \quad \text{Eq. 5.11}$$

where N_{pe} is the number of photo-electrons produced in the detectors in the time T_{sweep} and originates by the returning light from the target. It is clear from this result that although the sampling capacity (range measurements per time) can increase linearly by reducing the sweep time, the SNR will degrade as the square root of the sweep time. More importantly, from Eq. 5.11 we can see that as long as the LO current is larger than the dark current and background light, the SNR is shot noise limited depending only on the received power. This is the fundamental limit for SNR in optical detection systems and is reached here with integrated detectors rather than the expensive APDs used in other systems.

It is important to note here that, although (as discussed above) a large receiver NPA does not increase SNR without increasing the size of the emitter as well, multiple receivers can produce an effective large receiver and improve SNR. As discussed above, the coherent method we are using requires single mode waves to interfere with each other. Nevertheless, the returning light from the target is a scattered light and, therefore, includes many modes which can each interfere separately with a LO signal to create a beat node. By placing several receivers next to each other, each of the size of the transmitter, we can collect more modes of the returning light independently. Then, by beating each receiver against a LO and

analyzing the spectrum of the signal, we get the SNR calculated above in each receiver. Summing the spectral result from all the receivers (amplitude vs frequency) will improve the signal as a square of the number of receivers since the noise of the different signals is uncorrelated. True, the different signals cannot be summed on the optic or electronic levels due to their random phase in respect to each other, but summing the amplitude of the spectral response drops this phase from the sum and allows for the stated SNR improvement. Since we can see from the above that the SNR enhancement goes as the square root of the optical collection area, and since the number of photons being collected is increasing linearly with area, it is clear that the new SNR with multiple receivers system still goes as $\sqrt{N_{pe}}$. Hence, this method of increasing SNR is still shot noise limited to the returning power from the target. Fig. 5.3 shows a synthetic example of possible electric spectral power from a single receiver Gaussian distribution noise source SNR = 2 and after summing the spectral power of 4 individual (independent) receivers.

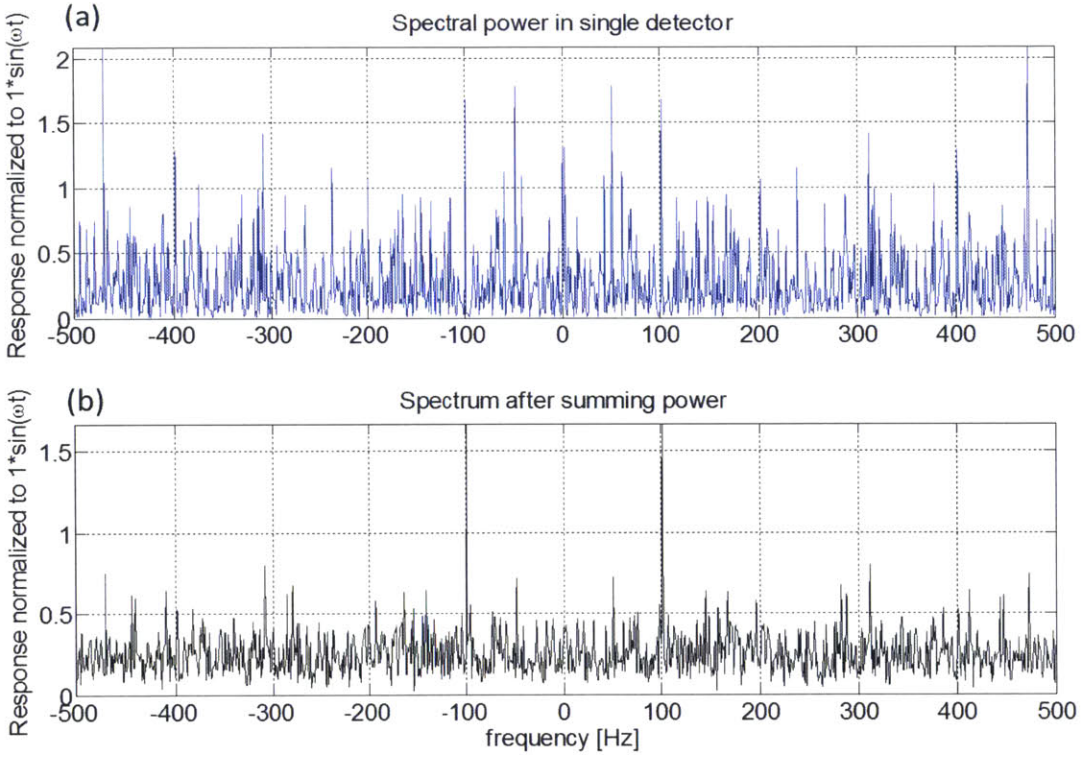

Fig. 5.3 Multiple receivers synthetic simulation: (a) A spectral power response of a single signal at 100Hz and with SNR = 2. (b) The spectral power after summing over four different detectors.

Table 5.1 shows a set of values we believe we can achieve and the resulting SNR showing its ability to operate in systems that to date were either using extremely expensive lidar systems or no lidars at all for their high price. This result of high SNR = 10 with such a small system and with a range of 100m being achieved with an integrated detector with normal dark current levels is possible only by the use of

coherent detection, a method that suites Si photonics technologies for its single mode waveguide characteristics.

Parameter Name	Symbol	Value
Antenna array efficiencies	e_{Tx}, e_{Rx}	6dB
Receiver area	A_{Rx}	10mm^2
Target reflectance	ρ	10%
Range	R	100m
Transmitter power	P_T	0.1W
Photodiode responsivity	$\Re$	0.8A/W
Bandwidth	BW	10kHz
SNR	SNR	10

Table 5.1 Expected Parameter values for example system and scenario, and the driven expected SNR

In order to demonstrate nanophotonic lidar we first demonstrate the ability to measure range using the FMCW method and propose a new NPA architecture suit for lidar application separately. Only then, we describe a nanophotonic lidar design that includes both FMCW components and beam steering on chip. The last is still in the process of fabrication and only preliminary results are presented. In the next section, we demonstrate FMCW ranging with nanophotonic components.

5.2.3 Nanophotonic FMCW Ranging

First we describe the design of a nanophotonic ranging demonstration to show the feasibility of such system. In order to demonstrate such ranging we use a nanophotonic system designed for interferometry and described in detail in (94). We incorporate the use of two main components shown in Fig. 5.4. Single sideband (SSB) modulators, shown in Fig. 5.4(a) with its spectral performance in Fig. 5.4(b), and Ge based detectors for balanced detection shown in inset of Fig. 5.4(c) with its spectral response ([A/W]). It can be seen that the Ge detector, with the right design, allows for responsivities of over 0.8A/W at a wavelength of 1550nm and the single side band modulator can operate with ~20dB side lobe suppression. The Ge detector and SSB modulator are described in depth in (89) and (95) respectively.

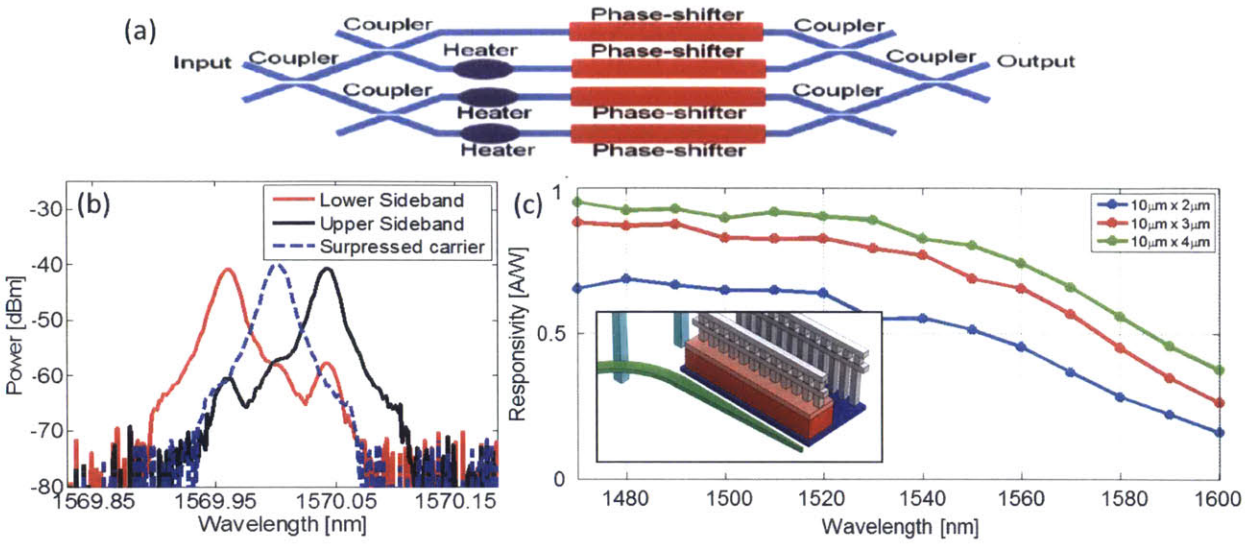

Fig. 5.4 Components for on chip lidar system: (a) A schematic drawing of the SSB, as designed and measured by C. M. S. Agaskar (95), where the heaters are low frequency phase shifters for tuning the SSB operation point, and the phase-shifters are p-n junction based phase shifters modulated with RF frequencies. (b) The SSB spectrum where the dashed blue line is for SSB turned off (no RF input) and the black and red lines are for the two outputs of the SSB. (c) The spectral response of the Ge detectors shown in the inset, designed and measured by E. Timurdogan et al (89).

The interferometric system is built by placing two SSBs in parallel. The first output port of each SSB is beaten against each other and to form a reference signal. The second output of one SSB modulator is coupled out of the chip through a fiber coupler to be projected on a target, reflected and coupled back to the chip through another fiber coupler. This signal is beaten against the second output of the other SSB. See inset of Fig. 5.5 for the system architecture. We placed the system with focusing optics and a retro reflector to enable high efficiency power collection on the small waveguide mode at the chip edge. We then used the two SSBs in the design with two constant frequencies to shift the LO and the transmitted signal 20MHz and 20.5MHz from the laser input wave. The frequency sweep for the FMCW method was done using a tunable laser feeding the chip and a sweep rate of 1.25THz/s was used over a band of 10nm. The results can be seen in Fig. 5.5 where three different beat nodes are clearly seen on frequencies 2kHz, 3.7kHz and 5.4kHz for range measurements of 10" 18" and 26" respectively. These frequencies were taken from the offset frequency which is the difference between the two SSBs (500kHz). The frequency offset between the two SSBs was used to avoid low frequency signals which are harder to filter and sample. Calculating the expected beat node frequencies for these 10", 18" and 26" ranges from Eq. 5.1

$$\Delta f = \frac{df}{dt}\frac{2R}{c} \qquad \text{Eq. 5.12}$$

gives the same frequencies measured with an error of ~100Hz (less than 5%) that are probably due to placement errors of the target.

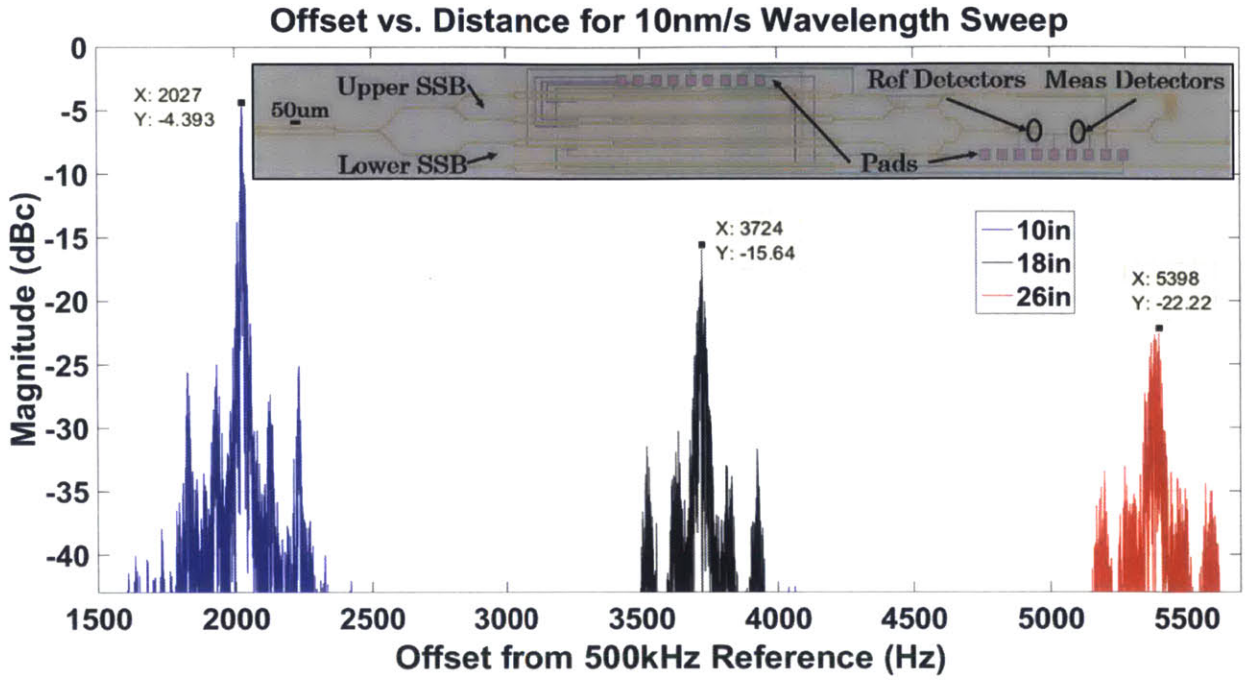

Fig. 5.5 FMCW with on chip components: Ranging of 10" (blue) 18" (black) and 26" (red). Beat nodes are clearly seen 10dB - 20dB above side lobes.

5.3 Emitter and Receiver

Next we demonstrate a Si based NPA fabricated in a CMOS compatible process with continuous, fast (100kHz), wide-angle (51°) beam-steering suitable for applications such as low-cost lidar systems. The device demonstrates the largest (51°) beam-steering and beam-spacing to date while providing the ability to steer continuously over the entire range. Continuous steering is enabled by a cascaded phase shifting architecture utilizing, low power and small footprint, thermo-optic phase shifters. We demonstrate these results in the telecom C-band but the same design can easily be adjusted for any wavelength between 1.2-3.5μm.

5.3.1 Introduction

Si based NPAs have been widely investigated in the last few years (6), (65), (96), (97) for applications in many fields including holographic video displays, optical communication systems, and low cost lidar systems. In particular, low cost chip-scale lidar can, in principle, dramatically enhance accident avoidance systems in the automotive industry (86), (98), (99), (100). Yet, automotive applications impose constraints that are challenging for NPAs. While two-dimensional beam steering is usually not required, high-speed continuous beam steering is often necessary. Architectures mentioned in (6), (96), (97), (101), (102) utilize lookup tables (LUTs) to determine the required signal for every beam angle. For continuous steering in such systems, a delay is required for the phase shifters to stabilize at every step of the sweep, substantially increasing the time of the sweep by the product of the number of

angular steps required and the associated relaxation time for each step in angle. With the architecture given in (28), such a delay is not required, but the power needed for steering increases as the square of the number of antennas thereby restricting the scaling of the array. More importantly, for efficient, large-angle, and low cross-talk operation, a large angle between the different optical orders is necessary. Despite the substantial progress in NPAs, current systems can only steer across a maximum of ~24° (96), whereas, autonomous vehicle applications typically require scan angles exceeding 45°.

Here we demonstrate a high-speed, low-power and wide-scan-angle NPA. The array is based on a novel phase shifting architecture. The approach utilizes 32μm long grating based antennas, fed through evanescent field waveguide couplers from a bus waveguide with directly integrated thermo-optic phase shifters (36), (38). The demonstrated NPA is continuously steerable over a 51° angular range with a 10.6V signal, an average power consumption of ~18mW/antenna and a 3dB cutoff speed of 100kHz. We operate this array at the eye-safe 1550nm wavelength, but the design can easily be converted to work at any wavelength between 1.2-3.5μm allowing for tens of thousands of lidar systems to work together without interfering, an important feature for accident avoidance applications.

5.3.2 Design

As stated above, when designing a NPA, pushing the side lobes (or orders) farther apart is extremely important. Side lobes radiate power in undesired directions that would otherwise go into the main beam and thereby increasing the probability of crosstalk between different ports while reducing the gain of the NPA antenna. The presence of side-lobes also indicates a narrowed steering angle since there is no benefit in steering beyond the spacing of two consecutive beams. We define the beam spacing, $\Delta\phi$, as the angle between the fundamental (emitting straight forward) and the next order lobes. This angle can be derived by applying the first-order constructive-interference condition on the array antennas with all of the antennas emitting at the same phase, and it is related to the antenna pitch, d, by

$$\sin(\Delta\phi) = \frac{\lambda}{d}, \qquad \text{Eq. 5.13}$$

where λis the laser wavelength (see Appendix A). Thus, increasing the angle between two consecutive lobes requires narrowing the antenna spacing. Unfortunately, since the antenna spacing needs to approach a half-wavelength to achieve the full 180° steering range, approaching this range prevents other components from existing between the antennas (e.g. preventing phase shifters as in (6), and/or waveguides to different antennas as in (24)). Given that Si photonics is inherently two-dimensional, extracting other components from between the antennas limits the array to one dimensional electrical steering. In the longitudinal direction, i.e. along the antenna waveguides, the emission angle of the N^{th} order θ_N, in air, is given by (103)

$$\sin(\theta_N) = n_{eff} - \frac{N\lambda}{\Lambda}, \qquad \text{Eq. 5.14}$$

where n_{eff} is the waveguide effective index and Λ is the grating period. Since, in our case, $\lambda/\Lambda = n_{eff} > 1$ only the first order exists in the longitudinal direction (see Fig. 5.7(a) for the definition of angles).

The cascaded phase shifting architecture shown in Fig. 5.6(a) combines the splitting and phase shifting stages described in Chapter 1, and therefore enables continuous steering using one input signal. By driving all of the cascaded phase shifters with the same voltage, a constant phase difference between consecutive antennas is developed, enabling continuous steering. This is different from earlier designs mentioned above. In (6), (96), (97), (101), (102), a look up table (LUT) and specific set of signals are needed for every angle of steering making a continuous steering very slow for the relaxation required from the phase shifter. In contrast, in the cascaded phase shifting architecture, an electrical power signal is linearly translated to the beam angle, therefore the cutoff steering frequency is equal to the phase shifter cutoff frequency allowing for high speed steering. Compared to the architecture shown in (28) our design, regardless of the size of the array, requires equal power for all antennas and is easily scalable to larger arrays. As a consequence, the cascaded phase shifting architecture enables continuous and high-speed steering with low power consumption.

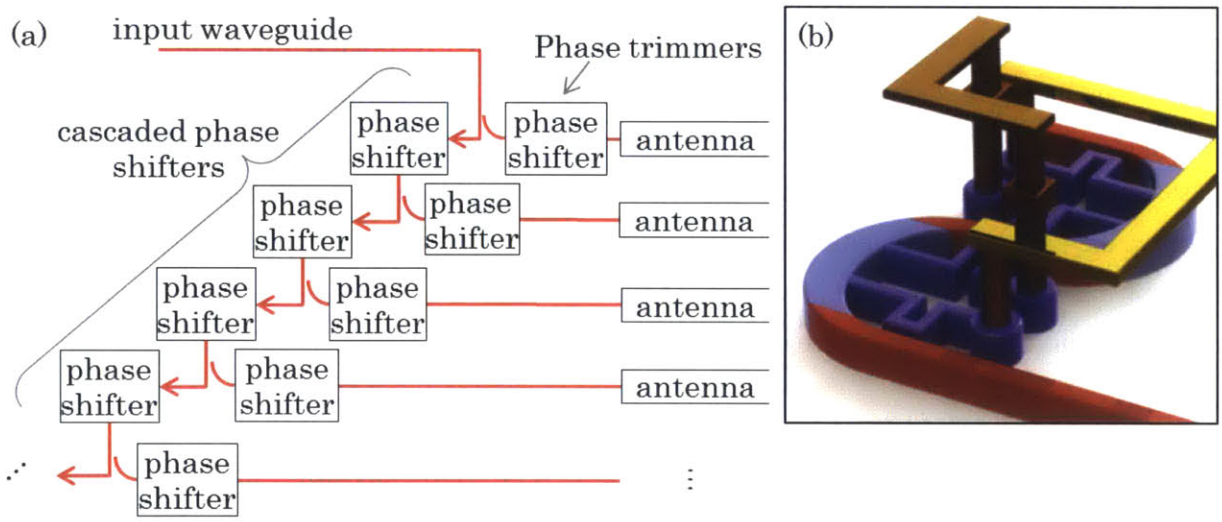

Fig. 5.6 Architecture and phase shifter: (a) The architecture of the NPA showing the cascaded phase shifting drawn compatibly with Fig. 5.8(a). The red lines show the waveguide paths and the redundant phase trimmers were drawn to illustrate the components shown in Fig. 5.8(a). (b) A schematic of the phase shifter showing the intrinsic waveguide (red), the lightly doped heater (blue), the high doped Si wires contacting the heater (purple) and the metals and contacts (gold/brown).

Phase shifting is achieved using the thermo-optic effect in silicon in which a part of the waveguide was doped to form a resistive heater. To achieve electrical contact to the heater elements integrated in the waveguide, we use an S-shaped adiabatic bend, broadening the waveguide width from 400nm to 1μm in the middle of each curve and back to 400nm. This type of bending and broadening pushes the mode away

from the inner part of the curve, allowing electrical contacts to be made with minimal scattering losses (36), (38). Such an S-shape structure also allows for a larger phase shift in a small footprint. Additionally, the use of highly doped, zigzagged, silicon lines enables electrical contacting to the waveguide without melting the metal-to-Si contacts at the waveguide's high temperatures. Fig. 5.6(b) shows the phase shifter design where intrinsic, low, and high doping levels are shown as red, blue, and purple respectively. COMSOL™ simulations show that the high temperature shift applies not only to the doped volume, but flows quickly along the waveguide, thus enabling larger phase shifts. Finally, by directly heating the waveguide, which has a small volume and low heat capacity, we are able to reduce the total heating energy required for a given phase shift thus allowing for more efficient, high speed phase shifting. Ref (36) shows a single phase shifter of this type to have a time constant of $\tau \sim 2.2 \mu sec$. In order to calculate the 3dB cut-off frequency f_{3dB} of the steering resulting from this phase shift time response, we compare the absolute value of the Fourier transform to 1/2

$$\left| \frac{1}{1 + j2\pi f_{3dB}\tau} \right| = \frac{1}{2}. \qquad \text{Eq. 5.15}$$

Since the angular response is linear with phase, we do not need to square the Fourier transform as is done when a power cutoff frequency is calculated. The 3dB cutoff frequency of this phase shifter f_{3dB} is, following Eq. 5.15,

$$f_{3dB} = \frac{\sqrt{3}}{2\pi\tau} = 125kHz. \qquad \text{Eq. 5.16}$$

More detailed elaboration on the phase shifters (and couplers) is given in Sections 2.2 and 2.3.

When a large aperture is needed, for diffraction or energy collection reasons, the one dimensional characteristic of the array forces long optical antennas to cover the necessary aperture size. The antenna gratings were designed using a shallow etch on the sides of the waveguide. In this manner, the interleaving of shallow etched and fully etched silicon regions can be controlled very accurately enabling infinitesimal perturbations to be imposed at the antenna input and continuously stronger perturbations as the light propagates deeper in the antenna so as to ensure uniform power extraction from the decaying mode amplitude. This extraction has to meet an equation similar to Eq. 2.9 but instead the extraction here is continuous and has units of part per μm:

$$Ext(x) = \frac{\Lambda_{array} I(x)}{P_{end} + \Lambda_{array} \int_x^{end} I(x)dx} \qquad \text{Eq. 5.17}$$

where $I(x)$ is the global near field intensity emitted from the array at point x along the antenna to all directions, Λ_{array} is the pitch of the array between antennas so $\Lambda_{array} I(x)$ is the power extracted from the antenna per unit length and P_{end} is the power left to be disposed at the end of the antenna. For flat

intensity design of antenna and assuming negligible power is left to be disposed at the end of the antenna, Eq. 5.17 simply becomes

$$Ext(x) = \frac{1}{L-x}. \quad \text{Eq. 5.18}$$

3D FDTD simulations (see Appendix A) were used to determine the grating strength (width of shallow etches into the waveguide) and the pitch along the emitter waveguide. Fig. 5.7(a) shows a section of the antenna simulated between two adjacent antennas with flux monitors for up/down emission, transmission and reflection. A number of simulations were done to analyze the power extraction from the waveguide as a function of perturbation strength and a fit to the equation $Ext(W) = aW^b$, where W is the etch width and a and b are parameters, was made. Fig. 5.7(b) shows the extraction required per μm at a certain distance from the end of the antenna $(L - x)$ together with (Fig. 5.7(c)) the extraction as a function of perturbation width. The 100μm point is given as an example with a needed 0.01/μm (-20dB/μm) extraction and corresponding perturbation width of 33nm. Using Eq. 5.18 and the fit to the FDTD simulation results, the grating strength was adjusted to ensure uniform intensity of emission along the antenna length. In addition, by looking at the phase change along the grating section, we tuned the grating pitch, for each strength, to minimize aberrations and ensure a collimated beam. Fig. 5.7(d) shows the simulation results together with a linear fit used to determine the specific pitch at each strength. In our 100μm example, the pitch at this point needs to be 710nm. These FDTD simulations also reveal minimal coupling between adjacent antennas even when antenna waveguides are placed as close as 1μm apart (1.4μm in pitch).

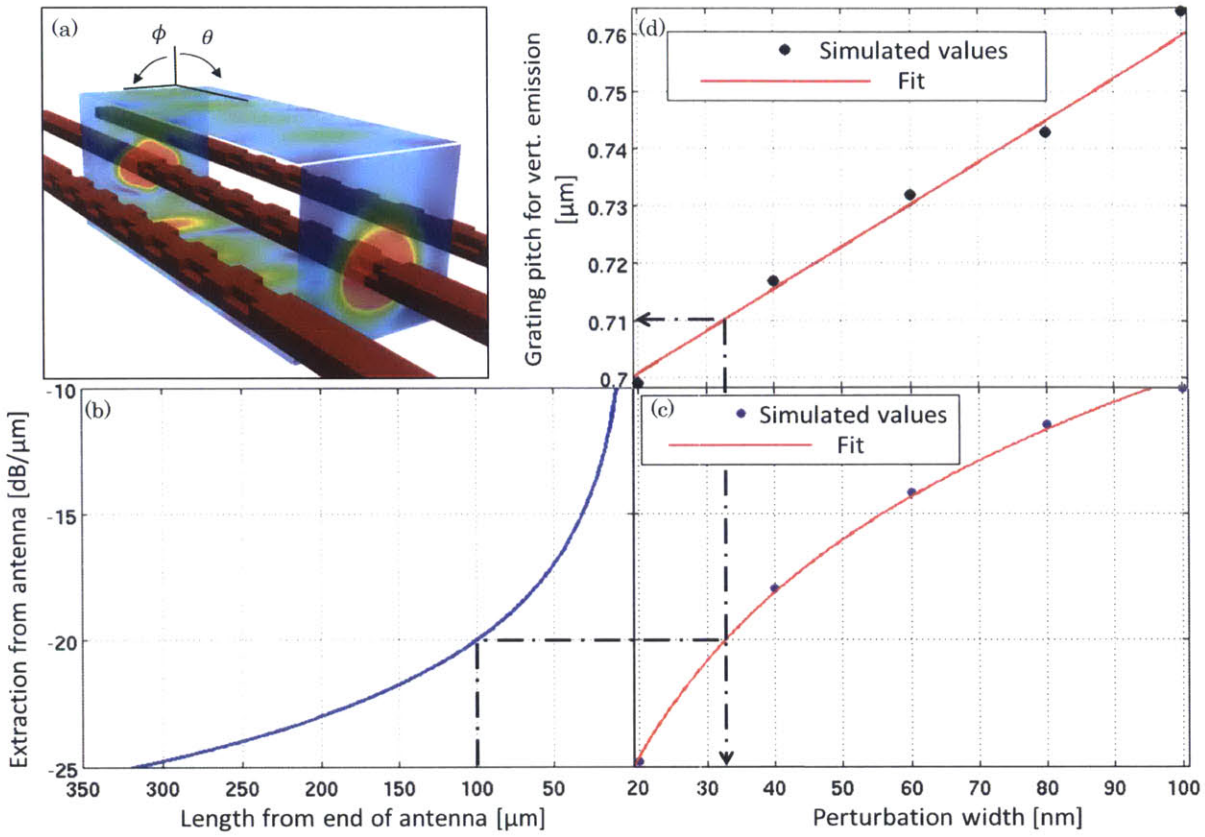

Fig. 5.7 Antenna design: (a) An FDTD simulation of a small section of the emitters showing the flux monitors used for calculating the amount of power extracted from the waveguide per unit length. An illustration of lateral, ϕ, and longitudinal, θ, angles is added at the top. (b) The required extraction from antenna per μm as a function of distance from the end of the antenna, (c) simulated extraction values and (d) simulated required grating pitch as a function of shallow etch width. The red line in (c) represents a fit to the equation $Ext = a * W^b$ and the red line in (d) represents a linear fit.

As a result of this gradually increasing perturbation design, the forward/backward symmetry of the antenna is also broken allowing for higher coupling efficiency between the waveguide propagating mode to the emitted free space mode. Unfortunately the up/down symmetry in our design is not efficiently broken and FDTD simulations show that about half of the light emits in the downward direction. Considering this and power loss to side lobes, the total efficiency was estimated. It is important to note here that in addition to the free space expected side lobes, discussed in Eq. 5.13, there are slab modes that can be excited by the NPA. In other words, the condition for no side lobes inside the SiO_2 cladding requires even smaller antenna pitch. Since the refractive index of the SiO_2 layer is 1.445, a 2μm pitch almost supports an additional slab mode which appears with the slightest steering angle. Thus, the total number of modes emitted from the array is ~8 (4 up and 4 down) and the single mode efficiency is estimated to be greater than 10%.

5.3.3 Fabrication

The array was fabricated in a 300mm CMOS compatible foundry using 193nm optical immersion lithography on a silicon-on-insulator wafer with ~$1x10^{15}cm^{-3}$ p-type, 220nm thick silicon on a 2μm thick buried oxide. The process included a deep (220nm) etch and shallow (110nm) etch to define the silicon layer, low ($2x10^{18}cm^{-3}$) and high (~$10^{20}cm^{-3}$) n-type doping levels, two layers of copper and aluminum metal interconnects and their via contacts to the silicon layer. The phased-array structure was formed by combining the aforementioned components in such a way that the antenna spacing is minimized, and thus the beam spacing is maximized. By placing sixteen, 32μm long grating-based antennas described earlier, with a 2μm pitch, a 32μm x 32μm array was created. A Scanning Electron Microscope (SEM) image of the fabricated array can be seen in Fig. 5.8(a) while the inset shows how the phase shifters are integrated in the cascaded architecture. A close-up on the individual phase shifter can be seen in the false-colored SEM in Fig. 5.8(b) showing its different doping levels as red, blue, and purple representing intrinsic, medium, and high doping levels respectively. An optical path of length ~1.5μm, average width of ~0.75μm and thickness of 0.22μm, medium doped, yields a total resistance of ~6.2kΩ per S-curve. The two curves, connected in parallel in each phase-shifter create heating of around 500°C and change the Si refractive index by ~3.2% (104) with 10.6V applied. Fig. 5.8(c) shows two close-up views of the gratings, at the beginning and end of one antenna, demonstrating the weak and strong perturbations mentioned above respectively. In agreement to Eq. 5.13, a 51° beam spacing in the lateral dimension was achieved and in agreement with Eq. 5.14 no additional beams were observed in the longitudinal direction.

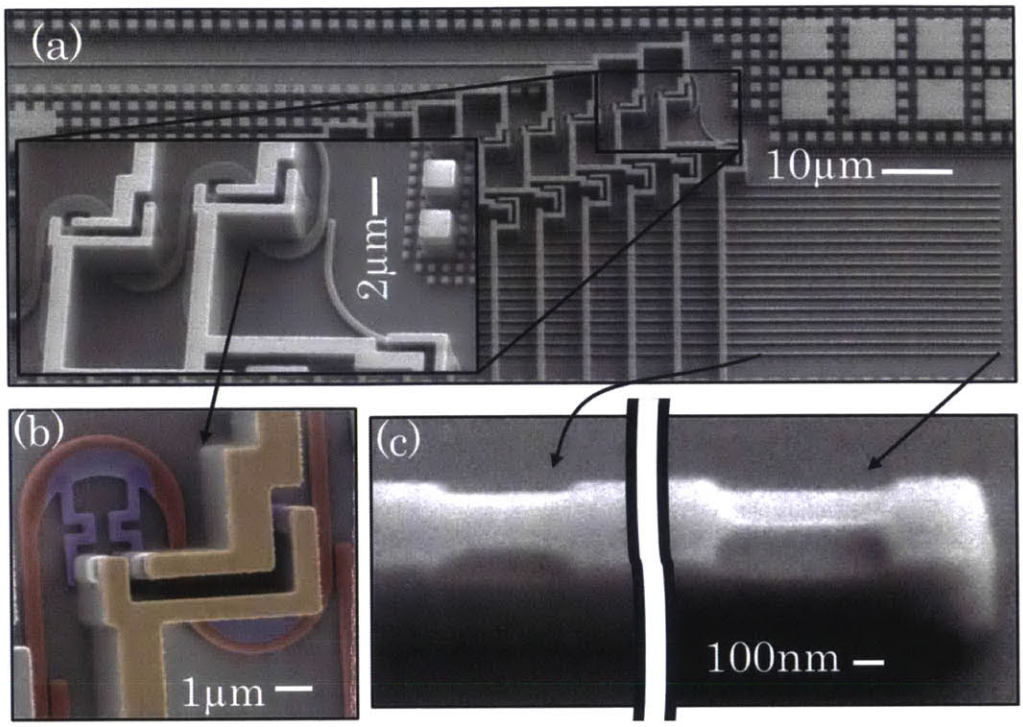

Fig. 5.8 Fabrication: (a) A SEM image of the array showing the whole device and another SEM image (inset) magnifying the first two cascaded phase shifters. (b) A false-colored SEM of a single phase shifter illustrating the intrinsic waveguide (red), low doped resistor (blue) and high doped Si wires (purple). (c) SEM images of the first and last antenna gratings showing the difference in grating strength along the emitter. All SEM images were taken after removing the SiO_2 cladding.

5.3.4 Experimental Results and Discussion

In order to measure the far field of our NPA we used the system illustrated in Fig. 5.9(a). A laser with a cleaved fiber and polarization controller were coupled to the chip and the optical power emitted from the array was then captured by an objective lens with declared 0.4 NA at the visible range. A dichroic mirror was then used to split the light to a visible arm, used for fiber and probe alignment, and a Near Infrared (NIR) arm, used for signal monitoring. While the visible arm was focused straight into the visible camera, the NIR arm was built as a bifocal system where, on the second stage, a lens was placed in one of two position points to allow either near field or far field recording. The red lines in Fig. 5.9(a) show three NIR beams propagating though the optical system. There are three red lines in the figure, two solid ones showing the focus of near field image and a dashed line showing a path with similar k vector to one of the solid lines and how it is being focused on the NIR camera when the lens is in its far field position. Fig. 5.9(b) shows a 3D intensity plot of the beam (inset) and a specific plot of the spot's intensity cross section as a function of θ and ϕ. The far field angular response of the camera (pixels/degree) was found using the set of zeros of the intensity-vs.-ϕ curve and the lens was found to have an effective NA of 0.32 at a 1550nm wavelength. The far field Full Width at Half Maximum (FWHM) spot size was measured to be 2.46° in the θ (longitudinal) direction, which is exactly the diffraction limit for a 32μm rectangular aperture. In the ϕ (lateral) direction, the FWHM of the beam was found to be 2.67°, only slightly more

than the diffraction limited value. Fig. 5.9(c) shows the beam steering angle as a result of all-optical heating in the waveguide. The steering effect in our experiment was much less than one camera pixel and the use of strong interpolation (x50) and correlation between images was necessary to produce this plot. Although this curve is expected to appear linear at low powers (ohmic heating from doped regions), it looks like the linear component is negligible and the dominant component is related to two photon absorption and thermal relaxation. The fitting curve's second order component is found to be 0.35×10^{-3} deg/mW^2. Still, at 12mW the steering is much less than the beam width (0.05° only). Even when ramping the optical power to 100mW (well beyond the non-linear limit of a common Si waveguide), the extrapolated resulting steering is not expected to exceed 4° which is well within the steering range and can be easily electrically corrected.

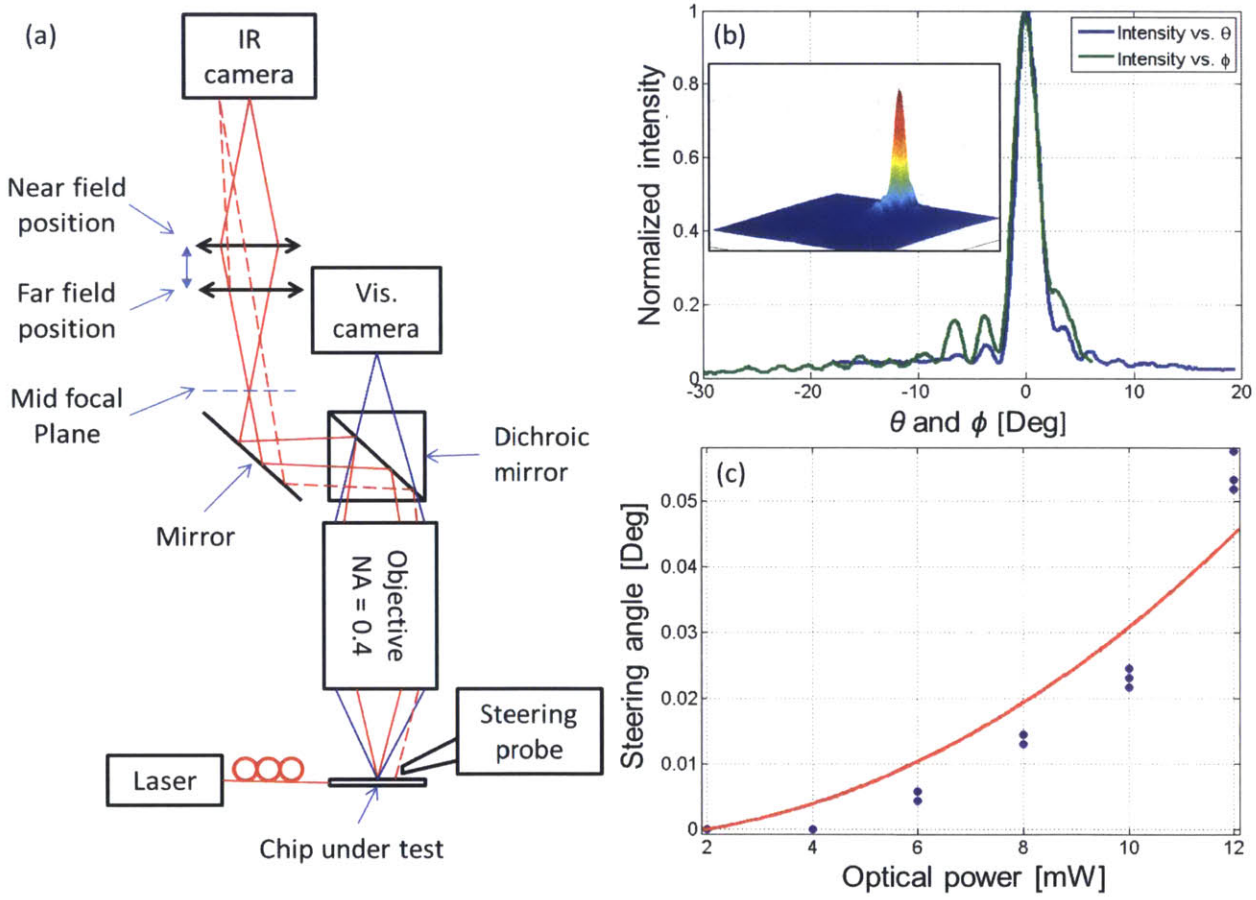

Fig. 5.9 Experimental setup and beam analyzing: (a) A drawing of the experimental system with two arms: a, short, visible arm and a, long, bifocal, IR arm with secondary lens which can be displaced to shift between far field and near field IR images. The red lines denote IR radiation and the blue lines a visible radiation. (b) The NPA far field spot: a 3D plot of the spot intensity in the inset and a plot of the intensity cross section on the ϕ and θ directions. (c) A plot of the resulted steering angle due to input optical power. It can be seen that the steering angle is negligible (less than 0.05°) at an optical power of 12mW.

To characterize the steering, a uniform voltage was applied across all of the cascaded phase shifters (no voltage was necessary on any of the phase trimmers) through the electric probe shown in Fig. 5.9(a). Fig. 5.10(a) shows the resulting far field beam, captured with the NIR camera, as it is steered over the whole beam spacing. The lens having NA of 0.32 at wavelength of 1550nm shows an angular radius of only 18.7° and, therefore, cannot show more than one beam at a time. However, it can still clearly be seen that at 11V the next order shows up at the same position where the main beam was at 0V bias, which confirms that a 2π phase shift was achieved.

In order to measure the frequency response of the system, a sinusoidal input steering voltage, with frequencies much higher than the inverse integration time of the NIR camera, was applied. Such an input signal enabled us to see the steering as a steady line where the steering amplitude is indicated by half of the line length. The inset of Fig. 5.10(b) shows example images at 1kHz, 10kHz and 50kHz and how the steering angle reduces with frequency. The normalized frequency response of the array was measured vs. frequency by comparing the steering amplitude with the steering amplitude at low frequencies. Fig. 5.10(b) shows the normalized steering amplitude as a function of steering frequency. The 3dB cutoff operation frequency for continuous steering was found to be ~100kHz and the maximal steering speed up to $5\text{x}10^6$ degree/sec. We attribute the 20% reduction of the 3dB cut-off frequency to the proximity of phase shifters in series which limits the cooling mechanism to a two dimensional plane rather than all directions.

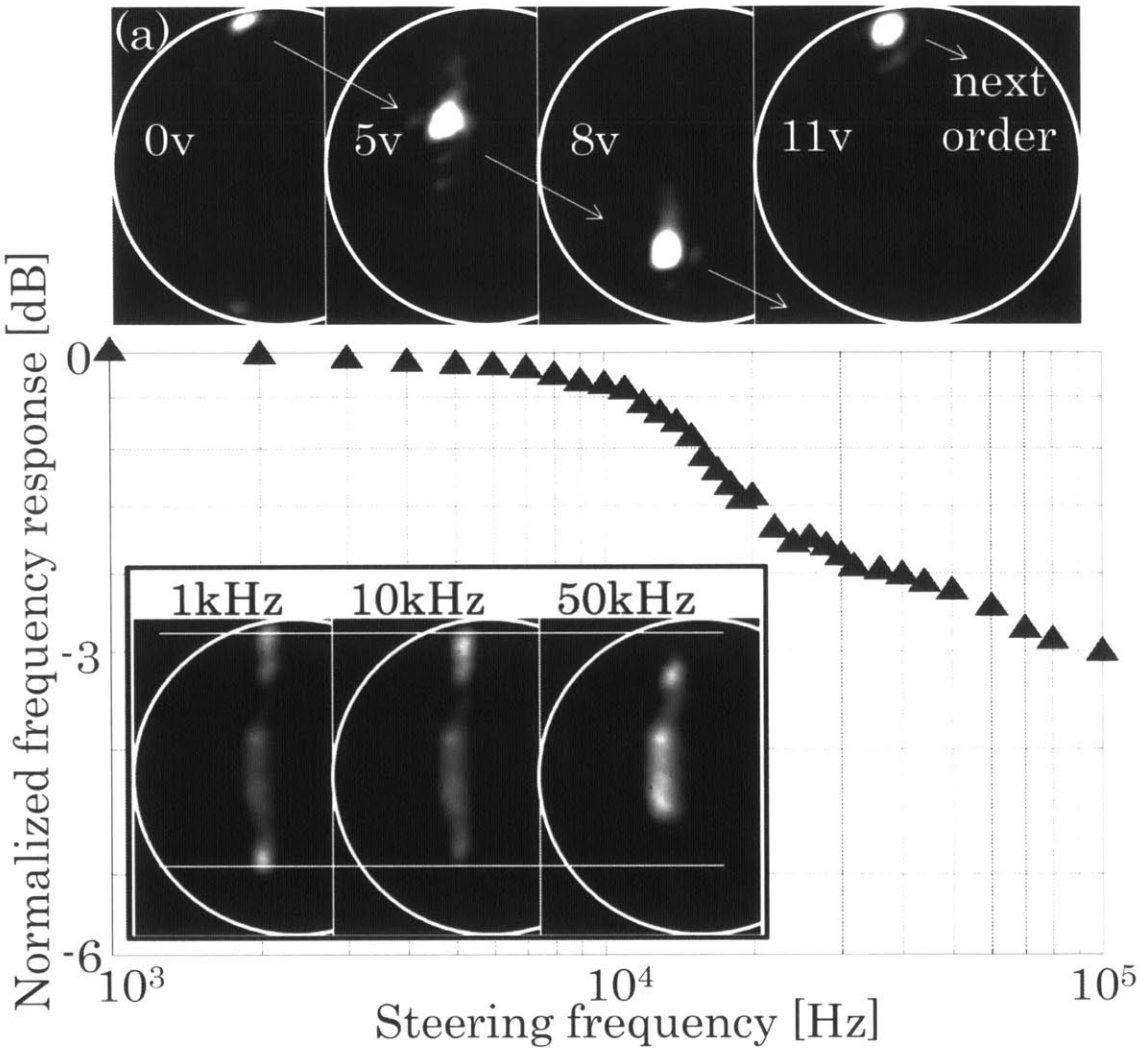

Fig. 5.10 Steering experiment: (a) Far field images of slow steering show steering throughout the whole beam spacing. (b) Normalized frequency response of the NPA showing the 3dB level at ~100kHz with the inset illustrating the method we used to measure that frequency response. It shows actual, high speed, steering images at different frequencies and how the amplitude reduces with frequency. The white circles in the images show the 0.32 numerical aperture of the imaging system (24° in radius).

In conclusion, we demonstrate a high-speed silicon based NPA with, to the best of our knowledge, the widest scanning range (51°) achieved to date. This one-dimensional phased-array provides continuous, high-speed beam steering suitable for lidar applications. In the longitudinal dimension, several arrays can be implemented on the same chip with different grating periods in order to generate several scanning planes. This method of repeating emitters in order to generate 2-D scanning is common in lidar systems (e.g. Velodyne lidar HDL-64E (105)). Nevertheless, (96), (24) suggest longitudinal steering by sweeping the wavelength. This is possible but also points to another method that can be applied; by driving a NPA with a spectral comb, multiple beams can be emitted simultaneously to achieve 2-D scanning. The design can be easily modified for different wavelengths within the 1.2-3.5μm range. More importantly, this NPA was fabricated in a standard 300mm CMOS fabrication facility using a custom Si photonics process. As

such, the device can be cost-effectively mass produced to serve numerous applications including automotive accident avoidance technologies.

5.4 Nanophotonic Lidar

The next step is a nanophotonic lidar demonstration. This includes combining the FMCW ranging with a large NPA to enable both steering and detection of a non-retro-reflecting target without external optics. In order to do so, we need to design our NPA with a larger aperture. For final system resolution requirements of less than 0.5m at 100m range and assuming a diffraction limited system, we need an aperture size of several hundred microns. This large aperture will not allow for many splits and variations on our limited chip area. Therefore, we assess the lateral scale up to be easier due to its coupler based architecture and scale up only the longitudinal dimension at this point. A Si photonic demonstration lidar for short range (~1m) ranging that can work with transmitted power of about 1mW and with a reasonable aperture size, was designed here and preliminary results of the beam shape are shown.

5.4.1 Design

Fig. 5.11(a) shows the architecture of the designed photonic system with its main components. One SSB and two Ge detectors similar to that in the last section were placed in the design for frequency control and balanced detection. The balanced detection is extremely important to eliminate the LO power fluctuations from entering spectral noise to the analyzed signal. 10% and 50% couplers were used to tap a small amount of light out of the emitted beam as a LO, and for beating the received signal with the LO. NPAs were placed as an emitter and a receiver but with some changes compared to the ones from the last section. As seen in Fig. 5.11(b), the direction of the cascaded phase shifting was flipped to reduce the additional length between sequential antennas and to lower aberrations resulting from fabrication fluctuations. In order to demonstrate the large aperture in the longitudinal direction of the antennas, 512μm long antennas were designed with a similar method explained in Section 5.3.2 and shown in Fig. 5.7. Phase shifters were redesigned with larger radii to further reduce bend to waveguide losses. New phase shifter optimal dimensions were set to be 3.0μm on the outer radius, the inner ellipse size was found to be optimal at r_a = 2.5μm with r_b = 2.6μm and the ellipses offset was found to be optimal at Δ_{opt} = 0.9μm. Using this design we achieved 0.5% loss per curve which allows larger number of antennas to be implemented in a cascaded phase shifting manner. We also add a linear cascaded phase shifter which is based on a long, single side, ridge waveguide with contacts on its ridge side and evanescent couplers on the full etch side. This cascaded phase shifter architecture allows coupling to large number of antennas with no bend losses but is also area consuming for the long waveguide section it requires between sequential antennas. Using these components, we drew different emitter NPAs with 22 antennas spaced 2μm and 1.5μm in pitch. The receiver antennas were drawn the same way as their emitters but with pitch

larger by 20% in order to shift the receiver side lobes from the emitter side lobes and avoid range measurements in unwanted directions. For a better working point, and lower loss, the two Mach-Zehnder Modulators (MZM) in the SSB were designed to work in push-pull and depletion mode. As shown in Fig. 5.11(c), while the center probe of each MZM was connected to a RF probe signal pad, the top and bottom rails of each MZM were connected to DC probe pads in order to receive positive and negative rails respectively. The RF ground probe pads were then connected through a metallic comb capacitor, in the two metal layers, to the rails to allow RF ground to reach the MZM. The full design drawing is shown in Fig. 5.11(d). The RF (GSGSG) probes are seen at the bottom left of the image near the input of the device and the DC probe pads with MZM rails, detectors' contacts and steering input signals are seen at the top of the drawing.

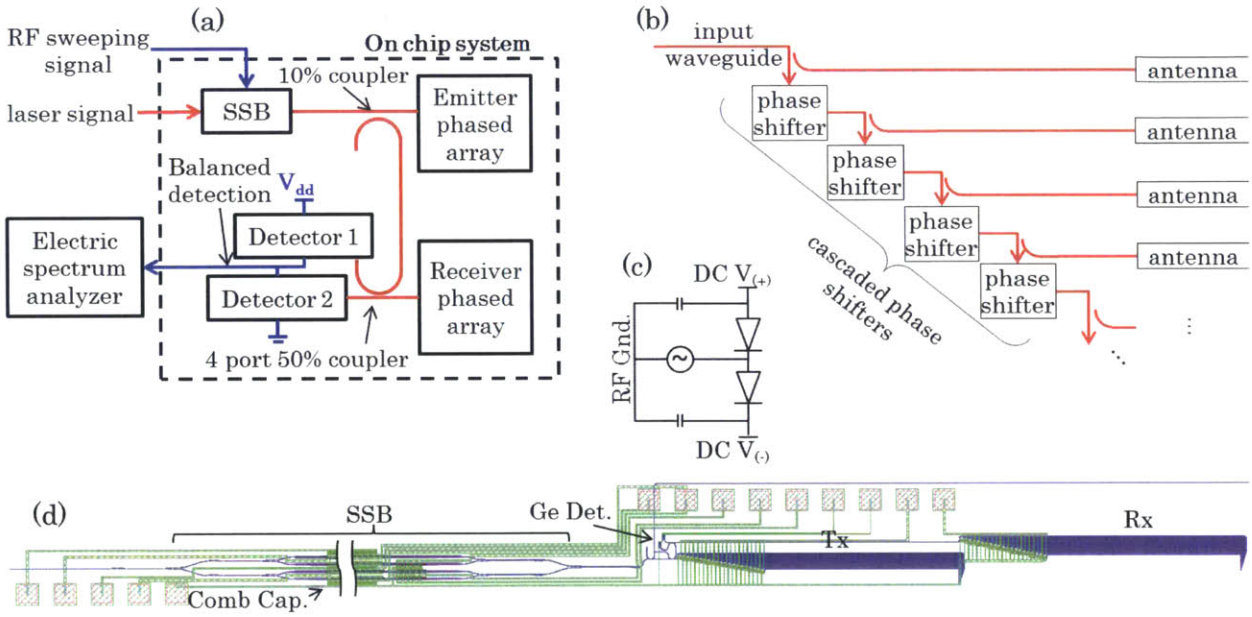

Fig. 5.11 On chip lidar design: (a) On chip components, (b) better cascade phase shifting for less aberration in large arrays, (c) a MZM arm was wired and (d) a drawing of the designed system showing the main parts of it with metal in green and Si in purple. The center of the SSB was taken off the picture for its uniform long pattern. RF Gnd. – RF ground, Comb Cap. – metal comb capacitor, Ge Det. – two balanced detectors, Tx – transmitter and Rx – receiver.

5.4.2 Fabrication and Preliminary Experimental Results

The device was fabricated in the College of Nanoscale Science and Engineering (CNSE) from a Si on insulator (SOI) wafer with 2μm buried oxide (BOX) and 220nm Si layer. This layer was fully etched to form the components and partly etched (110nm deep) to create the gradual increasing strength gratings and for side contacts on the SSB waveguide which was designed as a ridge waveguide. High, $n^+ \sim 10^{20}$ cm^{-3}, and low, $n = 2\times10^{18}$ cm^{-3}, n-type doping levels were applied to form the phase shifting and SSB components, and a high p-type doping, $p^+ \sim 10^{20}$ cm^{-3}, was applied on the Si layer under the Germanium (Ge) detectors. A Ge layer was deposited directly on the p-type Si with gradually increasing dopant levels

to form the p-n junction Ge detector. Two layers of metal with Si contacts and via were placed to allow contact pads to control and measure the device. Temporal issues with the focus of the opto-lithography machine in CNSE produced high losses in the waveguides and disabled us from a lidar demonstration but early results of near field and far field are shown here.

Fig. 5.12(a) shows a 3D plot of the far field intensity and Fig. 5.12(b) shows the cross-sections of intensity in the lateral and longitudinal directions separately. The ripples on the lateral direction are a result of the reflection of the down emission from the bottom of the Si handle. These reflections can be reduced by roughening the bottom of the chip or otherwise canceling its reflection. On the lateral dimension, the expected diffraction limited FWHM of the spot is 1.79° - about the same as the measured far field spot size. On the longitudinal direction, on the other hand, the spot size is 0.34° while the expected diffraction limited spot size from a 512μm antenna is just above 0.15°. While this spot size is about twice the expected size, it is still the smallest known to us produced from a Si photonic antenna. One more issue is seen in the near field. The near field intensity along the antenna is not uniform as designed but instead decays along the antenna direction. Looking at our design again, we attribute both issues stated here to high fabrication sensitivity to our antenna design method. While the method of ridge etching small gratings on the side of the antenna allows for very small perturbations, small exposure differences between the ridge etch and full etch masks or small fluctuations in shallow etch time/depth, can cause small changes in extraction levels of light from the waveguide. This in turn, for a long antenna, accumulates to extract the light from the waveguide before the antenna ends, effectively making a smaller antenna. In addition, these small fluctuations cause aberrations on the emitted light along the antenna since the pitch is no longer set for the fabricated grating strength. In order to correct this, in our next run we designed the antenna with small full etch gratings on the side wall of the waveguide. This full etch grating can be as small as the mask resolution (1nm in our case). While the opto-lithography spot size and minimum feature size are much greater, than this resolution, small displacement in side walls does translate to the waveguide structure. This method should solve the issues stated above, since using the same mask is not affected by exposure fluctuations, and by being a full etch, not sensitive to etch time. Full etched side wall grating antennas can provide accurate, practically infinitesimal, perturbation to be used in long optical antennas.

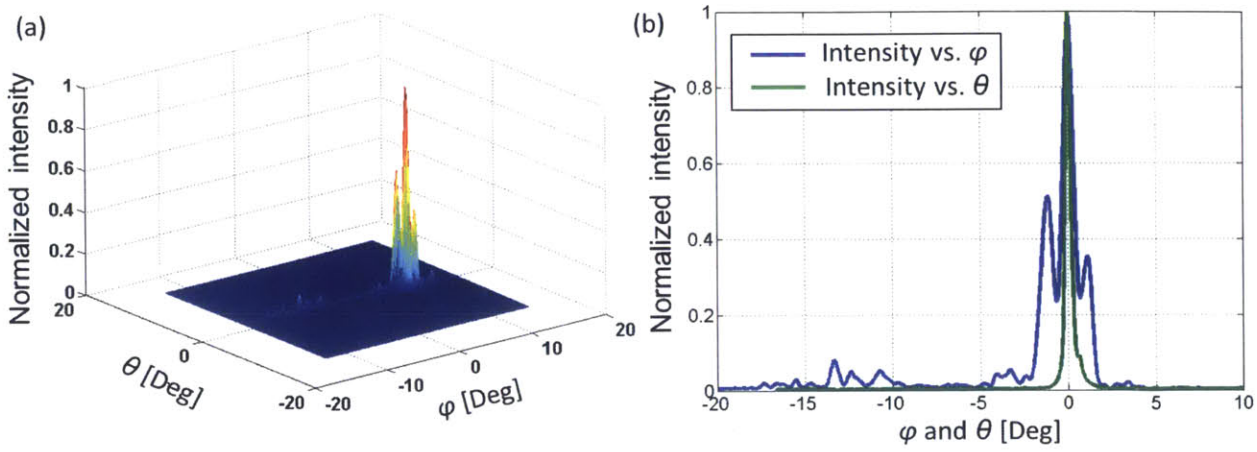

Fig. 5.12 Far field spot analysis of a long NPA: (a) a 3D image showing the two dimensional far field intensity. The far field intensity along the longitudinal, θ, and lateral, φ, direction.

5.4.3 Summary

We have shown a design for an on-chip lidar demo system and its preliminary result. Although some fabrication and antenna issues are still to be solved, this work is a work in progress and important lessons have been learned. In addition, the ranging method of FMCW was demonstrated using some of the components in our design. Future work will include several different levels. On the immediate scale, fabrication issues will be solved and a short range lidar demonstrated is expected. As a second stage, a passive run is planned to test the ability of designing a large diffraction limited phased array and an active run is designed to test multiple receivers as well as other methods of gaining more capabilities from one lidar design. Combining these two abilities will clear the way for demonstrating a photonic lidar for up to tens of meters ranging. An on-chip laser source (87), (88) can also be implemented and the photonic chip can be integrated to a CMOS electronic chip (89) for SSB driving, signal processing and frequency analyzing but these are considered out of the scope for this work. Designed and fabricated right, NPA based lidars will impact many fields in the near future.

6 Summary

Si based Nanophotonic Phased Arrays (NPAs) are indeed strong tool for cost reduction of lidar systems but they can serve in many more applications that benefit from their low cost, high robustness and easy interface with CMOS technology. Here we briefly show two other applications where NPAs can make a large contribution. The first one is in the holographic application – actively tunable NPAs can produce dynamic holographic images. The second is to produce a tunable optical angular momentum beam using a unique architecture of NPA.

6.1 Other Practices for Nanophotonic Phased Arrays

6.1.1 Holographic Displays

Until now, image information has generally been stored and transmitted through the intensity of individual pixels. In contrast, NPAs open up possibilities for imaging as well as projecting. Using a small NPA to replace the conventional pixel (~100μm x 100μm in size), the intensity only information, traditionally emitted from that pixel, can now be replaced with a multi-directional intensity map (Intensity per $\vec{k}$ vector). This ability of phased arrays was demonstrated in (6) and further elaborated in (106) to create a complex intensity pattern in $\vec{k}$ space. The intensity pattern in $\vec{k}$ space can also be called the far field image of the array and can be used to generate a 3D representation (hologram) of any object.

Fig. 6.1(a) shows how a point source can be projected in front of such a screen. A viewer observing the screen from any angle will see a floating point source since the light that reaches the observer eye will always pass though the same point in space. Shifting from a point source to a hologram of an object, we can represent the object by a large number of individual point sources. Then, by tuning each phased array to illuminate all point sources (some pattern in its far field), we create a hologram of the desired object for the observer of the screen. Fig. 6.1(b) shows far field images of 9 pixels, corresponding to their locations on such a screen, designed to create a hologram of a pyramid. It can be seen how each pixel's far field pattern is designed to show the pyramid from a different angle.

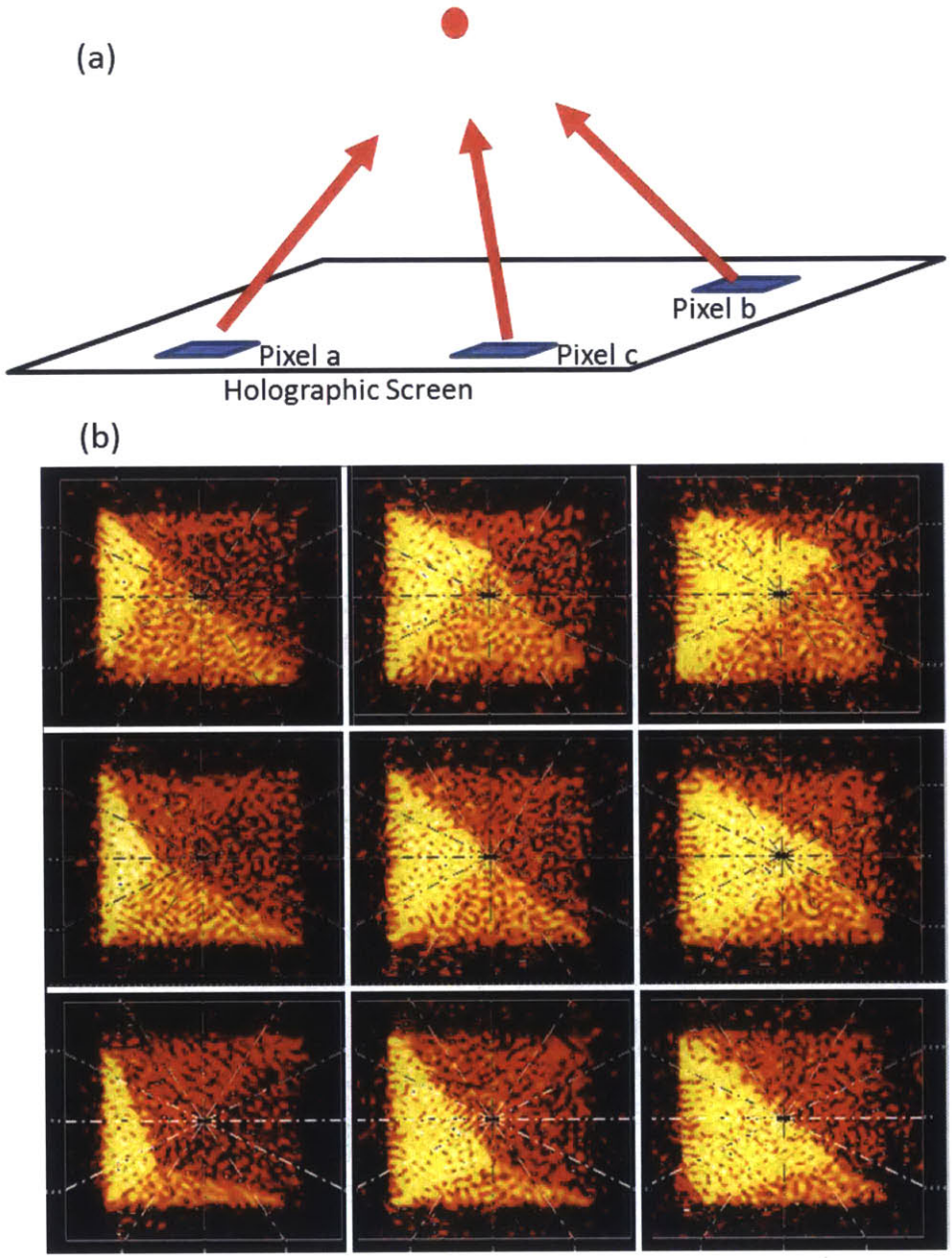

Fig. 6.1 Holographic principle: (a) Pixels in a screen emit light in a single beam each to illuminate one point in space. This point becomes a hologram of a point source floating in space. (b) Nine computed far field images of 32x32 emitter phased array pixels designed to emit a hologram of a pyramid.

In this section we discuss current work being carried out to design a screen of phased arrays as individual pixels in the visible range (λ=635nm) that will produce a hologram in front of or behind the screen. We describe a 4μm pitch unit cell as part of a 2D NPA (with similar power splitting scheme as in Chapter 1 and Fig. 4.1) and how it is used in two separate tasks needed to achieve the aforementioned functionality. The first task is to create a passive screen of 32×32 phased array pixels, each with 32×32 antennas that will produce a hologram demo. For this task we control the phase by small shifts in the position of the unit cell along the row bus waveguide. This task is important for demonstrating the ability

to create a hologram from a set of far field emission patterns. The second task is to demonstrate an active visible phased array, with no more than 16×16 unit cells. This task is important in order to demonstrate visible spectrum phase shifting on a small array that can be drawn with many variations on a small chip area.

Both far field patterns and active phase control were demonstrated at a wavelength of 1550nm (6), nevertheless, designing a phased array for the visible spectrum includes some new challenges. First, the shorter wavelength (on the order of hundreds of nanometers), requires further reduction in the unit cell size. This limits the available area for coupling, phase shifting and emitting the light. Second, the use of Si as a strong waveguiding material is no longer possible due to the high absorption in the visible spectrum. Furthermore, the strong thermo-optic effect in Si which led to a small footprint phase shifter can no longer be used here. In order to address these two issues (space and waveguide material) we combine two approaches. Implementing phase tuning of the emitted light above the optical antenna, takes out a large component from the unit cell area and eliminates the need for a strong phase shifting effect in the waveguide. Doing so allows us to substitute the use of Si waveguide with a Si_3N_4 waveguide which is transparent throughout the entire visible range. Si_3N_4 as a waveguide material was chosen mainly for its compatibility with CMOS fabrication processes and facilities. The active phased array is designed to test several methods of phase shifting. The main methods rely on liquid crystals (LCs) and can be achieved either by direct application of LCs on top of the chip or application of LCs in trenches in the cladding SiO_2 of the chip. When applying LCs on top of the chip, we use the top Aluminum (Al) layer in our platform as bottom separated electrodes per pixel and an Indium Tin Oxide (ITO) electrode deposited on a glass substrate as ground electrode. The Al electrodes are shaped as a rectangular aperture in order to allow transmission of the emitted antenna radiation. As a different option, we use trenches reaching 200nm from the Si_3N_4 layer in our platform to accommodate ~6μm optical path of LC volume. Two metals and via layers are used to apply a horizontal electric field on the LC.

A challenge presented by the use of Si_3N_4 waveguides is the low index contrast between the waveguide $n_c = 2.01$ and its cladding material SiO_2 $n_{cl} = 1.457$ (107). This produces a less confined mode in the waveguide, creates loss in waveguide bends and makes it harder to design short and strong grating antennas. Fig. 6.2(a) shows our unit cell design as part of a 2D 8x8 phased array. It can be seen in this image how we shift the bend section with respect to the straight section in order to better match the straight propagating mode with the curved waveguide mode and reduce losses. In addition, it can be seen how we extend the grating region to the outer side of the bend in order to emit some of the wave lost in the bend. The figure also shows that in order to enhance coupling to free space from the low index contrast Si_3N_4 grating we add small staggered Si arches under the Si_3N_4 gratings. These Si arches do not add extensive loss since their interaction with the light is extremely short and they are staggered with

respect to the Si_3N_4 gratings in order to break symmetries as explained in Section 2.3. In addition, the first Si grating is ridge etched, again, in order to break forward backward symmetry. The test structure consisting of 8x8 antennas was fabricated and tested to produce the preliminary results of near field and far field images shown in Fig. 6.2(b) and (c) respectively. The far field image shows the 9° separation expected from a 4μm pitch phased array and a spot size that is about 1°, the diffraction limit of such array.

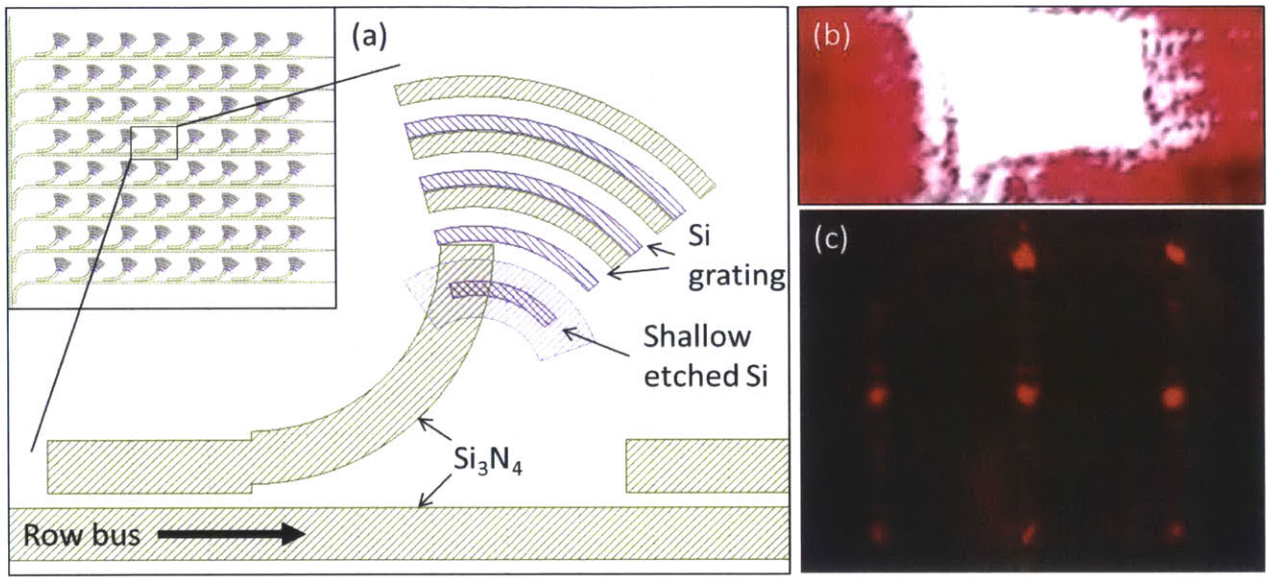

Fig. 6.2 Visible phased array design and preliminary results: (a) a unit cell design as part of the 2D architecture. The use of waveguide shifting before the bend to reduce bend loss, and the use of Si gratings to enhance emission are seen in the picture. (b) Near field and (c) far field images of the phased array, The spots in the far field are 9° apart with widths of ~1° FWHM which is close to the diffraction limit of a 32μm × 32μm phased array.

By comparison with other holographic approaches such as the metasurface antennas (73), the NPA allows separate control over the phase of light emission and on-chip single-point excitation of the nanophotonic antennas, enabling truly arbitrary holograms to be generated entirely on-chip for the first time. We show here a design that, together with the right phase shifting mechanism (e.g. LCs), can produce a true holographic image.

6.1.2 Continuously Tunable Optical Angular Momentum

An optical vortex, a beam with non-zero optical orbital angular momentum (OAM), is a beam with phase that is changing with an azimuthal dependence $E(\varphi) \propto e^{-jl\varphi}$ where l is the angular momentum quantum number and φ is the azimuth angle around the center of the beam. It is important to note here that l is not limited to be an integer (108). OAM is used in a variety of fields from communication (109), (110) to optical quantum information (111). Some applications, like optical forces for atom and molecule manipulation (112), requires continuously tunable optical angular momentum (i.e. non-integer l number). We propose and demonstrate here an architecture of an on-chip NPA that produces a free space tunable

angular momentum beam. This system, being so miniature and cost effective in mass production, opens a vast amount of opportunities for on-chip laboratories and cost reduction of complex communication and encoding systems. This work was published in detail in (20) and is overviewed here only as an of example of one more application available using NPAs

In order to design this tunable angular momentum NPA, we arrange the array of antennas in a circular manner and feed them using a cascade phase shifting bus waveguide on the outer circumference of the device. Fig. 6.3(a) and (b) shows the architecture of the device and the design of a single unit cell respectively. The coupler and phase shifter components, though not exactly the same as described in Chapter 1, are built on the same principle and do not have any major difference from the described above. The antenna is exactly the same as been used in Chapter 1.

Being a ring of N antennas oriented in different direction, φ_n, around the circle, the far field intensity and phase of this NPA is not completely intuitive. Assuming the far field of a single antenna is linearly polarized in the lateral direction, the far field of the n^{th} antenna is

$$\boldsymbol{E}_n(r,\theta,\varphi) = \hat{\varphi}_n E_0(r,\theta,\varphi-\varphi_n) \qquad \text{Eq. 6.1}$$

where r and θ are the radial and polar coordinates, the polarization of each antenna is changing with n and pointing to the $\hat{\varphi}_n$ direction and $E_0(t,\theta,\varphi)$ is the field intensity scalar function in far field of a non-rotated antenna. From Eq. C.2, the total array radiation now is

$$\begin{aligned}\boldsymbol{E}(r) &= \sum_{n=1}^{N} \boldsymbol{E}_n(r)\exp\left(-j(k\hat{r}\cdot r_n+\phi_n)\right)\\ &= \sum_{n=1}^{N} \boldsymbol{E}_n(r)\exp\left(-j(ksin(\theta)\cos(\varphi-\varphi_n)+n\Delta\phi)\right).\end{aligned} \qquad \text{Eq. 6.2}$$

Compared to Eq. C.2, the single antenna field was inserted in to the sum since every antenna has a different far field contribution and a_n was omitted since we can set $a_n = 1$ for our case. $k = 2\pi/\lambda$ is the wave number, and the n^{th} antenna phase is $\phi_n = n\Delta\phi$ where $\Delta\phi$ is the phase difference between adjacent antennas controlled by the phase shifters. Since the antennas are equally distributed around the circle, $\varphi_n = -2\pi n/N$, where the (-) sign is for the counter-clock-wise order of the antennas. It is easy to see that $\Delta\phi = -2\pi l/N$ which leads to

$$\boldsymbol{E}(r) = \sum_{n=1}^{N} \boldsymbol{E}_n(r)\exp\left(-j(ksin(\theta)\cos(\varphi-\varphi_n)-\varphi_n l)\right). \qquad \text{Eq. 6.3}$$

Since the polarization of each $\boldsymbol{E}_n$ is different, and at $\theta \neq 0$ each antenna contribute with different phase, the far field, the far field of this array is a circular polarized with different phases depending on the φ

position. This equation gives the theoretical helical far field of the array and is used later in the text to simulate the array response and compare it with our experimental results.

The device was fabricated in the College of Nanoscale Science and Engineering on a Si on insulator (SOI) wafer with 2μm buried oxide (BOX) and 220nm Si layer which was fully and partially etched to form waveguide and antennas. High and low n-type doping levels of ~10^{20} cm^{-3} and 2×10^{18} cm^{-3} were applied to form the phase shifting Si leads and resistive sections respectively. Two layers of metal with Si contacts and vias were placed to allow contact pads to control the heaters. As seen in Fig. 6.3(a), all phase shifters were operated with a single voltage which allows a simple operation. Fig. 6.3(c)-(e) show an SEM of the device, the antenna section and a single phase shifter respectively after dry etching and removing the oxide cladding.

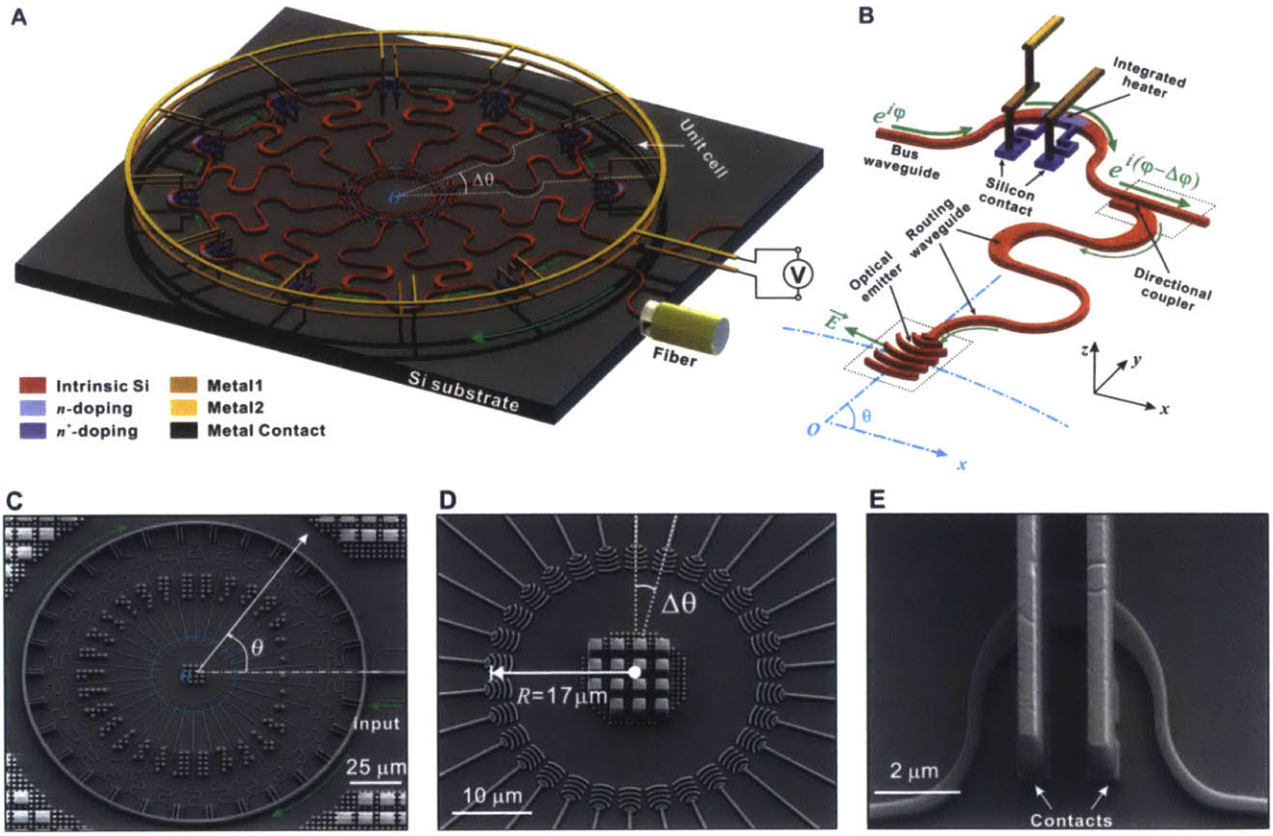

Fig. 6.3 The structure of the continuously tunable OAM generator: (A) A schematic of the proposed continuously tunable integrated OAM generator, consisting of N unit cells placed concentrically along a silicon bus waveguide that forms an open circle. (B) A schematic of an individual unit cell, consisting of a directional coupler, a directly integrated thermo-optic phase shifter and a grating-based optical emitter. Scanning-electron micrographs of (C) the fabricated OAM generator using a CMOS-compatible silicon photonic process, (D) a close-up view of N = 30 optical emitters in the center of the device, and (E) a close-up view of the integrated thermo-optic phase shifter. Figure courtesy of (20)

In order to test the light emitting from the OAM generator we use the system shown in Fig. 6.4. Laser power was split to two fiber arms with polarization and power control on each arm. The first arm (90% of the power) was used to feed the chip while the second arm (10% of the power) was used to create a

reference beam to interfere the OAM beam with. It is important to note here that an OAM beam intensity alone is ring shaped and does not give the complete angular momentum information in its helical shape without looking at its phase information. This can be extracted by interfering the OAM beam with a circular polarized reference beam to create the line fringes of constructive and destructive interference. Preferably, the reference beam's phase front is not planar but spherical to give create the spherical interference lines of helical shape that differs between its positive and negative angular momentum numbers. The inset in Fig. 6.4 shows how the OAM helical beam interferes with a spherical phase front to create the spherical shape of constructive and destructive interference. Thus, for the reference beam, no fiber collimator was used and the fiber end was used as a point source to create the spherical phase front. The optics on the OAM beam was set to project the far field image of the array on the near infrared (NIR) camera and a 50/50 beam splitter was used to combine the reference beam with the OAM beam before projecting onto the camera.

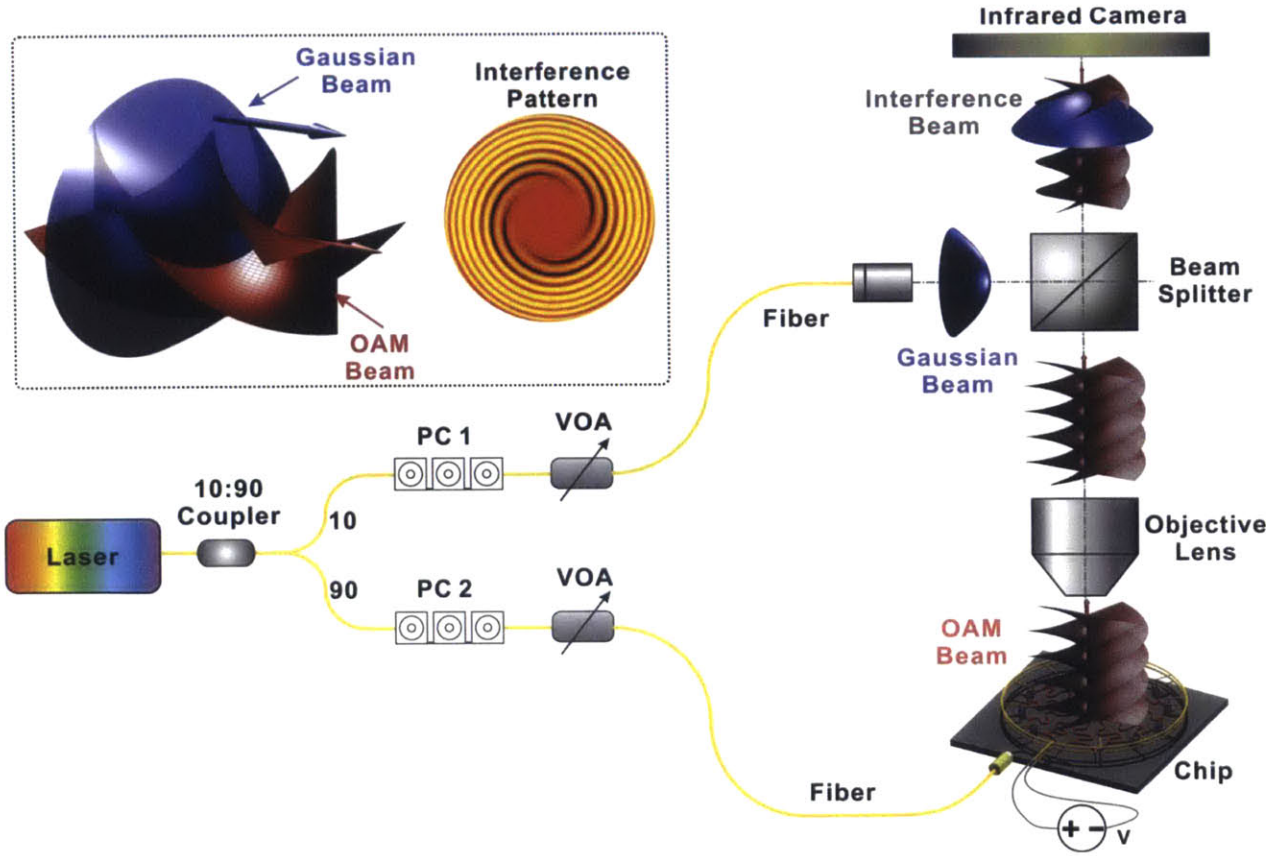

Fig. 6.4 Experimental setup to identify the OAM state of the synthesized beam: The inset illustrates the interference of the OAM beam with a spherical phase front reference beam to reveal the helical phase front of the OAM beam from which the l-value (positive and negative) can be identified. PC: Polarization Controller, VOA: Variable Optical Attenuator. Figure courtesyof (20) supplementary material.

For testing the device, different electrical powers were applied on the phase shifters to create different OAM l numbers. The NIR images were then captured and are plotted in Fig. 6.5(a) against simulated

images calculated using Eq. 6.3. One can clearly see the agreement between the captured and simulated images. Also, by counting the numbers of spirals in each image, the different OAM states, including the half states, of the captured beams are clearly seen up to $l = \pm 4$. Plotting the NPA's electrical power vs. OAM state reveals the phase linearity per power of our phase shifter design and agrees with the linear characteristic of the device for OAM state per added phase. Moreover, the non-resonant characteristic of this NPA and its electric control OAM state releases the need for wavelength control presented in (113) and allow for a broadband OAM generator.

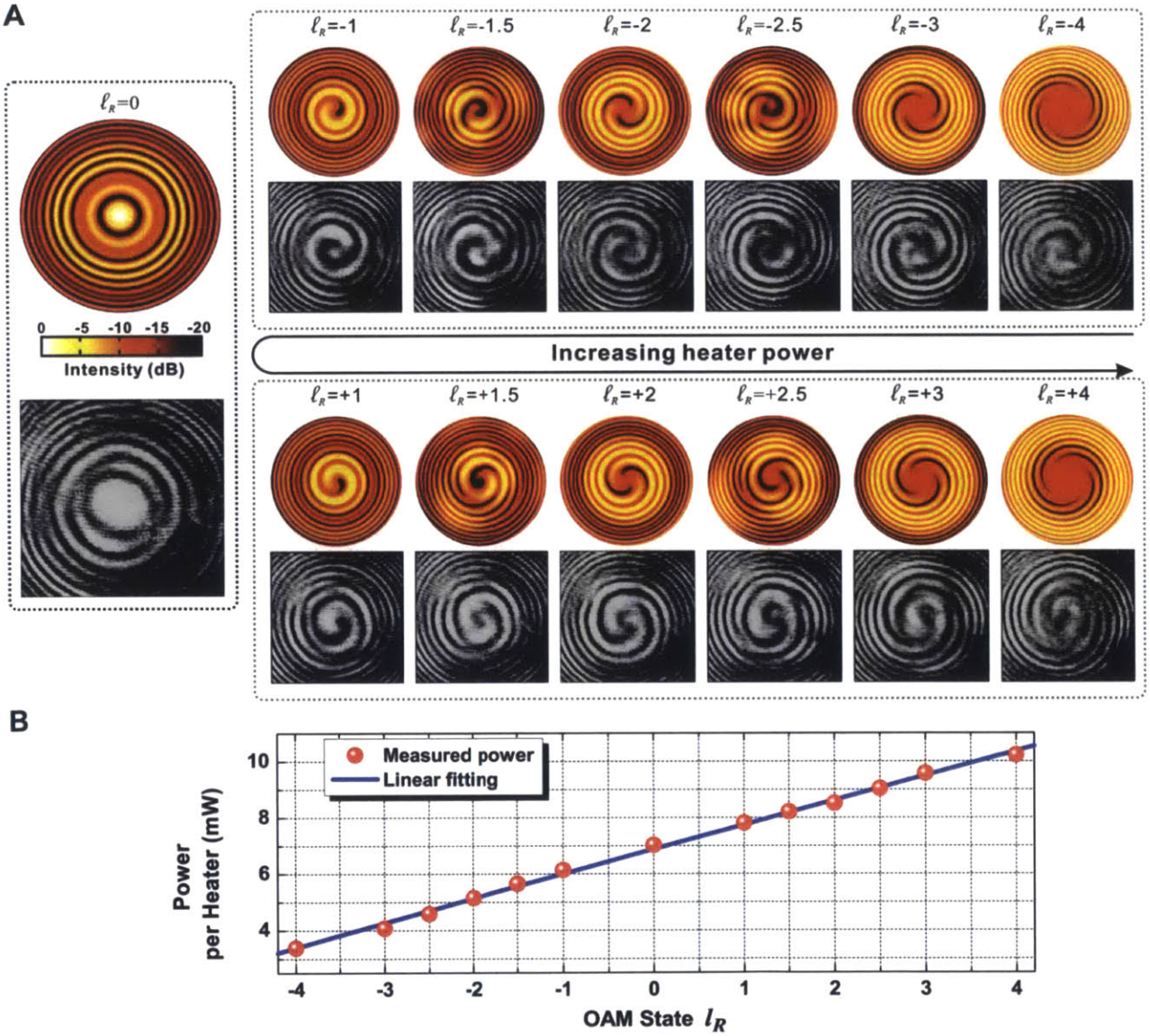

Fig. 6.5 Demonstration of the continuously tunable OAM state: (A) The OAM state of the generated vortex beam can be electrically tuned by the voltage applied on the thermo-optic phase shifter. OAM states from -4 to +4 revealed by the number of arms and the chirality of the spiral interference pattern with a co-propagating, circular polarized, beam. The non-integer OAM states (±1.5, ±2.5) have also been demonstrated, showing the beam evolution in between two integer OAM states. A good agreement between simulation (top row) and measurement (bottom row) has been observed. (B) The measured power applied on the phase shifter to achieve different OAM states, which increases linearly as the OAM state is continuously tuned from -4 to +4. Figure courtesy of (20).

Our device, a tunable OAM generator, and through reciprocity a tunable OAM detector, enables continuous and wavelength-independent tuning of the OAM state. Already, OAM is impacting a wide range of applications, and even greater opportunities lie in the promise to integrate our device with other silicon photonic components and functionalities as well as electronics to realize chip-scale broadband tunable OAM systems. The device opens up new possibilities to generate complex and reconfigurable optical beam forms using chip-size, silicon photonic circuits.

6.2 Parting Thoughts and Future Work

It is clear now that NPAs are expected to create a large impact on number of fields. The ability to produce a free space arbitrary beam shape will enable new methods in communication, holography, and imaging. The ability to control a beam's angular momentum has the potential to affect information systems, communication and nano-synthesis of materials or biological substances. This large number of applications and fields where NPAs can make an impact was produced in only several years since first devices were demonstrated, and the field is still in its infancy. The largest expected impact of these devices is not in its new capabilities but the ability to produce a robust, chip scale, system at an affordable price. Being CMOS compatible, NPAs and the systems that they will enable are going to be cost effective to implement in massive numbers.

Part of the systems in which the cost reduction plays a crucial role are lidars. The ability to measure distances up to a hundred meters or more with sub-meter resolution and independence of day light or background is a game changer in autonomous systems and self-driving cars specifically. Moreover, the number of applications that can benefit from such low cost range mapping range from cellular sensors, through robotic vacuum cleaners to console games to low end security systems and many more.

When designing a compact lidar system, the limitation on the aperture size plays a crucial limit on power collection and SNR budget which strongly limits range and performance of the system. The natural solution for such a limitation is the use of coherent detection which enables low power signal transmission, shot noise limited signal detection with, low cost, reasonable dark current detectors and almost complete immunity to background light. Si based nanophotonics is the natural platform for such systems. Its single mode waveguide characteristic supports, and is necessary, for coherent detection; its integrated Ge detectors are suited for the required signal detection. Furthermore, its ability to integrate with CMOS electronics allow for more data analysis on chip and, maybe most important, its ability to steer the transmitter and receiver beams release the need of external, expensive, mechano-optics. Si based lidars incorporating NPAs are the natural solution for this system and will create a large impact in the coming years.

Still, some future work needs to be done and some accomplishments need to be demonstrated before such systems can be manufactured. First a lidar system employing a NPA needs to be demonstrated. After this step, first systems will probably start to materialize, but more advantages are yet to come. Flip chip integration of the photonic chip with an electronic chip will enable on chip data analyzing, driving and laser integration on the photonic chip will allow for easy packaging with a small laser diode optically driving the device. Our group is working on both these tasks, as well as other methods to improve the lidar system, and we are confident that such results are near. Low cost, chip scale, Si based lidars incorporating NPAs are soon to be presented.

Appendix: Theoretical Design and Analysis Methods

In order to designs and analyze our components (nanoantennas, couplers and phase shifters), two methods were used, analytical and numerical. The analytical method is Coupled Mode Theory (CMT) which was used for developing intuition, defining physical criteria to evaluate the various designs and understanding the general way a component is working. For exact design parameter choice and evaluation of each component (efficiency, bandwidth, etc.) a numerical method of Finite Difference Time Domain (FDTD) was used. For the system design of Nanophotonic Phased Arrays (NPAs) we used the phased array theory. In this chapter we describe the three methods in more details. We start with coupled mode theory in Appendix A , shift to a short description of the 3D FDTD method in Appendix A , and finish with phased array theory in Appendix A .

Appendix A Coupled Mode Theory (CMT)

Coupled mode theory, in optics and photonics, is a strong tool that helps understand linear effects of coupling between optical modes of different structures placed in proximity. In most cases given in the literature, this theory is described *in space* (114), (115). The optical modes are propagating modes with a 2D field distribution and third dimension (e.g. z) dependence of $\exp(-j\beta z)$. In the same way, the waveguide supporting the modes and the perturbation on this waveguide are assumed to be constant in z. The coupling mode theory in space, then, looks at the mode evolution along this third dimension (z axis). Nevertheless, the way to use coupling mode theory for tree-dimensional resonators is by looking at it *in time* (29), (61), (62), where the optical modes are defined in 3D and the evolution is looked at in time. In this section we will describe coupled mode theory in time between *bound* resonators (i.e. resonators that their mode is confined in a finite space). Then we explain how to treat *unbound* (radiating) resonators and waveguides, show how to calculate their coupling coefficient(s) and develop the case where the coupling is between a power source (unbound) and a bound resonator with some drop (e.g. drop waveguide). Chapters in this work, where different formulations of coupled modes theory were used, describe the difference inside.

Starting from the formulation of (61), (62), in a more general form, we assume N number of bound resonators with proximity in space such that each resonator weakly perturbs the field of the others, and, for simplicity, we assume no coupling to other modes (i.e. coupling only between the N specified resonators' modes). Although in this situation the supermodes of the system may be totally different, one can still look at the separate independent modes and add a slow amplitude evolution of these modes while

the energy bounces between them. We then define a coupling coefficient κ_{ik} and write the coupling's first order differential equation:

$$\frac{da_i}{dt} = \left(j\omega_i - \frac{1}{\tau_i}\right) a_i - j \sum\nolimits_{k \neq i} \kappa_{ik} a_k, \qquad \text{Eq. A.1}$$

where a_i, ω_i and τ_i are the amplitude, resonance frequency and decay time of the i^{th} resonator respectively and κ_{ik} is the coupling coefficient from the k^{th} resonator to the i^{th} one. The $-j$ in front of the sum is arbitrary and has been chosen for consistency with the CMT in space (115). $|a_i|^2$ is normalized to energy amplitude in each resonator. The decay time τ_i of each resonator can be due to radiation (τ_r), ohmic losses (τ_o) or coupling to the other resonators (τ_e), and is summed this way:

$$\frac{1}{\tau} = \frac{1}{\tau_r} + \frac{1}{\tau_o} + \frac{1}{\tau_e}. \qquad \text{Eq. A.2}$$

We can write Eq. A.1 in a matrix form

$$\frac{d}{dt}\bar{a} = j\mathrm{M}\bar{a}, \qquad \text{Eq. A.3}$$

where

$$\mathrm{M} = \begin{pmatrix} \left(\omega_1 + j\frac{1}{\tau_1}\right) & \cdots & -\kappa_{1N} \\ \vdots & \ddots & \vdots \\ -\kappa_{N1} & \cdots & \left(\omega_N + j\frac{1}{\tau_N}\right) \end{pmatrix}. \qquad \text{Eq. A.4}$$

Then, assuming the vector $\bar{a}$ dependence in time goes like $\exp(j\omega t)$ we solve to find the eigenvalues $\left(j\omega - \frac{1}{\tau}\right)$ and eigenvectors $\bar{a}$ of the whole system. We can then use these eigenvectors and eigenvalues to evaluate how a system with known starting conditions, spanned by the set of eigenvectors, will evolve in time.

In cases when an unbound resonator is involved, acting like a port to the system (e.g. waveguide or radiating resonator), a_i is substituted with s_i which is the mode amplitude normalized to power, and, for cross coupling between bound and unbound resonators, κ is substituted with μ (61). Because s_i is normalized to power, the time derivative on s_i is removed, and the mixed equations for one bound and one unbound resonators are (61)

$$\frac{da}{dt} = \left(j\omega_0 - \frac{1}{\tau}\right) a - j\mu_{as} s_{in}, \qquad \text{Eq. A.5}$$

$$\Delta s \equiv s_{out} - s_{in} = -j\mu_{sa} a. \qquad \text{Eq. A.6}$$

where s_{in} is defined only for a waveguide with an input port. For a radiating resonator $s_{in} = 0$. It is important to note here that while κ has units of $[1/sec]$, μ has units of $[1/\sqrt{sec}]$ in order to compensate for the difference in the units of a $[\sqrt{Joule}]$ and s $[\sqrt{Watt}]$.

In order to calculate the actual value of the coupling coefficient, given a specific layout of two resonators, we look at the part of the radiation caused by the perturbation on one resonator and coupled into the mode of the second resonator. Following (62) we define each mode e_i in space as the electric field of that mode with no perturbations existing around it. We can normalize this field either to energy for the case of a bound resonator with losses

$$1 = \sqrt{\int \epsilon |e_i|^2 dv} \qquad \text{Eq. A.7}$$

where the integration is over all space. Alternatively, as discussed above, we can normalize to power in the case of a waveguide or radiating resonator

$$1 = \sqrt{\int \left(e_i \times h_i^*\right) \cdot da} \qquad \text{Eq. A.8}$$

where the integration is across one port of the system. I.e. over the envelope of the resonator for antenna that is exited from the center (no input port), or, on a cross section in the case of a waveguide (both input and output ports). This way we can define the actual field distribution of each mode as $a_i e_i$ or $s_i e_i$ with $|a|^2$ and $|s|^2$ representing the energy and power respectively. Following (62) we look at the case of two bound resonators, with no loss, and focus at the power exchange between them

$$\frac{d|a_1|^2}{dt} = -j(\kappa_{12} a_1^* a_2 - \kappa_{12}^* a_1 a_2^*). \qquad \text{Eq. A.9}$$

This power can also be presented as the displacement current P caused by mode number 2 in the presence of, $\delta\epsilon_1$, the perturbation caused by resonator 1

$$j\omega P = j\omega \delta\epsilon_1 a_2 e_2 \qquad \text{Eq. A.10}$$

and radiate into mode number 1

$$\frac{d|a_1|^2}{dt} = \frac{1}{4}\int (j\omega P \cdot a_1^* e_1^* + c.c)dv = \frac{1}{4} j\omega a_2 a_1^* \int (\delta\epsilon_1 e_2 \cdot e_1^*)dv + c.c. \; . \qquad \text{Eq. A.11}$$

Comparing Eq. A.9 with Eq. A.11 we see that

$$\kappa_{12} = -\frac{1}{4}\omega \int (\delta\epsilon_1 e_1^* \cdot e_2)dv. \qquad \text{Eq. A.12}$$

In the case where the fields e_i were not normalized, the right equation for κ is

$$\kappa_{12} = -\frac{\frac{1}{4}\omega \int (\delta\epsilon_1 e_1^* \cdot e_2)dv}{\sqrt{\int |e_2|^2 dv \int |e_1|^2 dv}}. \qquad \text{Eq. A.13}$$

For the case of a waveguide or a radiating resonator, μ is found to be the same but with the corresponding normalization.

Considering only two resonators with no loss and conserving the total energy we can use Eq. A.1 to write

$$0 = \frac{d}{dt}(|a_1|^2 + |a_2|^2) = -j(\kappa_{12}a_1^*a_2 - \kappa_{12}^*a_1a_2^* + \kappa_{21}a_2^*a_1 - \kappa_{21}^*a_2a_1^*). \quad \text{Eq. A.14}$$

Since a_1 and a_2 are arbitrary, we can choose values such that $a_1^*a_2 = j$ so $Re(\kappa_{12}) = Re(\kappa_{21})$ or $a_1^*a_2 = 1$ so $Im(\kappa_{12}) = Im(\kappa_{21})$. Hence, $\kappa_{12} = \kappa_{21} \equiv \kappa$ or in the more general case M is symmetric so $\kappa_{ik} = \kappa_{ki}$.

Shifting back to the case depicted in (61) with a waveguide feeding a resonator, we can write Eq. A.5 for a resonator, a, with resonance frequency ω_0, perturbed by a waveguide source s_{in}

$$\frac{da}{dt} = \left(j\omega_0 - \frac{1}{\tau}\right)a - j\mu_{as}s_{in}, \quad \text{Eq. A.15}$$

and the waveguide mode leaving the perturbation region is

$$s_{out} = s_{in} - j\mu_{sa}a. \quad \text{Eq. A.16}$$

Using the same procedure as in Eq. A.14 we write the energy balance equation assuming no loss or radiation from the resonator ($1/\tau_r = 1/\tau_o = 0 \implies \tau = \tau_e$) and substituting Eq. A.16

$$\begin{aligned} 0 = &\frac{d|a|^2}{dt} + |s_{out}|^2 - |s_{in}|^2 = \\ &-j(\mu_{sa}as_{in}^* - \mu_{sa}^*a^*s_{in} + \mu_{as}s_{in}a^* - \mu_{as}^*s_{in}^*a) + |\mu_{sa}a|^2 - \frac{2}{\tau_e}|a|^2. \end{aligned} \quad \text{Eq. A.17}$$

By zeroing s_{in} it is clear that $|\mu_{sa}|^2 = 2/\tau_e$, and by applying $a^*s_{in} = j$ and $a^*s_{in} = 1$ it is easy to see that $\mu_{sa} = \mu_{as} \equiv \mu$.

In cases where a frequency other than the resonator resonance frequency is applied ($s_{in} = s_0e^{j\omega t}$) from the perturbation source, the response of the resonator can be found by looking at the steady state ($a = a_0e^{j\omega t}$) solution of Eq. A.15:

$$a = -\frac{j\mu s_{in}}{j(\omega - \omega_0) + \frac{1}{\tau}}. \quad \text{Eq. A.18}$$

The total power being radiated from the resonator is then

$$\frac{2}{\tau_r}|a|^2 = \frac{4/\tau_e\tau_r}{(\omega - \omega_0)^2 + \frac{1}{\tau^2}}|s_{in}|^2. \quad \text{Eq. A.19}$$

Therefore, in order to maximize the power delivery neglecting losses, we find the conditions $\omega = \omega_0$ and $\tau_e = \tau_r = 2\tau$. These conditions are generally referred to as frequency matching and load matching respectively. Substituting these conditions back in Eq. A.19, show that 100% of the energy is extracted from the waveguide and distributed by the resonator. Still, the load matching condition is sometimes impossible to achieve. In cases where the resonator is coupled to the waveguide in both directions, for example, there are two equal coupling mechanisms, $1/\tau_e$, so that the second condition (load matching) cannot be met. In this case, the maximum radiated power is only 50% of the source power and is achieved with $\tau_e = 2\tau_r$.

CMT assumes shape invariance of the modes and drops second order terms, making it quantitatively accurate only with weakly coupled modes; however, coupled mode theory provides useful insight even when modes are strongly coupled. In fact, we define parameters like decay time and coupling coefficients to evaluate our components, use design methods measuring decay times to understand our coupling conditions and use eigenmodes calculated through CMT. However, CMT is still approximate; therefore to ensure accuracy in design, we rely on three-dimensional full field simulations for all quantitative results.

Appendix B Finite Difference Time Domain (FDTD)

To evaluate the performance of designs of the different components in this work Finite Difference Time Domain (FDTD) simulations are used. We briefly describe here this method, more details can be found in (80). This chapter does not intend to show all the details required to create a 3D FDTD simulation. Instead, we will show the math related to 1D propagation and discuss the discretization of the field in time and space. By doing so, we intend to bring the general understanding of this method and the way it works.

Generally speaking, FDTD takes the material properties (e.g. permittivity), structured in a defined volume, with an electromagnetic source, and propagates the field in time using Faraday's Law and Ampere's Law

$$\frac{d(\mu \boldsymbol{H})}{dt} = -\nabla \times \boldsymbol{E}$$
$$\frac{d(\epsilon \boldsymbol{E})}{dt} = (\nabla \times \boldsymbol{H} - \boldsymbol{J}) \qquad \text{Eq. B.1}$$

where μ and ϵ are defined as functions of space and defines the structure of the domain. An initial field distribution in the volume of the simulation can be defined but, in most cases, it is zero. A 2D source (or several 2D sources) is commonly used to mimic an input power source. During the simulation, 2D field distributions at prespecified planes can be kept for later reference. More importantly, at every step of the simulation, time Fourier integrals of the fields are summed on predefined planes. These Fourier transforms allow us to apply a short pulse at the source, carrying a broad spectrum, and then separate at these planes to calculate the different frequency responses of the system. Being a time domain simulation, the fields, as measurable physical parameters, are defined as real numbers.

The time domain characteristic of the FDTD method allows it to take into account any measurable effect, even nonlinear ones. By specifying a real measurable characteristic of the media (e.g. polarization, electrical current or magnetic momentum) and mathematically relate it to the physics of the simulation, one can add the physical effect into the simulation. For metallic structures in this work, the Drude model was added to accommodate losses, skin effects and, in general, the imaginary part of the permittivity of metals. The Drude model is often known for its permittivity solution in the frequency domain

$$\epsilon(\omega) = \epsilon_0 \left[1 - \frac{\omega_p^2}{\omega^2 - j\omega\gamma}\right] \qquad \text{Eq. B.2}$$

where ϵ_0 is the high frequency permittivity, $\omega_p = \sqrt{Nq^2/m_e\epsilon_0}$ is the plasma frequency and $\gamma = q^2N/m_e\sigma$ is the damping coefficient caused by current resistance in the metal. This equation is originates from the kinetic equation of electrons under an optical electric field

$$q\boldsymbol{E} = m\left[\frac{d^2\vec{r}}{dt} + \gamma\frac{d\vec{r}}{dt}\right]. \qquad \text{Eq. B.3}$$

By integrating this equation once, we get the differential equation for the current in the metallic media

$$\frac{d\boldsymbol{J}}{dt} = \omega_p^2\int_0^t \epsilon_0\boldsymbol{E}(\tau)d\tau - \gamma\boldsymbol{J}\,. \qquad \text{Eq. B.4}$$

The current contributes to the electric field through Ampere's Law

$$\frac{d\boldsymbol{E}}{dt} = \frac{1}{\epsilon}(\nabla\times\boldsymbol{H} - \boldsymbol{J})\,. \qquad \text{Eq. B.5}$$

We bring here one example of how the FDTD simulation can accommodate extended physical properties like metallic media. In other cases, lossy dielectrics (116), (117) or other non-isotropic media (118) were implemented successfully.

Starting with the Maxwell's equations for static dielectric media (i.e. no currents and static μ and ϵ) we write them in discrete, one dimensional, space and time,

$$\begin{aligned}
\frac{\boldsymbol{H}_y\left(x,t+\frac{\Delta t}{2}\right)-\boldsymbol{H}_y\left(x,t-\frac{\Delta t}{2}\right)}{\Delta t} &= \frac{1}{\mu}\frac{\boldsymbol{E}_z\left(x+\frac{\Delta x}{2},t\right)-\boldsymbol{E}_z\left(x-\frac{\Delta x}{2},t\right)}{\Delta x}\\
\frac{\boldsymbol{H}_z\left(x,t+\frac{\Delta t}{2}\right)-\boldsymbol{H}_z\left(x,t-\frac{\Delta t}{2}\right)}{\Delta t} &= -\frac{1}{\mu}\frac{\boldsymbol{E}_y\left(x+\frac{\Delta x}{2},t\right)-\boldsymbol{E}_y\left(x-\frac{\Delta x}{2},t\right)}{\Delta x}\\
\frac{\boldsymbol{E}_y\left(x,t+\frac{\Delta t}{2}\right)-\boldsymbol{E}_y\left(x,t-\frac{\Delta t}{2}\right)}{\Delta t} &= -\frac{1}{\epsilon}\frac{\boldsymbol{H}_z\left(x+\frac{\Delta x}{2},t\right)-\boldsymbol{H}_z\left(x-\frac{\Delta x}{2},t\right)}{\Delta x}\\
\frac{\boldsymbol{E}_z\left(x,t+\frac{\Delta t}{2}\right)-\boldsymbol{E}_z\left(x,t-\frac{\Delta t}{2}\right)}{\Delta t} &= \frac{1}{\epsilon}\frac{\boldsymbol{H}_y\left(x+\frac{\Delta x}{2},t\right)-\boldsymbol{H}_y\left(x-\frac{\Delta x}{2},t\right)}{\Delta x}.
\end{aligned} \qquad \text{Eq. B.6}$$

After rearranging them we get the propagation in time equations for the electromagnetic fields in one dimensional space

$$\begin{aligned}
\boldsymbol{H}_y\left(x,t+\frac{\Delta t}{2}\right) &= \boldsymbol{H}_y\left(x,t-\frac{\Delta t}{2}\right)+\frac{\Delta t}{\mu\Delta x}\left[\boldsymbol{E}_z\left(x+\frac{\Delta x}{2},t\right)-\boldsymbol{E}_z\left(x-\frac{\Delta x}{2},t\right)\right]\\
\boldsymbol{H}_z\left(x,t+\frac{\Delta t}{2}\right) &= \boldsymbol{H}_z\left(x,t-\frac{\Delta t}{2}\right)-\frac{\Delta t}{\mu\Delta x}\left[\boldsymbol{E}_y\left(x+\frac{\Delta x}{2},t\right)-\boldsymbol{E}_y\left(x-\frac{\Delta x}{2},t\right)\right]\\
\boldsymbol{E}_y\left(x,t+\frac{\Delta t}{2}\right) &= \boldsymbol{E}_y\left(x,t-\frac{\Delta t}{2}\right)-\frac{\Delta t}{\epsilon\Delta x}\left[\boldsymbol{H}_z\left(x+\frac{\Delta x}{2},t\right)-\boldsymbol{H}_z\left(x-\frac{\Delta x}{2},t\right)\right]\\
\boldsymbol{E}_z\left(x,t+\frac{\Delta t}{2}\right) &= \boldsymbol{E}_z\left(x,t-\frac{\Delta t}{2}\right)+\frac{\Delta t}{\epsilon\Delta x}\left[\boldsymbol{H}_y\left(x+\frac{\Delta x}{2},t\right)-\boldsymbol{H}_y\left(x-\frac{\Delta x}{2},t\right)\right].
\end{aligned} \qquad \text{Eq. B.7}$$

It can be seen from this set of equations that, for the differential nature of the Maxwell equations, $\boldsymbol{E}$ and $\boldsymbol{H}$ are staggered in time and space so that the simulation method is to compute one field, propagate the time by $\Delta t/2$, then, calculate the other field and propagate another $\Delta t/2$ to complete a full time step. The fields are also staggered in space such that each $\boldsymbol{E}$ field can be calculated from the spatial derivative of $\boldsymbol{H}$ and vice versa.

Two important issues arise from the quantization of space and time. One is that the continuous space derivation at point x does not exactly equal the quantitated derivation done in the computational method. In fact, this inaccuracy grows as the wavelength shortened. It is a general rule of thumb to use $\Delta x \sim \lambda/20$. The second issue relates to the time step; using a time step larger than $n\Delta x/c$, allows electromagnetic waves to travel faster than the simulation can keep up with. This, in turn, creates instabilities in the simulation domain and yields meaningless results. Therefore, the time step must be chosen as $\Delta t < n\Delta x/c$.

When extending the simulation to more dimensions, we look again at the Faraday's Law and Ampere's Law for nonconducting static media

$$\frac{d\boldsymbol{H}}{dt} = -\frac{1}{\mu}\nabla \times \boldsymbol{E}$$
$$\frac{d\boldsymbol{E}}{dt} = \frac{1}{\epsilon}\nabla \times \boldsymbol{H}. \qquad \text{Eq. B.8}$$

It is clear looking at these equations (at the curl operation to be specific) that the time step of $\boldsymbol{H}_i$ falls between two points of $\boldsymbol{E}_j$ in the $\hat{k}$ direction and vice versa where $\hat{\imath}$, $\hat{\jmath}$ and $\hat{k}$ are the three axis in any order. This staggered grid was found first by K. S. Yee and is called Yee grid (119). Fig. B.1 shows how the fields are being staggered in space in the Yee grid.

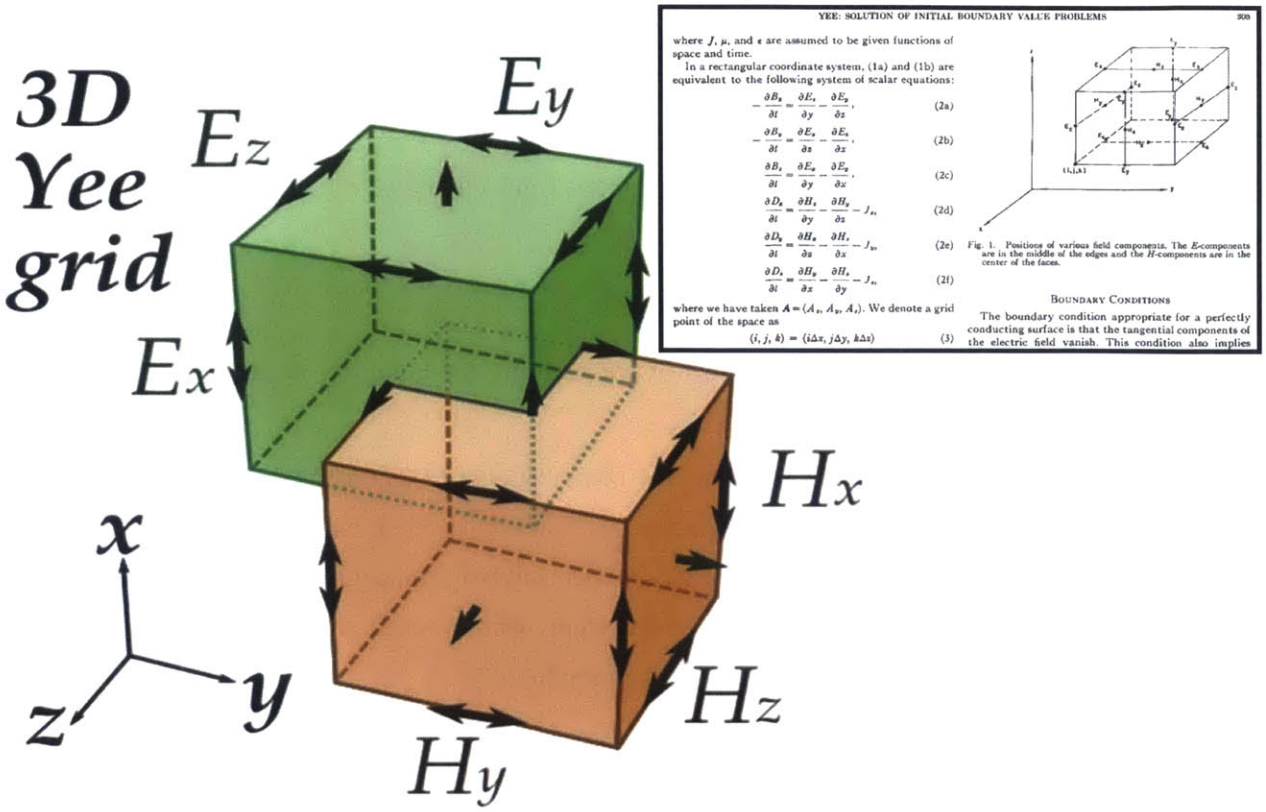

Fig. B.1 Yee grid: It is shown how the E field and the H field are staggered in space in a way that each field's time derivative is located between the two space derivative field locations that affect it. The inset shows a piece of the original paper (119) from 1966 where K. S. Yee breakes down Maxwell's equations to components, shows the field relation and draws the grid.

Looking at the boundary conditions for the simulation, the simplest thing to do is to set the last points of the grid in each facet to be the electric field points parallel to the surface and to set these points to $\boldsymbol{E} = 0$. This, while very easy to implement, mimics a boundary condition of a perfect conductor and reflects all waves straight back into the simulation domain. Different methods are also available to create a boundary with minimal reflections. One of the effective and most implemented methods consists of a set of Perfectly Matched Layers (PML). By adding a set of layers outside of the simulation domain with some conductivity to them, we are actually adding an absorptive section separating the perfect conduction boundary from the simulation domain. Nevertheless, a boundary between a pure dielectric and a dielectric with conductivity will always have some reflection of its own. In order to deal with that issue, we apply a (nonphysical) magnetic conductivity, so Maxwell's equations formulate as

$$\nabla \times \boldsymbol{H} = \epsilon \frac{d\boldsymbol{E}}{dt} + \sigma \boldsymbol{E}$$
$$\nabla \times \boldsymbol{E} = -\mu \frac{d\boldsymbol{H}}{dt} - \sigma^* \boldsymbol{H}\,. \qquad \text{Eq. B.9}$$

We then redefine ϵ and μ as

$$\bar{\epsilon} = \epsilon + \sigma/j\omega$$
$$\bar{\mu} = \mu + \sigma^*/j\omega\,. \qquad \text{Eq. B.10}$$

It is well known that the reflection of a wave with $\vec{k}$ perpendicular to the surface depends on the change in the wave impedance, $\eta = \sqrt{\mu/\epsilon}$, so by using the magnetic conductivity we can create a layer that has the same impedance as any dielectric layer simply by defining

$$\frac{\epsilon}{\mu} = \frac{\sigma}{\sigma^*}. \qquad \text{Eq. B.11}$$

There are also ways to adjust this method to a wave reaching the boundary at an angle but they are considered out of the scope for this appendix.

In this appendix we discussed the basics of the computational FDTD method. FDTD is a powerful tool that allows us to compute almost any structure with any kind of excitation with high accuracy to reality. Since it is sometimes computational costly and demand long simulations, it cannot yet be used as a standalone tool to design large components and systems, but, coupled with CMT which helps gain general understanding of the components it is a very strong tool.

Appendix C Phased Array Theory

Phased arrays are arrays of coherent sources, e.g. antennas, tuned to emit a specific phase patterned beam. The phase pattern is defined in the near field, but in the far field an amplitude pattern is produced by the destructive and constructive interference of the multiple antennas. The straight forward way of computing the far field pattern is by summing the antenna emissions in each direction, and find out how constructive/destructive is the emission in that direction.

In order to do this sum, we first look at the far field of a general source (single or multiple antennas). Starting from Equations 5.2.20 and 5.2.21 in (120) we find that the far field of a current source with current distribution $\boldsymbol{J}(r)$ is

$$\boldsymbol{E}^{\perp}(r) = -\frac{j\omega\mu_0 e^{-jkr}}{4\pi r}\int_v \boldsymbol{J}^{\perp}(r')e^{jk\hat{r}\cdot r'}dr' \qquad \text{Eq. C.1}$$

where r is the far field point and the antenna is defined in $r' \ll r$. The $\perp$ sign is to note that this equation is only for the perpendicular to $\hat{r}$ elements ($\hat{\varphi}$ and $\hat{\theta}$) of the vectors, while the $\hat{r}$ element of the electric field is negligible in the far field. $\boldsymbol{J}^{\perp}$ could also be written as $(\hat{r}\times\boldsymbol{J})\times\hat{r}$ to eliminate the need of defining $\boldsymbol{E}^{\perp}$. From here on we will omit the $\perp$ sign but still consider $\hat{r}\cdot\boldsymbol{E}\to 0$ in the far field. It is easy to see from Eq. C.1 that, for N identical antennas with phase ϕ_n and amplitude a_n placed at points r_n in space, we can substitute r' with $r_n + r''$ and rewrite (7.31) as a sum of integrals

$$\boldsymbol{E}(r) = \boldsymbol{E}_0(r)\sum_{n=1}^{N} a_n \exp\left(-j(k\hat{r}\cdot r_n + \phi_n)\right) \qquad \text{Eq. C.2}$$

$$\boldsymbol{E}_0(r) = -\frac{j\omega\mu_0 e^{-jkr}}{4\pi r}\int_{v_{single}} \boldsymbol{J_0}(r'')e^{jk\hat{r}\cdot r''}dr'' \qquad \text{Eq. C.3}$$

where the integration here is done over a single antenna rather than the entire array, and the n^{th} antenna's current density is $\boldsymbol{J}_n = a_n\boldsymbol{J}_0$. The subscript of $\boldsymbol{J}_0$ is to note that the current distribution can be normalized in some way (e.g. so that the sum on a_n equals 1). $\boldsymbol{E}_0$ was moved out of the sum since it is only a function of r and not a function of antenna number. Being so, $\boldsymbol{E}_0$ gives an envelope pattern to the array far field that is independent of the specific phase and amplitude arrangement between the individual antennas; the sum, then, defines the specific far field pattern within this envelope and is usually referred to as the array factor (AF).

Although for a Si based NPA the antennas are, in general, not represented by current sources, we can still consider the far field pattern of a single antenna $\boldsymbol{E}_0$ (which in far field still holds $\hat{r}\cdot\boldsymbol{E}_0\to 0$) and calculate the array emission pattern using Eq. C.2. In most cases, we can approximate the optical antenna near field pattern to that of a small aperture illuminated from behind with a flat phase electromagnetic

wave. Using Fourier optics it is clear that the $\boldsymbol{E}_0$ envelope's angular width is inversely proportional to the size of the aperture or, in other words, to the size of the individual antenna and the number of antennas.

In order to understand some fundamental concepts related to phased arrays we look at a simple example of a one dimensional optical phased array with antenna spacing D along the $\hat{x}$ axis and antenna (effective aperture) size d. For simplicity we also assume uniform power distribution between the N antennas of the array. The envelope, $\boldsymbol{E}_0$, far field of a single aperture, is known to be

$$\boldsymbol{E}_0(\theta) \propto \frac{\sin\left(\frac{\pi d}{\lambda} sin(\theta)\right)}{\frac{\pi d}{\lambda}\sin(\theta)} \qquad \text{Eq. C.4}$$

where θ is the angle from the $\hat{y}$ axis. The array factor sum, for array phases set to emit a narrow beam in direction θ_0 ($\phi_n = -nkD\sin(\theta_0)$), becomes from Eq. C.2

$$AF = \sum_{n=0}^{N-1} \exp jnkD(\sin(\theta_0) - \sin(\theta)) \propto \frac{\sin\left(\frac{\pi ND}{\lambda}(sin(\theta_0) - sin(\theta))\right)}{N\sin\left(\frac{\pi D}{\lambda}(sin(\theta_0) - sin(\theta))\right)}. \qquad \text{Eq. C.5}$$

Fig. C.1 plots the envelope $|E_0(\theta)|^2$ (blue line) and total power response $|E(\theta)|^2$ of this one dimensional phased array for $\theta_0 = -20°$ (green line) and $\theta_0 = 0°$ (black line). Emission to the latter called the broad side. It can be seen, from Eq. C.4 and Eq. C.5 and in the plot, that while the aperture size d defines the envelope of the emission pattern, the array pitch D is responsible for the side lobes position and the total array size ND defines the minimum beam width or far field resolution.

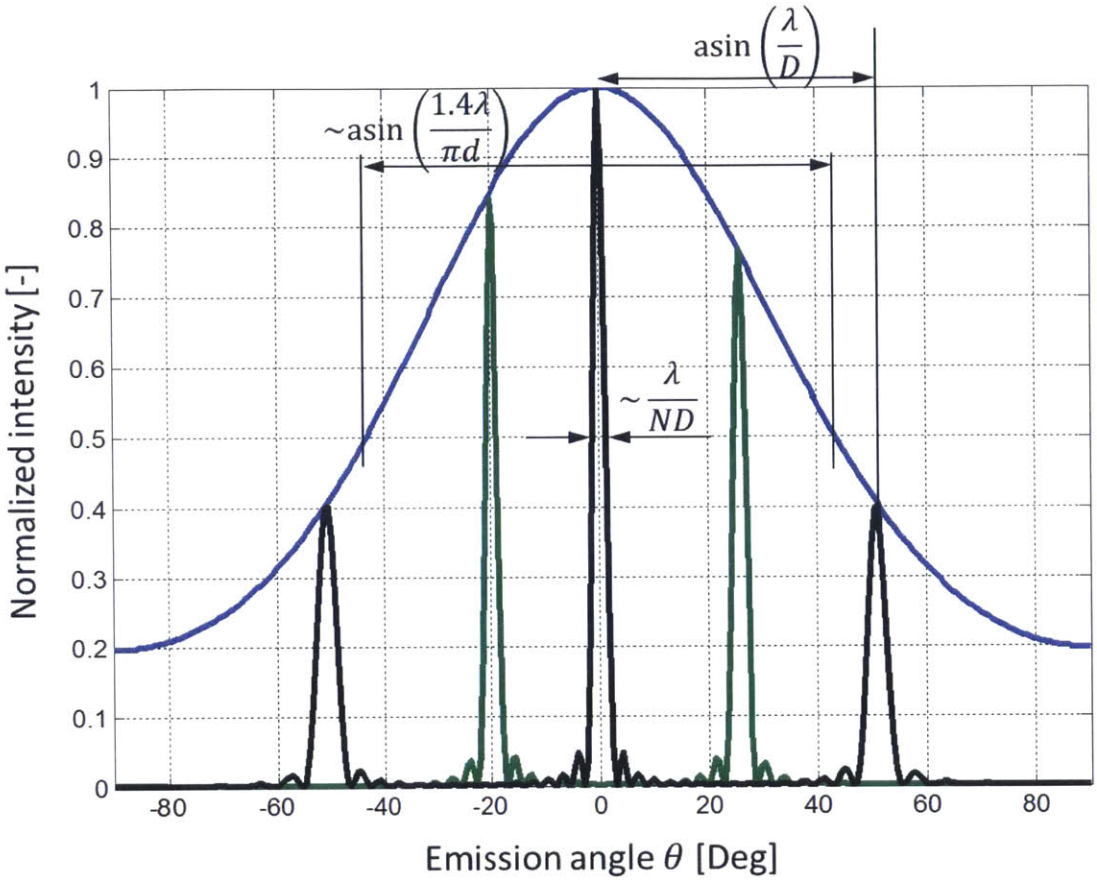

Fig. C.1 Far-field angular response of a one dimensional phased array: This is plotted for wavelength 1.55μm with 16 antennas sized 1μm and pitched 2μm. The blue line represents the envelope of the antenna, and the black and green lines show the beams when the array is pointing to the broad side direction and 20° to the left respectively. Beam resolution, side beams spacing and envelope width are specified on the plot.

For creating an angle region of 30° with no higher order interference even when sweeping the main beam to the edge of this region, we need 60° between the first and second order interferences which means the unit cell size should be smaller than 0.87 of a wavelength ($D/\lambda < 0.87$). If we want to clear the whole emission hemisphere of the array, we need this value to reach half.

Expanding the theory to the two dimensional case, we use two indices to describe the array factor of a rectangular grid array:

$$\boldsymbol{AF} = \sum_{n=0}^{N-1}\sum_{m=0}^{M-1} a_{mn}\exp\left(-j(k\hat{r}\cdot r_{mn} + \phi_{mn})\right) \qquad \text{Eq. C.6}$$

For beam steering we can utilze that the two axes are independent and write $\phi_{mn} = -\left(mkD_y\cos(\theta_{0,y}) + nkD_x\cos(\theta_{0,x})\right)$ and $\hat{r}\cdot r_{mn} = mD_y\cos(\theta_y) + nD_x\cos(\theta_x)$. It is important to note that the angles θ_x and θ_y are not spherical coordinates but the angles from the $\hat{x}$ and $\hat{y}$ axes respectively as can be seen in Fig. C.2. In spherical coordinates

$$\tan(\varphi) = \frac{\cos(\theta_x)}{\cos(\theta_y)}$$
$$\sin(\theta) = \frac{\cos(\theta_x)}{\sin(\varphi)} \; or \; \frac{\cos(\theta_y)}{\cos(\varphi)} \qquad \text{Eq. C.7}$$

where the two options of $\sin(\theta)$ cover for φ angles where the other is undefined.

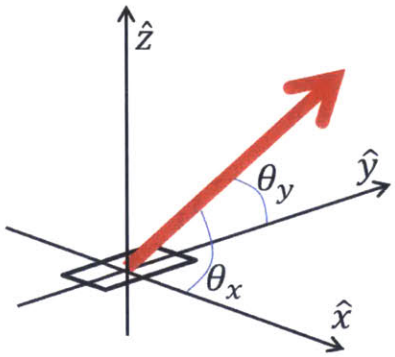

Fig. C.2 Angle definition: θ_x and θ_y for beam steering from a 2D array

Nevertheless, creating beams in far field is not the only ability of a phased array. The ability to integrate a large number of unit cells in a NPA within a small footprint opens up the possibility of using such arrays to generate arbitrary, sophisticated far-field radiation patterns. Using antenna synthesis through the Gerchberg–Saxton algorithm (121), (122), the phase ϕ_{mn} of each pixel can be determined in order to create complex far field patterns and 3D holograms. The algorithmic and design is out of the scope of this work but the fundamentals and basic designs shown here were created side by side with complex far field static images and set the path for the design of a holographic demonstration. The field of NPAs is a rapidly growing field of research and the arrays are expected to make major impact on our world in the near future.

Bibliography

1. **1. Lightman, Alan.** *The discoveries: great breakthroughs in 20th-century science.* Vintage Canada : s.n., 2010.

2. 2. "Cisco Visual Networking Index: Forecast and Methodology, 2013–2018" white paper. [Online] http://www.cisco.com/c/en/us/solutions/collateral/service-provider/ip-ngn-ip-next-generation-network/white_paper_c11-481360.pdf.

3. **Wanlass, Frank M.** *Low stand-by power complementary field effect circuitry. U.S. Patent 3,356,858* December 5, 1967.

4. TI introduces first commercial silicon transistor. [Online] Texas Instrument. http://www.ti.com/corp/docs/company/history/timeline/semicon/1950/docs/54commercial.htm.

5. *Fiber in the Home: Broadband Networks and Optic Distributed Sensing.* **Liu, Baozhong, et al., et al.** 18 Dec 2008. Future BioMedical Information Engineering 2008, FBIE '08. pp. 223-228.

6. *Large-scale nanophotonic phased array.* **6. Sun, Jie, Timurdogan, Erman, Yaacobi, Ami, Hosseini, Ehsan Shah and Watts, Michael R.** 7431, s.l. : Nature, Jan 10, 2013, Vol. 493 , pp. 195-199.

7. *The Past, Present, and Future of Silicon Photonics.* **R., Soref.** 6, s.l. : Selected Topics in Quantum Electronics, IEEE Journal of, Nov-Dec 2006, Vol. 12, pp. 1678-1687.

8. *Silicon photonics: a bright future?* **Paul, D.J.** 12, 2009, Electronics Letters, Vol. 45, pp. 582-584.

9. *Adiabatic Resonant Microrings (ARMs) with Directly Integrated Thermal Microphotonics.* **M. R. Watts, W. A. Zortman, D. C. Trotter, G. N. Nielson, D. L. Luck, and R. W. Young,.** s.l. : OSA Technical Digest (CD) (Optical Society of America, 2009). in Conference on Lasers and Electro-Optics/International Quantum Electronics Conference. CPDB10.

10. *High-speed low-voltage single-drive push-pull silicon Mach-Zehnder modulators.* **Po Dong, Long Chen, and Young-kai Chen,.** 2012, Optics Express, Vol. 20, pp. 6163-6169.

11. *Silicon-on-insulator spectral filters fabricated with CMOS technology.* **Bogaerts, Wim, Shankar Kumar Selvaraja, Pieter Dumon, Joost Brouckaert, Katrien De Vos, Dries Van Thourhout, and Roel Baets.** 1, s.l. : IEEE, 2010, IEEE journal of selected topics in quantum electronics, Vol. 16, pp. 33-44.

12. *High-performance Ge-on-Si photodetectors.* **Michel, Jurgen, Jifeng Liu, and Lionel C. Kimerling.** 8, 2010, Nature Photonics, Vol. 4, pp. 527-534.

13. *Ultra compact 45 GHz CMOS compatible Germanium waveguide photodiode with low dark current.* **Christopher T. DeRose, Douglas C. Trotter, William A. Zortman, Andrew L. Starbuck, Moz Fisher, Michael R. Watts, and Paul S. Davids.** Optics Express, Vol. 19, pp. 24897-24904.

14. Northrop Grumman Integrates All Phased Array Antennas on First Advanced EHF Flight Payload. *Globe Newswire.* Jan 23, 2007.

15. **Winkler, David F and Webster, Julie L.** *Searching the Skies: The Legacy of the United States Cold War Defense Radar Program.* s.l. : Champaign, IL: U.S. Army Construction Engineering Research Laboratories, 1997. LCCN 97020912.

16. **Keller, John.** Air Force eyes passive radar surveillance with initiative on wideband phased array antennas. *Military Aerospace.* 2012.

17. **Friedman, Norman.** The Naval Institute guide to world naval weapon systems. *Naval Institute Press.* 2006.

18. *Anisotropic leaky-mode modulator for holographic video displays.* **Smalley, D. E., Q. Y. J. Smithwick, V. M. Bove, J. Barabas, and S. Jolly.** 7454, 2013, Nature, Vol. 498, pp. 313-317.

19. *Indoor scene segmentation using a structured light sensor.* **Silberman, Nathan, and Rob Fergus.** s.l. : IEEE International Conference on, 2011. In Computer Vision Workshops (ICCV Workshops). pp. 601-608.

20. *Chip-Scale Continuously Tunable Optical Orbital Angular Momentum Generator.* **Sun, Jie, Ami Yaacobi, Michele Moresco, Douglas Coolbaugh, and Michael R. Watts.** 2014, arXiv preprint. 1408.3315.

21. *Optical phased array using high contrast gratings for two dimensional beamforming and beamsteering.* **Yoo, Byung-Wook, Mischa Megens, Trevor Chan, Tianbo Sun, Weijian Yang, Connie J. Chang-Hasnain, David A. Horsley, and Ming C. Wu.** 10, 2013, Optics express, Vol. 21, pp. 12238-12248.

22. *Implementation of controlling the divergence angle utilizing liquid crystal optical phased array.* **Xiao, Feng, and Lingjiang Kong.** s.l. : International Society for Optics and Photonics, 2012. In Photonics Asia. pp. 85570I-85570I.

23. *Two-dimensional free-space beam steering with an optical phased array on silicon-on-insulator.* **Doylend, Jonathan K., M. J. R. Heck, Jock T. Bovington, Jonathan D. Peters, L. A. Coldren, and J. E. Bowers.** 22, 2011, Optics express, Vol. 19, pp. 21595-21604.

24. *Two-dimensional optical phased array antenna on silicon-on-insulator.* **Van Acoleyen, Karel, Hendrik Rogier, and Roel Baets.** 13, 2010, Optics express, Vol. 18, pp. 13655-13660.

25. *Large-Scale Silicon Photonic Circuits for Optical Phased Arrays.* **Sun, Jie, Erman Timurdogan, Ami Yaacobi, Zhan Su, Ehsan Shah Hosseini, David B. Cole, and Michael R. Watts.** 4, s.l. : IEEE Jurnal of, 2014, Selected Topics in Quantum Electronics, Vol. 20, pp. 264-278.

26. *Novel 1-to-N way integrated optical beam splitters using symmetric mode mixing in GaAs/AlGaAs multimode waveguides.* **Heaton, J. M., R. M. Jenkins, D. R. Wight, J. T. Parker, J. C. H. Birbeck, and K. P. Hilton.** 15, 1992, Applied Physics Letters, Vol. 61, pp. 1754-1756.

27. *Integrated optic adiabatic devices on silicon.* **Shani, Yosi, Charles H. Henry, Rodney C. Kistler, Rudolph F. Kazarinov, and Kenneth J. Orlowsky.** 3, s.l. : IEEE Journal of, 1991, Quantum Electronics, Vol. 27, pp. 556-566.

28. *Off-chip beam steering with a one-dimensional optical phased array on silicon-on-insulator.* **Van Acoleyen, Karel, Wim Bogaerts, Jana Jágerská, Nicolas Le Thomas, Romuald Houdré, and Roel Baets.** 9, 2009, Optics letters, Vol. 34, pp. 1477-1479.

29. **Haus, Hermann A.** *Waves and fields in optoelectronics.* Englewood Cliffs, NJ : Prentice-Hall, 1984. Vol. 464.

30. *Compact bandwidth-tunable microring resonators.* **L.Chen, N. Sherwood-Droz, and M. Lipson.** 22, Nov 2007, Optics letters, Vol. 32, pp. 3361–3363.

31. *Maximizing the thermo-optic tuning range of silicon photonic structures.* **F. Gan, T. Barwicz, M. Popovi´c, M. Dahlem, C. Holzwarth, P. T. Rakich, H. Smith, E. Ippen, and F. K.** 2007. IEEE Photonics in Switching Conference. pp. 67-68.

32. *Wavelength-tunable silicon microring modulator.* **P. Dong, R. Shafiiha, S. Liao, H. Liang, N.-N. Feng, D. Feng, G. Li, X. Zheng, A. V. Krishnamoorthy, and M. Asghari.** 11, May 2010, Optics Express, Vol. 18, pp. 10 941–10 946.

33. *Silicon microring modulator with integrated heater and temperature sensor for thermal control.* **C. T. DeRose, M. R. Watts, D. C. Trotter, D. L. Luck, G. N. Nielson, and R. W. Young.** 2010. Lasers and Electro-Optics Confrence. pp. 1-2. CThJ3.

34. *Adiabatic resonant microrings (ARMs) with directly integrated thermal microphotonics.* **M. Watts, W. Zortman, D. Trotter, G. Nielson, D. Luck, and R. Young.** 2009. Lasers and Electro-Optics Conf. pp. 1-2. CPDB10.

35. *Low power and broadband 2 × 2 silicon thermo-optic switch.* **C. T. DeRose, M. Watts, R. W. Young, D. C. Trotter, G. N. Nielson, W. Zortman, and R. D. Kekatpure.** Losangeles : s.n., 2011. Optical Fiber Communication Conf. OThM3.

36. *Adiabatic thermo-opticMach-Zehnder switch.* **M. R. Watts, J. Sun, C. DeRose, D. C. Trotter, R. W. Young, and G. N.Nielson.** 5, Mar 2013, Optics Letters, Vol. 38, pp. 733-735.

37. *Thermally tunable SOICMOS photonics circuits.* **I. Shubin, X. Zheng, H. Thacker, J. Yao, J. Costa, Y. Luo, G. Li, A. V. Krishnamoorthy, J. E. Cunningham, T. Pinguet, and A. Mekis.** 2010. Proceedings of SPIE. Vol. 7607, pp. 76 070C-1–76 070C-6.

38. *Adiabatic microring resonators.* **Watts, M. R.** 19, Oct 2010, Optics Letters, Vol. 35, pp. 3231–3233.

39. *Adiabatic resonant microring (ARM) modulator.* **E. Timurdogan, M.Moresco,A. Biberman, J. Sun,W. Zortman,D. Trotter, andM.Watts.** s.l. : IEEE, 2012. Optical Interconnects Confrence. pp. 48-49.

40. *Electrooptical effects in silicon.* **Bennett, R. A. Soref and B.** 1, s.l. : IEEE, Jan 1987, jurnal of Quantum Electronics, Vol. 23, pp. 123-129.

41. *Core-shell nanowire optical antennas fed by slab waveguides.* **Li, Jingjing, and Nader Engheta.** 11, s.l. : IEEE Transactions, 2007, Antennas and Propagation, Vol. 55, pp. 3018-3026.

42. *Waveguide-fed optical hybrid plasmonic patch nano-antenna.* **Yousefi, Leila, and Amy C. Foster.** 16, 2012, Optics Express, Vol. 20, pp. 18326-18335.

43. **Davids, Paul S., Christopher T. DeRose, Rohan Deodatta Kekatpure, Joel Robert Wendt, Andrew Lea Starbuck, Douglas Chandler Trotter, Jeffrey W. Lantz, Uday Chettiar, Nader Engheta, Yaacobi, Ami and Michael R. Watts.** *Plasmonic Nanoantenna for On-chip Optical Phased Arrays.* Albuquerque, NM : Sandia National Laboratories (SNL-NM), 2012. SAND2012-0829C.

44. *Hybrid nanoplasmonic-photonic resonators for efficient coupling of light to single plasmonic nanoresonators.* **Chamanzar, Maysamreza, and Ali Adibi.** 22, 2011, Optics Express, Vol. 19, pp. 22292-22304.

45. *An out-of-plane grating coupler for efficient butt-coupling between compact planar waveguides and single-mode fibers.* **Taillaert, Dirk, Wim Bogaerts, Peter Bienstman, Thomas F. Krauss, Peter Van Daele, Ingrid Moerman, Steven Verstuyft, Kurt De Mesel, and Roel Baets.** 7, s.l. : IEEE Journal, 2002, Quantum Electronics, Vol. 38, pp. 949-955.

46. *Silicon-on-insulator chip-to-chip coupling via out-of-plane or vertical grating couplers.* **Cabezón, Miguel, Ignacio Garcés, Asier Villafranca, José Pozo, Pragati Kumar, and Andrzej Kaźmierczak.** 34, 2012, Applied Optics, Vol. 51, pp. 8090-8094.

47. *A grating-coupler-enabled CMOS photonics platform.* **Mekis, Attila, Steffen Gloeckner, Gianlorenzo Masini, Adithyaram Narasimha, Thierry Pinguet, Subal Sahni, and Peter De Dobbelaere.** 3, s.l. : IEEE Journal of, 2011, Selected Topics in Quantum Electronics, Vol. 17, pp. 597-608.

48. *Optical Antennas.* **Palash Bharadwaj, Bradley Deutsch, and Lukas Novotny.** 2009, Advanced Optics and Photonics, Vol. 1, pp. 438-483.

49. *Optical antennas: Resonators for local field enhancement.* **K. B. Crozier, A. Sundaramurthy, G. S. Kino, and C. F. Quate.** 2003, Jurnal of Applied Physics, Vol. 94, p. 4632.

50. *Input Impedance, Nanocircuit Loading, and Radiation Tuning of Optical Nanoantennas.* **Engheta, Andrea Alù and Nader.** 2008, Physics Review Letters, Vol. 101, p. 043901.

51. *Gap-Dependent Optical Coupling of Single "Bowtie" Nanoantennas Resonant in the Visible.* **David P. Fromm, Arvind Sundaramurthy, P. James Schuck, Gordon Kino, and, and W. E. Moerner.** 5, 2004, Nano Letters, Vol. 4, pp. 957-961.

52. *3D optical Yagi-Uda nanoantenna array.* **Daniel Dregely, Richard Taubert, Jens Dorfmuller, Ralf Vogelgesang, Klaus Kern and Harald Giessen.** 5 4, 2011, Nature Communication, Vol. 2, p. 267.

53. *Directional control of light by a nano-optical Yagi-Uda antenna.* **Terukazu Kosako, Yutaka Kadoya, Holger F. Hofmann.** 5, 5 2010, Nature Photonics, Vol. 4, pp. 312-315.

54. *Vertical emitting aperture nanoantennas.* **Yaacobi, Ami, Erman Timurdogan, and Michael R. Watts.** 9, 2012, Optics Letters, Vol. 37, pp. 1454-1456.

55. *Compact Nano-Antenna Emitters for Optical Phased Array Applications.* **Shtyrkova, Katia, Ami Yaacobi, Paul Davids, Doug C. Trotter, Joel Wendt, Chris DeRose, Rohan Kekatpure, Erich P. Ippen, and Michael R. Watts.** 2011. CLEO.

56. *High Directivity, Vertical Fiber-to-Chip Coupler with Anisotropically Radiating Grating Teeth.* **M. Fan, M. Popovic, and F. X. Kaertner.** s.l. : OSA Technical Digest Series (CD) (Optical Society of America, 2007). Lasers and Electro-Optics/Quantum Electronics and Laser Science Conference and Photonic Applications Systems Technologies. CTuDD3.

57. *Embedded slanted grating for vertical coupling between fibers and silicon-on-insulator planar waveguides.* **Wang, Bin, Jiang, Jianhua and Nordin, G.P.** 9, Sep 2005, Photonics Technology Letters, Vol. 17, pp. 1884-1886.

58. *Cavity-resonator-integrated grating input/output coupler for high-efficiency vertical coupling with a small aperture.* **Kenji Kintaka, Yuki Kita, Katsuya Shimizu, Hitoshi Matsuoka, Shogo Ura, and Junji Nishii.** 2010, Optics Letters, Vol. 35, pp. 1989-1991.

59. *High efficiency grating coupler between silicon-on-insulator waveguides and perfectly vertical optical fibers.* **Günther Roelkens, Dries Van Thourhout, and Roel Baets.** 2007, Optics Letters, Vol. 32, pp. 1495-1497.

60. *Metal Grating Patterning on Fiber Facets by UV-Based Nano Imprint and Transfer Lithography Using Optical Alignment.* **Stijn Scheerlinck, Peter Dubruel, Peter Bienstman, Etienne Schacht, Dries Van Thourhout, and Roel Baets.** 2009, Jurnal of Lightwave Technology, Vol. 27, pp. 1415-1420.

61. *Microring resonator channel dropping filters.* **Little, B. E., et al., et al.** 6, Jan 1997, Lightwave Technology, Vol. 15, pp. 998-1005.

62. *Coupled-mode theory.* **Haus, H. A. and Huang, W.** 10, s.l. : IEEE, Oct 1991, Proceedings of the IEEE, Vol. 79, pp. 1505-1518.

63. **Philipp, H. R.** SiO2 (Glass) and Si3N4. [book auth.] Edward D. Palik. *Handbook of Optical Constants of Solids.* Elsevier : s.n., 1998, pp. 760, 774.

64. *Frequency-chirped subwavelength nanoantennas.* **Yaacobi, Ami, and Michael R. Watts.** 23, 2012, Optics Letters, Vol. 37, pp. 4979-4981.

65. *Electronically controlled optical beam-steering by an active phased array of metallic nanoantennas.* **DeRose, C. T., R. D. Kekatpure, D. C. Trotter, A. Starbuck, J. R. Wendt, A. Yaacobi, M. R. Watts, U. Chettiar, N. Engheta, and P. S. Davids.** 4, 2013, Optics Express, Vol. 21, pp. 5198-5208.

66. *Grating-Based Optical Fiber Interfaces for Silicon-on-Insulator Photonic Integrated Circuits.* **Roelkens, G., et al., et al.** 3, s.l. : IEEE Journal of, May-Jun 2011, Selected Topics in Quantum Electronics, Vol. 17, pp. 571-580.

67. *Optical phased array technology.* **McManamon, P.F., et al., et al.** 2, Feb 1996, Proceedings of the IEEE, Vol. 84, pp. 268-298.

68. *Optical beam steering using a multichannel lithium tantalate crystal.* **Meyer, R. A.** 3, 1972, Applied optics, Vol. 11, pp. 613-616.

69. *High-efficiency liquid-crystal optical phased-array beam steering.* **Resler, D. P., D. S. Hobbs, R. C. Sharp, L. J. Friedman, and T. A. Dorschner.** 9, 1996, Optics Letters, Vol. 21, pp. 689-691.

70. *The first demonstration of an optically steered microwave phased array antenna using true-time-delay.* **Ng, W. I. L. L. I. E. W., Andrew A. Walston, Gregory L. Tangonan, Jar Juch Lee, Irwin L. Newberg, and Norman Bernstein.** 9, 1991, Lightwave Technology, Vol. 9, pp. 1124-1131.

71. *1×12 Unequally spaced waveguide array for actively tuned optical phased array on a silicon nanomembrane.* **Kwong, David, Amir Hosseini, Yang Zhang, and Ray T. Chen.** 5, 2011, Applied Physics Letters, Vol. 99.

72. *Electronic beam steering in monolithic grating-surface-emitting diode laser arrays.* **N. W. Carlson1, G. A. Evans1, R. Amantea1, S. L. Palfrey1, J. M. Hammer, M. Lurie, L. A. Carr, F. Z.**

Hawrylo, E. A. James, C. J. Kaiser, J. B. Kirk and W. F. Reichert. 23, 1988, Applied physics letters, Vol. 53, pp. 2275-2277.

73. *Light propagation with phase discontinuities: generalized laws of reflection and refraction.* **Yu, Nanfang, Patrice Genevet, Mikhail A. Kats, Francesco Aieta, Jean-Philippe Tetienne, Federico Capasso, and Zeno Gaburro.** 6054, 2011, Science, Vol. 334, pp. 333-337.

74. *Suppression of sidelobes in the far-field radiation patterns of optical waveguide arrays.* **Abeles, J. H., and R. J. Deri.** 15, 1988, Applied Physics Letters, Vol. 53, pp. 1375-1377.

75. *Resonant optical antennas.* **Mühlschlegel, P., H-J. Eisler, O. J. F. Martin, B. Hecht, and D. W. Pohl.** 5728, 2005, Science, Vol. 308, pp. 1607-1609.

76. *Improving the mismatch between light and nanoscale objects with gold bowtie nanoantennas.* **Schuck, P. J., D. P. Fromm, A. Sundaramurthy, G. S. Kino, and W. E. Moerner.** 1, 2005, Physical review letters, Vol. 94.

77. *Tuning the scattering response of optical nanoantennas with nanocircuit loads.* **Alu, Andrea, and Nader Engheta.** 5, 2008, Nature Photonics, Vol. 2, pp. 307-310.

78. *Nanometre-scale germanium photodetector enhanced by a near-infrared dipole antenna.* **Tang, Liang, Sukru Ekin Kocabas, Salman Latif, Ali K. Okyay, Dany-Sebastien Ly-Gagnon, Krishna C. Saraswat, and David AB Miller.** 4, 2008, Nature Photonics, Vol. 2, pp. 226-229.

79. *High efficiency Silicon-on-Insulator grating coupler based on a poly-Silicon overlay.* **Roelkens, GŘnther, Dries Van Thourhout, and Roel Baets.** 24, 2006, Optics Express, Vol. 14, pp. 11622-11630.

80. **Taflove, A. & Hagness, S. C.** *Computational Electrodynamics: The Finite-Difference Time-Domain Method.* 3rd. s.l. : Artech House, 2005.

81. *Exploring light propagating in photonic crystals with Fourier optics.* **Le Thomas, Nicolas, Romuald Houdré, Maria V. Kotlyar, David O'Brien, and Thomas F. Krauss.** 12, 2007, JOSA B, Vol. 24, pp. 2964-2971.

82. **Krabill, W. B., J. G. Collins, L. E. Link, R. N. Swift, and M. L. Butler.** *Airborne laser topographic mapping results.* s.l. : NASA, 1984.

83. *Lidar Remote Sensing for Ecosystem Studies Lidar, an emerging remote sensing technology that directly measures the three-dimensional distribution of plant canopies, can accurately estimate vegetation structural attributes and should be of particular inter.* **Lefsky, Michael A., Warren B. Cohen, Geoffrey G. Parker, and David J. Harding.** 1, 2002, BioScience, Vol. 52, pp. 19-30.

84. *A new method for building extraction in urban areas from high-resolution LIDAR data.* **Rottensteiner, Franz, and Christian Briese.** 3/A, 2002, International Archives of Photogrammetry Remote Sensing and Spatial Information Sciences, Vol. 34, pp. 295-301.

85. **Fountain, Henry.** Yes, Driverless Cars Know the Way to San Jose. *New York Times.* 2012, Vol. 26.

86. *Inside Google's Quest To Popularize Self-Driving Cars.* **Fisher, Adam.** 2013, Popular Science (Online Articale).

87. *C-and L-band erbium-doped waveguide lasers with wafer-scale silicon nitride cavities.* **Purnawirman, Sun, J., Thomas N. Adam, Gerald Leake, Douglas Coolbaugh, Jonathon DB Bradley, E. Shah Hosseini, and Michael R. Watts.** 11, 2013, Optics Letters, Vol. 38, pp. 1760-1762.

88. *CMOS-compatible 75 mW erbium-doped distributed feedback laser.* **Hosseini, Ehsan Shah, Purnawirman, Jonathan DB Bradley, Jie Sun, Gerald Leake, Thomas N. Adam, Douglas D. Coolbaugh, and Michael R. Watts.** 11, 2014, Optics Letters, Vol. 39, pp. 3106-3109.

89. *An Ultra Low Power 3D Integrated Intra-Chip Silicon Electronic-Photonic Link.* **E. Timurdogan, Z. Su, K. Settaluri, S. Lin, S. Moazeni, C. Sun, G. Leake, D. Coolbaugh, B. Moss, M. Moresco, V. Stojanovitch, and M. Watts.** s.l. : OSA Technical Digest (online), 2015. Optical Fiber Communication Conference. Th5B.8.

90. *Laser ranging at 1550 nm with 1-GHz sine-wave gated InGaAs/InP APD single-photon detector.* **Ren, Min, Xiaorong Gu, Yan Liang, Weibin Kong, E. Wu, Guang Wu, and Heping Zeng.** 14, 2011, Optics Express, Vol. 19, pp. 13497-13502.

91. *Laser ranging: a critical review of usual techniques for distance measurement.* **Amann, Markus-Christian, Thierry Bosch, Marc Lescure, Risto Myllyla, and Marc Rioux.** 1, 2001, Optical engineering, Vol. 40, pp. 10-19.

92. **Barton, David Knox.** *Radar system analysis.* s.l. : Artech, 1976.

93. **Horowitz, Paul, Winfield Hill, and Thomas C. Hayes.** *The art of electronics.* Cambridge : Cambridge university press, 1989. Vol. 2.

94. *Integrated heterodyne interferometer with on-chip modulators and detectors.* **David B. Cole, Cheryl Sorace-Agaskar, Michele Moresco, Gerald Leake, Douglas Coolbaugh, and Michael R. Watts.** 2015.

95. **Sorace-Agaskar, Cheryl.** *Analog Integrated Photonics.* EECS, Massachutssets Institute of Technology. s.l. : Massachutssets Institute of Technology, 2015.

96. *Fully integrated hybrid silicon free-space beam steering source with 32 channel phased array.* **Hulme, J. C., J. K. Doylend, M. J. R. Heck, J. D. Peters, M. L. Davenport, J. T. Bovington, L. A. Coldren, and J. E. Bowers.** 2014. SPIE.

97. *Optical phased array using single crystalline silicon high-contrast-gratings for beamsteering.* **Yoo, Byung-Wook, Trevor Chan, Mischa Megens, Tianbo Sun, Weijian Yang, Yi Rao, David A.**

Horsley, Connie J. Chang-Hasnain, and Ming C. Wu. s.l. : International Society for Optics and Photonics, 2013. SPIE OPTO. pp. 86330F-86330F.

98. *Road environment recognition using on-vehicle lidar.* **K. Takagi, K. Morikawa, T. Ogawa and M. Saburi.** 2006. IEEE Intelligent Vehicles Symposium. pp. 120-125.

99. *Towards fully autonomous driving: Systems and algorithms.* **J. Levinson, J. Askeland, J. Becker, J. Dolson, D. Held, S. Kammel, J. Z. Kolter, D. Langer, O. Pink, V. Pratt, M. Sokolsky, G. Stanek, D. Stavens, A. Teichman, M. Werling and S. Thrun.** 2011. Fourth IEEE Intelligent Vehicles Symposium. pp. 163-168.

100. *Autonomous Ground Vehicles—Concepts and a Path to the Future.* **T. Luettel, M. Himmelsbach and H. J. Wuensche.** 13, 2012, Proceedings of the IEEE, Vol. 100, pp. 1831-1839.

101. *On-chip silicon optical phased array for two-dimensional beam steering.* **David Kwong, Amir Hosseini, John Covey, Yang Zhang, Xiaochuan Xu, Harish Subbaraman, and Ray T. Chen.** 4, 2014, Optics Letters, Vol. 39, pp. 941-944.

102. *Two-dimensional optical beam steering with InP-based photonic integrated circuits.* **Guo, Weihua, P. Binetti, Chad Althouse, M. Masanovic, H. Ambrosius, L. Johansson, and L. Coldren.** 4, 2013, JOURNAL OF SELECTED TOPICS IN QUANTUM ELECTRONICS, Vol. 19.

103. *Efficient coupling into polymer waveguides by gratings.* **Waldhäusl, Ralf, Bernd Schnabel, Peter Dannberg, Ernst-Bernhard Kley, Andréas Bräuer, and Wolfgang Karthe.** 36, 1997, Applied optics, Vol. 36, pp. 9383-9390.

104. *Refractive index of silicon and germanium and its wavelength and temperature derivatives.* **Li, H. H.** 3, 1980, Journal of physical and chemical reference data, Vol. 9, pp. 561-658.

105. Velodyne webpage showing their HDL-64E product. [Online] http://velodynelidar.com/lidar/hdlproducts/hdl64e.aspx.

106. **Jie, Sun.** *Toward accurate and large-scale silicon photonics.* s.l. : Massachutssets Institute of Technology, 2013.

107. **Polyanskiy, Mikhail.** *RefractiveIndex.INFO Refractive index database.* [Online] http://refractiveindex.info/.

108. *Integer and fractional angular momentum borne on self-trapped necklace-ring beams.* **Soljačić, Marin, and Mordechai Segev.** 3, 2001, Physical review letters, Vol. 86.

109. *Terabit free-space data transmission employing orbital angular momentum multiplexing.* **Jian Wang, Jeng-Yuan Yang, Irfan M. Fazal, Nisar Ahmed, Yan Yan, Hao Huang, Yongxiong Ren, Yang Yue, Samuel Dolinar, Moshe Tur & Alan E. Willner.** 7, 2012, Nature Photonics, Vol. 6, pp. 488-496.

110. *Terabit-scale orbital angular momentum mode division multiplexing in fibers.* **Bozinovic, Nenad, Yang Yue, Yongxiong Ren, Moshe Tur, Poul Kristensen, Hao Huang, Alan E. Willner, and Siddharth Ramachandran.** 6140, 2013, Science, Vol. 340, pp. 1545-1548.

111. *Quantum correlations in optical angle–orbital angular momentum variables.* **Leach, Jonathan, Barry Jack, Jacqui Romero, Anand K. Jha, Alison M. Yao, Sonja Franke-Arnold, David G. Ireland, Robert W. Boyd, Stephen M. Barnett, and Miles J. Padgett.** 5992, 2010, Science, Vol. 329, pp. 662-665.

112. *Controlled rotation of optically trapped microscopic particles.* **Paterson, L., M. P. MacDonald, J. Arlt, Wilson Sibbett, P. E. Bryant, and Kishan Dholakia.** 5518, 2001, Science, Vol. 292, pp. 912-914.

113. *Pure angular momentum generator using a ring resonator.* **Yu, Y. F., Y. H. Fu, X. M. Zhang, A. Q. Liu, T. Bourouina, T. Mei, Z. X. Shen, and Din Ping Tsai.** 21, 2010, Optics express, Vol. 18, pp. 21651-21662.

114. *Coupled-mode theory for guided-wave optics.* **Yariv, Amnon.** 9, s.l. : IEEE Journal of, 1973, Quantum Electronics, Vol. 9, pp. 919-933.

115. *Coupled mode theory of parallel waveguides.* **Hardy, Amos, and William Streifer.** 5, 1985, Lightwave Technology, Vol. 3, pp. 1135-1146.

116. *FDTD for N th-order dispersive media.* **Luebbers, Raymond J., and Forrest Hunsberger.** 11, s.l. : IEEE Transactions on, 1992, Antennas and Propagation, Vol. 40, pp. 1297-1301.

117. *An FDTD formulation for dispersive media using a current density.* **Chen, Qing, Makoto Katsurai, and Paul H. Aoyagi.** 11, s.l. : IEEE Transactions on, 1998, Antennas and Propagation, Vol. 46, pp. 1739-1746.

118. *Analysis and compensation of numerical dispersion in the FDTD method for layered, anisotropic media.* **Moss, C. D., Fernando L. Teixeira, and Jin Au Kong.** 9, s.l. : IEEE Transactions on, 2002, Antennas and Propagation, Vol. 50, pp. 1174-1184.

119. *Numerical solution of initial boundary value problems involving Maxwell's equations in isotropic media.* **Yee, Kane S.** 3, s.l. : IEEE Transactions, 1966, Antennas and Propagation, Vol. 14, pp. 302-307.

120. **Kong, J. A.** *Electromagnetic Wave Theory.* s.l. : EMW Publishing, 2008.

121. *practical algorithm for the determination of phase from image and diffraction plane pictures.* **Publishing, EMW.** 2, 1972, Vol. 35, pp. 273-246.

122. *Reconstruction of an object from the modulus of its Fourier transform.* **Fienup, J. R.** 1978, Optics Letters, Vol. 3, pp. 27-29.